Universidad Popular Autónoma del Estado de Puebla

Vicerrectoría de Investigación y Posgrados

Decanato de Ingenierías y Negocios

Graduate Biomedical Engineering and
Biomedical Engineering Sciences

Haptic model design for preoperative planning in maxillofacial, pediatric, and reconstructive surgery using FDM technology

by

MSc. Diana Ibarra Medel

A Thesis Presented in Partial Fulfillment
of the Requirements for the Degree

Doctor of Biomedical Engineering

is approved by the thesis committee:

Dr. Juan Manuel López Oglesby
Advisor

Dr. Evelyn Solís León
Committee Member

Dr. Luis Rosales Roldán
Committee Member

Puebla, Mexico

May 4, 2019

Universidad Popular Autónoma del Estado de Puebla

Vicerrectoría de Investigación y Posgrados

Decanato de Ingenierías y Negocios

Doctorado en Ingeniería Biomédica

Se aprueba la tesis:

Haptic model design for preoperative planning in maxillofacial, pediatric, and reconstructive surgery using FDM technology

Presentada por

M.C. Diana Ibarra Medel

Comité Asesor:

Dr. Juan Manuel López Oglesby
Director de Tesis

Dra. Evelyn Solís León
Asesor de Tesis

Dr. Luis Rosales Roldán
Asesor de Tesis

Puebla, México

4 de mayo 2019

Acknowledgements

Bueno, creo que es el final de un largo viaje, me tomó cerca de 10 años encontrar una motivación como estudiante, pasé desde la moda de la ingeniería genética hasta la manufactura aditiva, lo cual sin duda agradezco a cada persona que haya estado involucrada en este viaje, mencionarlas a cada una de ellas me llevaría escribir otra tesis, por lo tanto, si de casualidad se topan con esta pequeña sección de mi tesis… GRACIAS.

El mayor agradecimiento sin duda alguna se los doy a mis padres, ellos me formaron desde pequeña, me vieron nacer y ahora me ven defendiendo todo el trabajo realizado durante 4 años de doctorado. Ellos me motivaron a seguir un camino diferente, no sólo estudiar un posgrado, sino emprender mis sueños, hoy en día algo complicado. Su experiencia ha forjado mi carácter, y con su sabiduría vi otras formas de ver la vida. Gracias por estar siempre conmigo, aunque en lugares diferentes.

A los Doctores Ibarra-Medel, mis hermanos, quienes alguna vez me dijeron que, si me corrían de la maestría, dormiría con Perris. Aunque fuera broma, para mí fue en serio en el aspecto de proponernos objetivos y metas ambiciosas. Gracias a ellos conocí el mundo académico, así como lo maravilloso que es el trabajo de equipo, y el ser multidisciplinario, los tres hablamos del Universo, de la instrumentación especializada para observar desde el cuerpo humano hasta lo visible del universo y de toda la vida, su origen, su existencia y hacia donde podemos llegar, es increíble lo que hemos crecido juntos y ahora somos tres doctores Ibarra-Medel en este mundo.

Al Dr. Juan Manuel, a quien llamarlo mi director no basta. Una persona dedicada a sus alumnos, motivándolos, exigiéndoles, impulsándolos a creer en sí mismos y realizar sus sueños. Nos enseñó a salir de nuestra zona de confort, a vivir experiencias que cambian la vida y abrirte oportunidades con el esfuerzo, sin duda nos ha exigido en estos tiempos de estrés, de incertidumbre, pero nos ha exigido porque a pesar de toda la adversidad, él encuentra oportunidades para mejorar. La ciencia, la educación, la investigación no tiene sentido si sólo se trata de egoísmo y de riqueza. Cuando lo conocí en una entrevista, la pregunta que me hizo fue ¿Por qué quieres ingresar al posgrado?, mi respuesta “quiero aplicar todo lo que he aprendido para beneficio de la sociedad, y por qué no, cambiarle la vida a alguien”. Después de 4 años puedo decir que lo he logrado y que tengo lo necesario para seguir haciéndolo. Gracias, y es por ello por lo que lo considero mi mentor.

A la Dra. Evelyn, sin duda una persona muy alegre, tan alegre que en un principio desconcierta, pero con una agradable aura que inspira confianza. Ella sin dudarlo creyó en mí, aunque yo me olvidé de creer en mí. Es un modelo para seguir, como mujer y profesionista, sin duda le agradezco todo el apoyo y oportunidades de demostrar lo que he aprendido y lo que he logrado. Gracias por su apoyo, ayuda y sobre todo inspiración.

Al Dr. Luis, quien me ha enseñado que tomar decisiones que te lleven al otro lado del mundo te puede dar gratas sorpresas para cambiarte la vida, que nunca dejamos de ser alumnos, aunque seamos doctores y maestros, que, ante todos los títulos y premios, seguimos siendo humanos y que debemos hacer lo que nos hace feliz. Gracias por compartir los momentos más felices de su vida y de su confianza, también por las galletas. どうもありがとう.

A Eloy, sin él a mi lado en estos 4 años, sin duda no hubiera sido igual. Por su apoyo incondicional y confianza, por caminar a mi lado, por prestarme sus libros, por darme ideas, por escucharme, por hacer esta breve historia de nuestro tiempo eterna.

A mis compañeros y amigos, que, aunque cada uno esté librando sus propias batallas, haciendo sus propias tesis siempre hubo un momento en el que convergimos para dar un respiro, para reír y apoyarnos, Gracias Pablo, Gracias Monse, Gracias Luis, Gracias Gil. Estudiantes de posgrado, embarcados en la misma ruta con diferentes direcciones y destinos, pero siempre apoyándonos.

Por último, a la música, sin ella, hubiera terminado en una locura total, aferrada al convencionalismo de hacer y hacer, sin respiros ni momentos para uno mismo. Y aunque no lo crean, a mis gatos quienes se desvelaban conmigo mientras trabajaba por las noches, mirando con la expresión de "deberías estar durmiendo, sin ti todo está frio" y a mis perros, quienes, a pesar de las largas horas de espera, siempre me recibían felices.

Gracias a todos los que participaron en mi formación, a todos los que hicieron posible esta oportunidad. Estudiar un posgrado no es fácil, sin duda terminarlo tampoco. Por cada uno de ellos trabajaré para que otras personas puedan tener esta oportunidad y realizar sus sueños, así como yo la tuve.

Gracias.

A mis padres, María y Eduardo, los seres con los que comparto más información genética en el mundo, los cuales sin ellos literalmente, no podría existir

A mis hermanos, Eduardo y Héctor, por abrir el camino, a quienes en secreto admiro y presumo.

A Evelyn, Luis y Juan Manuel, por su confianza y la oportunidad de creer en mí.

A Eloy, el compañero de este viaje llamado vida.

8 personas de 7 billones en el mundo, que cambiaron mi vida.

For my parents, María and Eduardo, the beings with whom I share more genetic information in the world, without them, literally, I could not exist.

To my brothers, Eduardo and Héctor, for opening the way, whom I admire and presume in secret.

To Evelyn, Luis and Juan Manuel, for their trust and the opportunity to believe in me.

To Eloy, the companion of this trip called life

8 people of 7 billion in the world, who changed my life.

Table of Contents

List of Figures

List of Tables

List of Equations

Resumen

La implementación de la impresión 3D en el sector médico está aumentando en la última década, sin embargo, el costo de los equipos profesionales e industriales es inaccesible para algunos sectores de la sociedad. La tecnología FDM es de bajo costo y con menos requisitos de espacio. El presente trabajo implemento el uso de la tecnología FDM en tres casos de especialidades médicas, para planificación preoperatoria en cirugía maxilofacial, cirugía pediátrica y cirugía de reconstrucción mamaria. El diseño de al menos 30 modelos hápticos para la planificación preoperatoria en cirugía maxilofacial reduce el tiempo de operación en dos horas, lo que reduce el riesgo y la exposición de la anestesia. El diseño de un flujo de trabajo con materiales compatibles con la tecnología FDM para el desarrollo de un modelo de entrenamiento de cirugía pediátrica, para el procedimiento mínimo invasivo, toracoscopia, se construyó en solo 4 días, con un costo de $ 400 MXN, que podría resultar en una reducción de tiempo en curva de aprendizaje, en comparación con los modelos comerciales que cuestan entre $ 2,000 y $ 22,000 USD. La implementación de la ingeniería inversa y la fotogrametría mejoran la planificación preoperatoria de la cirugía reconstructiva de la mama mediante la obtención de un análisis volumétrico utilizando el software CAD / CAM que mejora el procedimiento para una mejor y más precisa selección del tamaño del implante, lo que reduce los resultados en asimetría y no estéticos. En conclusión, adaptando la tecnología de impresión 3D a las necesidades de los sectores más vulnerables y las especialidades médicas, desde el procesamiento de imágenes hasta el post-procesamiento aplicados en cirugía maxilofacial, así como la malformación congénita como EA / TEF, que tiene una menor incidencia y requieren una mayor especialización hasta los padecimientos que afectan a una gran parte de la población, como el cáncer de mama, , pueden beneficiarse de inmediato mediante el uso de todos los procedimientos,

Abstract

The implementation of 3D printing in the medical sector is increasing in the last decade, however, the cost of professional and industrial equipment is inaccessible for some sectors. FDM technology is low-cost and with less space requirements that was implemented in three cases of medical preoperative planning scenarios: maxillofacial surgery, pediatric-neonatal surgery and breast reconstruction surgery. The design of at least 30 haptic models for preoperative planning in maxillofacial surgery produces less operative time, which reduces the risk and exposure of anesthesia in two hours. The design of a workflow with materials compatible with FDM technology developed a pediatric thoracoscopic surgical model prototype designated “EA”, in only 4 days, with a cost of MXN $400 that could result in a shorter learning curve, compared to commercial models that cost between USD $2,000 - $22,000. The implementation of reverse engineering and photogrammetry improved the preoperative planning of breast reconstructive surgery by obtaining a volumetric analysis using CAD / CAM software that improves the procedure for a better and more accurate implant size selection, which reduces the likelihood of outcomes with asymmetry and non-aesthetic conditions. This work suggests that many different pathologies or conditions that affect a large part of the population, such as breast cancer, as well as the much rarer congenital malformations such as EA / TEF, can benefit immensely by using the processes demonstrated, from the taking and processing of medical images through physical manufacturing and postprocessing. Adapting 3D printing technology to the needs of the most vulnerable sectors and medical specialties is a step toward the democratization of medical technology.

Chapter 1: Introduction

"And despite the insignificance of the instant we have so far occupied in cosmic time, it is clear that what happens on and near Earth at the beginning of the second cosmic year will depend very much on the scientific wisdom and the distinctly human sensitivity of mankind."

— ***Carl Sagan*** (1)

The recent evolution of additive manufacturing process has impacted many fields of science and engineering. The Rapid prototyping process today known as "3D printing" has led to a revolution not only in the industrial sectors, but also in everyday society, from home to space. This thesis project will include a brief review of the different technologies of 3D printing, focusing on Fused Deposition Modeling (FDM) technology, due to its low cost in biomedical applications. FDM technology adapts easily to the needs of most sectors of society, including the most vulnerable, without minimizing its effectiveness and quality. The biomedical applications presented in this thesis project refer to pre-operative planning, covering high-incidence medical cases such as the elaboration of haptic 3D biomodels for surgical and implant guides in maxillofacial surgery. Maxillofacial surgery is one of the fields in medicine that 3D printing is creating a great impact and one that we can manage all the capacity of image processing, the use of CAD/CAM systems and inclusive two different 3D printing technology SLA and FDM.

The innovation of technologies like 3D printing in medical procedures that require preoperative planning allowes the reduction in risks and can lead to improved outcomes. The use of 3D printing in the physical recreation of complex pathology can improve surgical skills like the case of Esophageal Atresia (EA) / Tracheo-Esophageal Fistula (TEF) repair. EA is a congenital pathology where the esophagus does not develop correctly, ending in a blind end rather than connecting to the stomach. This congenital defect affects 1/2500 newborns. (2) The importance of 3D printing haptic models in the case of pediatric surgery reduces the likelihood of negative outcomes in the training phase for minimally-invasive thoracoscopic surgery, a procedure demands the highest degree of surgical skills with extremely specialized instrumentation. The design and development of surgical training models can make a difference in the learning curve due the technically challenging

nature of the problem and the high rarity which would not allow many surgeons to have high personal experiences with similar problems.

These same 3D printing processes can also benefit interventions that affect a great part of the population such breast cancer, and can lead to immediate, measurable benefits. One important problem in preoperative planning in breast reconstruction is a lack of volumetric analysis. Most of the reconstructive surgeons still rely on 2D images and subjective visual assessment for evaluating breast volume which varies depending on the experience and the ability of the surgeon (3). The application of reverse engineering in this scenario can help to improve this outcome. The use of 3D scans generates a surface rendering that provides additional information about shape and contour. 3D models can be printed and provide an extra tool in analyisis. The volume of breast volume can be more carefully assessed, enabling the surgeon to devise the optimal size of the implant or flap in order to achieve asymmetrical results.

In this wok, we design and apply the stages necessary for 3D printing to be applied to these selected medical procedures. The medical acquisition, image processing, model design, CAD/CAM simulation, reverse engineering, haptic models, casting, and the selection for the new and experimental materials were performed for all three primary cases. In every case of the implementation, we analyze the advantages and disadvantage, the outcomes, the cost- benefits of each process comparing with the conventional, and how these can be upgraded and develop new strategies which could set the state for a generalized workflow across all medical pre-op procedures that could benefit from 3D printing.

1.1 Objectives

1.1.1 General Objective

Implement 3D printing technology in maxillofacial surgery, pediatric surgery and breast reconstructive surgery, by the design and simulation of haptic models, exploring new materials and procedures to reduce the cost and complexity of the conventional methods, using FDM technology.

1.1.2 Specific Objectives

1. Analyze medical image processing using the Open-Source Software 3DSlicer for preoperative planning in maxillofacial surgery and pediatric surgery
2. Design haptic models for preoperative planning in maxillofacial surgery using FDM technology
3. Implement a workflow for the design of a pediatric training surgical model for a minimally-invasive EA repair approach using CAD/CAM software
4. Explore different materials compatible with FDM technology to mimic the realistic sensation for a pediatric training surgical model for EA repair minimum invasive approach
5. Implement a workflow to obtain volumetric data of the breast by anatomical reverse engineering using photogrammetry technique and 3D Scanning
6. Perform a preliminary economic study applying engineering economics to the developed techniques

1.2 Hypothesis

The implementation of 3D printing, FDM technology, and the use of CAD/CAM process in maxillofacial surgery, pediatric surgery and breast reconstructive surgery, for preoperative planning enhances the understanding of the pathology, reduces risk, costs and time of surgical procedures versus conventional processes.

1.3 Justification

The adoption of 3D printing technology in the health sector can improve the quality of life for society. For the selected pathologies as well as many similar conditions, conventional methods and procedures require time and often elevated costs. Many times, the best solutions are just available for the sector than can afford it, or in regions where the technology is available.

The global populations is increasing constantly at a rate 1.15% annually, and Mexico is slightly higher at 1.26% (4). Although this rate is decreasing, in 2040 the global rate will be 0.70%. Today, only

22.70% of the population in Mexico is over 60 years old, and projecting this number to the year 2040, this number will be 25.01% (5). Mexico is a country where the access to health can be inferred by the proxy indicator of 1.5 hospital beds per 1,000 habitants according to data from World Bank (6). Other health indicators are described in , comparing, different countries. Indicators like hospital beds, risk of catastrophic expenditures for surgical care and population growth highlights the importance to make improvements in Mexico (7). In this circumstance the development and innovation of new technologies to improve the health and wellbeing of the entire population has become a challenge.

Table 1 World Bank Health indicators and data (8)

Indicator	Mexico	Brazil	Chile	USA	Germany	Korea	Japan	World
Hospital beds per 1,000 habitants	1.5	2.2	2.2	2.9	8.3	11.5	13.4	2.7
Surgical procedures per 100,000 habitants	1.3K	13.94k	No data	No data	No data	No data	No data	No data
Risk of catastrophic expenditure for surgical care (% of people at risk)	8.9	12.9	9.4	.8	.1	.4	.4	28.14
Specialist surgical workforce per 100,000 habitants	No data	34.74	65.5	54.71	112.85	49.63	37.34	30.14
Population growth (annual %)	1.26	0.78	0.80	0.71	0.42	0.42	-0.16	1.15
Total Population	129,163,276	209,288,278	18,054,726	325,719,178	82,695,000	51,466,201	126,785,797	7.53 billions

The use of 3D printing has demonstrated to be a high-quality and economically efficient tool in personalized healthcare that tailors to specific characteristics and needs of patients. The conventional methods for preoperative planning rely on the expertise and the subjective perspective of the physicians. However, 3D printing is an additive manufacturing (AM) process that consists of different types of technologies, most of which are expensive and have very limit access in the broader population. The adaptation of 3D printing to the needs of the medical sector that cares the most vulnerable is a key focus of the work presented here. In the case of FDM technology, the most affordable 3D printing method, requires less space, and is in a state of continues development.

The benefit of implementing 3D technology in the medical sector solves one great limitation that doctors go through, which is the dependence of planning through 2D medical images, such as those obtained from computed tomography (CT) scans, magnetic resonance (MRI), and ultrasound, to gain insight into pathologies (9). Furthermore, some current surgical procedures are complex and require guidance and exhaustive preoperative planning to avoid damage and obtain an esthetic outcome like maxillofacial surgery and orthognathic surgery that correct maxillary and mandibular deformities from dental malocclusion, injuries, and diseases like tumors. In this medical discipline the physical representation of the malformity of the skull and mandible improves the analysis of bone quality, skeletal size, symmetry, quantity of bone available based of the reabsorption in the trabecular following tooth extraction (10). The application FDM technology has increased in this medical application due to the low cost of the haptic model instead of using conventional methods that are expensive and require more time.

Haptic 3D printed biomodels provide the design of patient-specific guides and can help in implant shaping for preoperative planning in reconstructive surgery. These reconstructions can be maxillofacial as mentioned before, but can have a much wider impact such as in breast reconstruction surgery where the lack of a volumetric analysis can lead to an incorrect flap, implant shape, and/or asymmetry which not only represents inaccurate surgical outcomes, but can also result in postsurgical psychological problems that can lead in depression and the avoiding of further surgical treatment (11).

The use of 3D printing and its low-cost presentation in FDM technology has a large potential to benefit other much more rare and complex medical scenarios. It can be used to study complex cases and train for procedures that require long times on a very steep learning curve. Examples include

neonatal or pediatric surgery, where congenital pathologies are the most challenging and often highly delicate, and new surgical procedures often requiring minimally-invasive surgery. (2) The conventional training models in pediatric surgery are limited and are not designed according to the needs of surgeons or patient-specific pathologies. Those models that are available for training are not highly adaptable to patient-specific applications and are highly expensive, like the high-fidelity heart sound simulator, "Harvey", with a cost of $75,000.00 USD (12) or NENASim, the Human patient baby simulator with a cost of $22,950.00 USD (13). Patient safety is an ever-growing concern. The time-honored approach of training health professionals at the patient's bedside is not always productive or ideal. Simulation-based medical education solves the time expenses at the patients bedside, avoiding risks, but a high cost. The high costs of many simulators have been a point of criticism and have been considered unethical. (14) (15)

The application of haptic models provides a better understanding between patient and physician. Non-medically-trained individuals, as most patients tend to be, can have a difficult time interpreting and understanding the same information from standard medical images that their physician may be pointing out. Placing a model in the hands of the patient or family and talking them through a given procedure can give a greater understanding of the pathology or proposed work and allows for a more effective question/answer dialogue with the physician.

However, the desire of improve efficiency of the use of 3D haptic biomodel, variables like operation time, accuracy between 3D rendering using CAD/CAM software and printed models, and cost and inclusive exposure to radiation must be analyze.

1.4 Scope and limitations

The AM process of 3D printing consists of different kind of technologies which varies in the process, cost, equipment, and materials. Despite the differences, most 3D printing technologies have been applied in the medical sector for complex cases. This thesis project focused on FDM technology, for its the inexpensive, desktop, accessible characteristics. The materials used in FDM printers are thermoplastics. Some special thermoplastics were used just to mimic the realistic sensation for EA repair training model. Alloys and experimental thermoplastics were dismissed due to the cost and the difficult availability. The FDM printers used were desktop, semi-professional, not industrial. This limitation was not only a budgetary and access limitation, but it also helped provide a real-world

test case for bringing the benefits of 3D printing into complex medical cases in Mexico for a much lower cost than in other regions of the world.

The 3D scans were done using Occipetal's 3D Structure sensor and app suite. MRI was not used to compare the volumetric analysis due to the cost for the patient. Other 3D medical scans like Konica MinoltaVivid 910 3d, BreastSCAN 3D, Cyberware WBX scanner, Crysalix, etc, (16), were not used due to the cost and were not available.

New workflows using the technology available and lower cost were used in the project to propose a new model that can be suitable for public hospitals, universities, schools, private hospitals and clinics.

All the software used in this project were open-source, or by educational license. Specialized engineering software has a high cost, becoming an access problem for hospitals and clinics. The open-source 3D slicer is a research software written in Python to be especially suitable for research and the development of new extensions and functionalities.

CHAPTER 2 Theoretical Framework

"Society needs better ways to understand technology, this has long been obvious. The challenges ahead simply make our need more urgent"

-K.Eric Drexler (17)

3D printing has existed in some form for almost 30 years. This technology was developed by Charles Hull in 1983 in a process known as stereolithography (SLA). This technology was in continuous development, as a result, other variants of this technology were developed like powder bed fusion, fused deposition modeling (FDM), injection printing and contour crafting (CC), selective laser sintering (SLS), Laminated objective manufacturing (LOM), Laser Metal Deposition (LMD). 3D printing is also known as additive manufacturing (AM) or rapid prototyping (RP), direct digital manufacturing, rapid manufacturing. The differences between them are large and include the primary process, materials, and cost (18). However, the ASTM F42 Technical Committee defines additive manufacturing (AM) as the "process of joining materials to make objects from three-dimensional (3D) model data, usually layer upon layer as opposed to subtractive manufacturing methodologies" (19). In the case of FMD technology the most accessible 3D printing technology due to the expiration of the patents and the open source movement leading to a low cost and less space requirements.

Just a few years ago, 3D printing technology was considered an emergent technology. There are several opportunities and advantages in the implementation of 3D printing technology instead of conventional manufacture techniques. For example, cost reduction, simplification of product innovation, price premiums achieved through customization and increasing local production. However, there are limitations that minimize the adoption of this technology, the principal one is the high cost of the equipment and limitation of the materials (20) . The knowledge of 3D printing technology is spreading through a digital platform where individuals expose their capabilities from top-management to lower-level users of the 3D printing uses. However, while the cost of industrial 3D-printers is very high, limiting the adoption of this technology, smaller consumer-grade 3D-printers cost between $500-10,000 USD, lowering the cost every year due to the variety of startup and crowdfunded projects and by developing new technology. This cost has hindered the rapid

adoption of 3D-printing in the consumer market, creating an all-new market for 3D printing technology that demands fast, efficient and effective customized products (21).

The capacities of 3D printing technology are according to the type of process that involves a different kind of materials and precision. New applications are emerging as novel materials and methods are continuously being developed according to de different technologies of 3D printing

2.1 Background

2.1.1 A brief history of commercial, research, and development of the AM process

The experimental research begins in 1960 at Battelle Memorial Institute in Ohio, using photopolymers to create 3D objects. The objective of the research was to polymerize resin using two laser beams of different wavelengths. In 1971 Wyn Swainson founded the Formigraphic Engine Company in California, by using a similar dual laser beam approach, nevertheless , Swainson could not commercialise this technology (22). Hideo Kodama, at the Nagoya Municipal Industrial Research Institute in Japan, developed an AM process using a single laser beam. In 1981, his research was published describing the process of solidifying thin consecutive layers of photopolymers, using UV rays and photosensitive resin (23). This technique by Kodama was the main aspect for the development of SLA. The AM process was patent by Charles Hull in 1986 and was started the foundation of 3D Systems and the beginning of the commercialization of SLA printers in 1988 (24).

Contemporary to Hull's SLA patent, Carl Deckard from the University of Austin Texas developed the SLS process concept. In 1992, Deckard with the founding of Desktop Manufacturing Corporation (DTM Corp), produced the first SLS printers. Later, DTM was acquired by 3D Systems. Stratasys, one of the giant's companies of AM process, was founded in 1989, by Scott and Lisa Crump. They filed a patent for the process of fused deposition modelling (FDM), Stratasys develop the FDM equipment and its materials, thermoplastics (25). 3D Systems and Stratasys created an industry of AM process dominated by them. 3D Systems have been characterized by its business development strategy, which involved setting up national subsidiaries in many countries, aggressively protecting intellectual property, and acquiring competitors like Z Corp.3D systems have even been declared a monopoly (22). On the other hand, Stratasys focused on developing of a single technology, producing a range of machines from desktop to professional functional prototyping printers. By

the end of the 1990s only three companies remained in this space: 3D Systems, Stratasys and EOS (24) (26).

The FDM technology patent expired in 2005, giving rise to the open source movement RepRap. Led by Adrian Bowyer, it had the goal of developing and sharing designs for a 3D printer making it affordable for all the world. The first printer was called Darwin, released in 2007, and the second called Mendel in 2009. Josef Prusa released his own design, the Prusa Mendel in 2010, accelerating the development and improving the printer models. Crowdfunding projects like Kickstarter facilitated the launching of new 3D printing companies, like B9Creator and Form 1 (27).

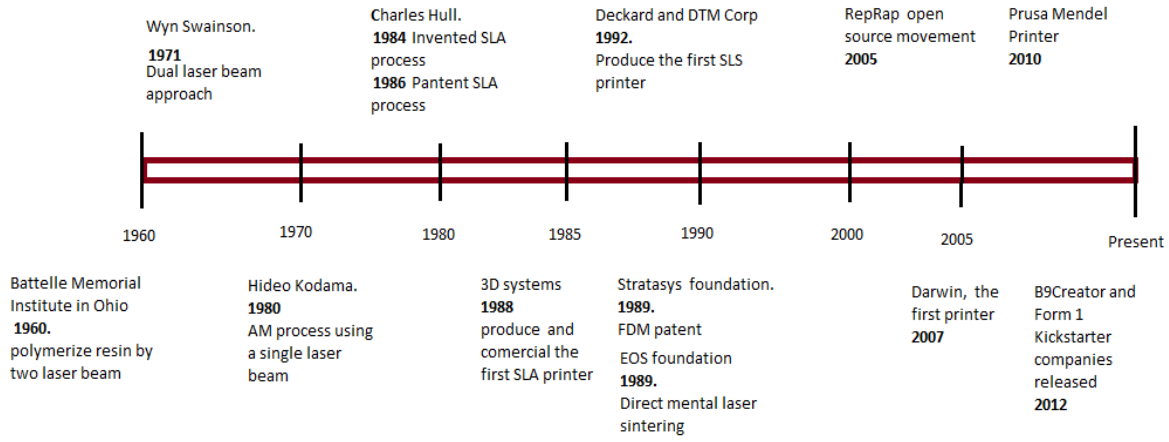

Figure 1 Summarizing of 3D printing industry

2.1.2 3D Printing in surgical applications

The impact of 3D printing in the industry has revolutionized many fields including the medical field. The open source movement extends to research in medical applications that include surgical planning, prosthesis, custom implants, and medical education. The major advantage in the use of 3D printing is the custom-made guides, making medicine personalized. With the continuous development of new equipment and materials for 3D printing, the technology has been adapted to the needs for all the sectors of the society.

3D printing is a rapid prototyping (RP) technique. RP describes computer-controlled machines that can manufacture physicals objects using three-dimensional (3D) computer data. Initially, this technique and machines were developed to enable the design and building of prototypes using computer-aided design software (CAD) to go from on-screen models to a 3D physical prototype with high accuracy. With the advance in computer software for medical imaging, the 3D computer data from medical scans can be used by CADs software and reproduce 3D physical objects from a specific human anatomy structure, rising to a new field of medicine, medical modelling.

In recent years, the 3D printing applications in medicine have been demonstrated in a wide range of surgical disciplines. Despite the continuous development in the medical imaging models, there is still a disadvantage in the visual spatial appreciation of anatomical structures, due to the use of 2D images on a screen, and the lack of tactile appreciation of a 3D digital model.

3D printed haptic biomodels provide a fully 3D, explorable, tactile tool and enhance the appreciation of a complex structure of the pathology and anatomical movements, enabling a prior visual spatial analysis and anticipating possible outcomes of the procedure. This can translate into shorter surgical time, reduced exposure to anesthesia, and bleeding. Furthermore, surgeons have gone beyond printing patient-specific haptic biomodels to printing patient-specific medical hardware, such as implants, prosthetics, external fixators, splints, surgical instrumentation and surgical cutting guides (28).

The design and printing of haptic biomodels is the major application of 3D printing in surgery due two purposes: preoperative planning and education. In the pre-surgical planning stage, 3D haptic biomodels represent the specific anatomic structures, simulating the procedure and allow pre-shaping or testing of surgical tools. The most frequent organ or anatomical structure to design a 3D printed haptic biomedical correspond to the skull and facial structure for neurosurgery and maxillofacial surgery (28).

Maxillofacial surgeries correspond to the region of upper jaw, nose, eye sockets, and the face. The first uses of 3D printing in maxillofacial surgery was in 1998. Kermer and collaborators fabricated 3D printed haptic model using SLA technology with data obtained from a CT scan from a patient suffering from acute maxillofacial trauma (29). Neurosurgeons have used 3D haptic biomodels of complex skull base and craniovertebral junction deformities, corrective surgery in scoliosis patients, atlas neoplasms and atlantoaxial dislocation for preoperative planning reducing operative time and blood loss (9) (30) (31).

After applications in neurosurgery, the medical specialty that is most benefited with the development of haptic biomodels is cardiothoracic and vascular surgery. 3D haptics biomodels helps in planning the procedure for correction of congenital heart disease, such as transposition of the large arteries, ventricular septal defects, pulmonary stenosis and double outlet right ventricle correction (32) (33), as well cardiac tumor resection (34), septal myectomy (35), cardiac schwannoma resection (36), pediatric cardiac transplantation in a patient with a univentricular heart, (37) correction of intracardiac defects (38), ectopic thymoma resection (39), complete aortic arch replacement (40), pulmonary sub segmentectomy (41). In vascular surgery, 3D printed haptic biomodels helps to guide graft fenestration placement for branch vessels, and obtain whole aortic models that most accurately represent the patient's anatomy (42) (43).

The general view of the implementation of 3D printing in medical applications is based on the prototyping of 3D haptics biomodels for surgical planning, as in the procedures mentioned above. Although, in a review by Philip Tack and collaborators, the most frequent use of the 3D models was for surgical guides, followed by models for surgical planning, custom implants, models for implant shaping, and molds for prosthetic and model for patient selection. In addition, they see an increase in the use of 3D printing starting in 2012, which is consistent with the height of the movement and the reduction of technology costs, which makes it more accessible to the public. However, there are reports that evidence the use of 3D printing or rapid prototyping in medical applications before 2010 (18).

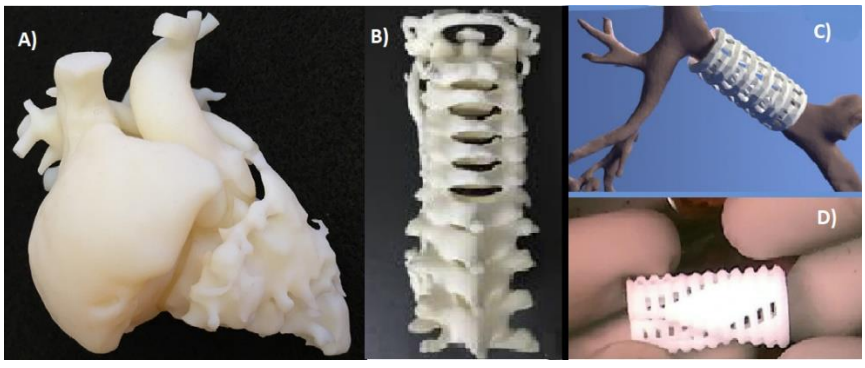

Figure 2 Surgical applications of 3D printed Haptic biomodels. A) congenital heart surgery, 3D haptic biomodel, appreciation of the sites of valvar attachment (44). B) preoperative planning for spinal correction surgery (31)y C) Vascular surgery, Virtual assessment of the fit of tracheobronchial splint over segmented primary airway model. D) Final 3D printed haptic biomodel PCL tracheobronchial splint (45).

The design of haptic models for preoperative planning can be used in teaching medical applications. The teaching of human anatomy consists of the uses of cadavers, or in some cases animals. These practices produce a significant social controversy with medical, legal, and ethical debates. While some institutions remain with the dissection of cadavers, others in Europe have abandoned dissection-based learning. The financial consideration that involves maintaining a cadaver bequest program, accessing cadavers and storage facilities is high without mentioning the safety considerations for students and staff. Costs, ethical, and legal considerations have led many medical institutions and anatomy departments to find alternatives techniques. One of these alternatives is 3D printing, that is expanding and with the open source movement is making it more accessible (46). 3D printing of specimens based on CT scans produced highly realistic 3D replicas in which even small nerves and vessels could be readily distinguished. In addition, printing of sinuses and coronary vessels segmented from CT data was as anatomically accurate as the original clinical radiological data. Additionally, the possibility of scaling up or down in size of the 3D models has produced highly satisfactory replicas of dissections and negative space prints. This is additionally beneficial if the original anatomical structure is larger than the build volume of the printer. Another solution is to print large structures in parts that can be joined manually together (47). However, there is still a lack of materials that mimics the human tissue that are compatible with 3D printing. Depending of the need, several materials may be required for creating a proper replica. The selection of the material is directly linked to the selection of 3D printing technology and the cost and availability. Table 2 represents examples of anatomical reproductions and 3D printers.

Table 2 Summarizing of 3D printing technology and the use for medical anatomy simulation

Simulation	Anatomical reproduction	Technology	Material	Purpose
Bone	Temporal bone (48)	Fused deposition modelling (FDM)	Acrylonite butadienestyrene (ABS)	Drilling
	Head and neck (49)		Plaster (ZP-130)+binder (CA101 cyanoacrolate)	Endoscopic surgery Dissection and drilling
	Cortical and trabecular temporal bones (50)	Binder jetting (Bj)	Hydroquinone+ binder(cyanacrylato)	-
	Temporal bone (51)	Selective Laser Sintering (SLS)	Polyamide+ glass beads	Drilling, buring and suction
Tumor	Skull base Tumor (52)	BJ	Plaster (ZP-150)+binder (ZB-63 clear) wax coating	Investigation of the accessibility of the tumor by evaluating its visibility
Cartilage	Trachea (53)	Polyjet (PJ)	Ruberlike resin (TangoPlusFLX930)	-
	Septum, middle and inferior turbinares (54)	BJ	Plaster (ZP-15)+binder	Dissection and Drilling
Artery	Human pulmonary arteries (55)	PJ	Rubber-like resin (TangoPlus FLX930)	- Transcatheter valve replacement
	Ascending Aorta (56)	BJ	Model infiltrated with polyurethane	
Valve	Mitral valve (57)	PJ	Rubber-like resin (TangoPlus FLX930) shore 27 and 35	Catheter-based interventions: Mitraclip procedure and plugin of a transcatheter device
Heart	Hepatic segments (58)	BJ	Plaster(Zp150)+binder(Z-bond 90)	Cutting and suturing
Cerebral Aneurysm	Cerebral vessel (59)	PJ	Ruber like resin	Clipping the aneurysm
Soft tissue (60)		PJ	Rigid material (VeroBlackPlus RGD875)+Rubber like resin (tangoplus FLX930)	Cutting and suturing

2.2 3D printing technologies

Though different types of AM processes have been introduced by industry, one system to classify AM processes was proposed by the ASTM F42 Committee and classifies AM according to seven areas (19). One category is going to be analyzed in this project according to the material used in the AM process: A) liquid, B) filament, C) powder and D) solid sheet. The different AM process according to de material implemented is summarized in Table 3

2.2.1 Liquid: Stereolithography (SLA).

The first AM technology developed by Charles Hull in 1983, is characterized by the conversion of the liquid photosensitive resin to a solid state by selective exposure of a resin vat to ultraviolet (UV) light. The CAD model is sliced into layers, on each layer, the laser beam traces the cross-section of the part on the surface of the liquid resin to solidify the pattern. The build platform is then lowered by one layer thickness. Then a resin-filled blade sweeps across the parts cross-section, recoating it with a one-layer thickness of fresh resin. The subsequent layer then is scanned, adhering to the previous layer (21) (61). There is a process that has emerged developing a variation in the SLA process. This variation consists in fabricate ceramic and metal parts by using suspensions of ceramic or metal particles in a photo-curable monomer vat (62). New research consists of the implementation of digital mask generators like the digital micromirror device (DMD) to build structures using photo-curable polymers, lowering the cost due to the elimination of an expensive laser system, and is faster because a whole layer is exposed at once instead of scanning with a single laser beam (63). The main limitation of SLA is the final product size, smaller than 60 cm^3, the cost is expensive, the photopolymer costs approx. $ 5,000 -10,000 MXN ($300 to $ 500 USD) per liter (61).

Multi-Jet-Modeling (MJM)

An AM process using a technique similar to ink-jet pritnint but using multiple nozzles. The print head generates jets oriented in a linear array, each jet dispenses UV photo polymer or wax. The MJM

head shuttles back and forth to build each single layer followed by a UV lamp that cures the deposited polymer. As in SLA process, when a layer is completed, the platform descends by one layer thickness and the next layer is built upon previous layer, this process continues until the entire 3D model is finished. The cost-effectiveness is one of the advantages of this AM process, also the shorter build time. On the other hand, a similar process was developed by Israel, Jetted Photopolymers uses wide area inkjets to deposit layers of photopolymers to build parts (21).

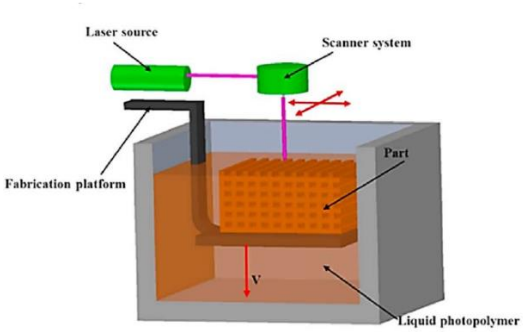

Figure 3 Schematic diagram of additive manufacturing stereolithography (64)

2.2.2 Filament: Fused Deposition Modelling (FDM)

This process deposits a thermoplastic filament that is extruded by a heated nozzle that moves in X and Y axes onto a substrate. The material is heated to a temperature above its melting point and cooled down until it solidifies and forms a layer. New systems have been developed that include two nozzles, creating 3D models with two different materials. A variety of materials are in continuous developed for FDM equipment and the part accuracy can reach $\pm$0.05mm (61). The advantage of FDM equipment is its low space requirements, and the cost of maintenance is low. However, the layer thickness, width, and orientation of filaments and air gap are the main processing parameters that affect the mechanical properties of the final 3D model. The development of new materials for FDM use is based on fiber-reinforced composites that strengthened the mechanical properties. The challenges and innovation are the suitable fibre orientation, bonding between the fibre and matrix and void formation (64). The research and developing of new materials can be suitable for sterilization and with biocompatible properties, that makes these materials suitable for medical use.

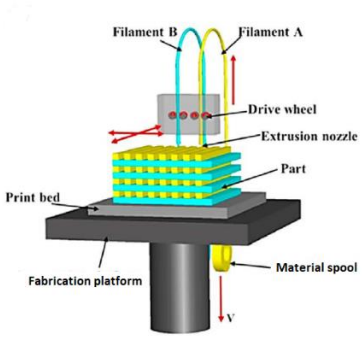

Figure 4 Schematic diagram of additive manufacturing, fused deposition modelling (64)

2.2.3 Powder

The basic principle of this AM process is based on the application of the material in powder form and selective formation of the part by a localized heat source to build each layer.

Selective Laser Sintering (SLS) is a variation in which powder is first spread in a layer and then scanned selectively by a laser, and Laser Metal Deposition (LMD), the powder is sprayed and deposited locally and melted by a focused high-power laser beam. Selective Laser Metal (SLM), is an SLS process focus on print or fabricating metal parts as steel and aluminum. In SLM the powder is fully melted, which results in superior mechanical properties. Another variation is Electron Beam Melting (EBM), this AM process uses an electron beam as the heat source. The fabricated parts are fully dense, free of voids, and extremely strong. Three-Dimensional Printing (3DP) is a powder-based AM process recently developed. In this method, a part is created from the powder bed by selectively spraying liquid binder, which solidifies to form a layer. The 3DP process is quite flexible in terms of the types of materials that can be used and is probably the fastest of all AM processes (61). The combination of a powdered material with a binder can form droplets. Plastic, ceramic, metal and the metal-ceramic composite part can be produced (21). The chemistry and rheology of the binder, size, and shape of powder particles, deposition speed, the interaction between the powder and binder, a post-processing technique are the main challenges in 3DP (65).

Fine resolution and high quality are the main advantages of powder bed fusion, making it suitable for printing complex structures.

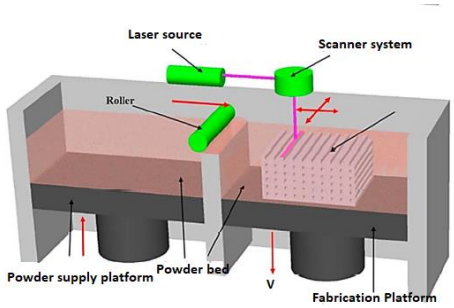

Figure 5 Schematic diagram of additive manufacturing powder bed fusion (64)

2.2.4 Solid sheet: Laminated Object Manufacturing (LOM)

In this AM process, a solid material is supplied in sheet form, cutting a cross-section in the sheet and attaching the cross section to the part being built. The sheet is spread across a movable substrate and a laser cuts it along the contours of the object geometry determined by de CAD model. The layers bond when a hot roller compresses the sheet and activates a heat sensitive adhesive (21). A variety of materials can be used, including paper, metals, plastics, fabrics, synthetic materials and composites. This AM process is low cost, relatively non-toxic and is suitable for larger structures. Post production time is needed to eliminate waste, and to generate accurately functional parts. There is a variation of LOM, the Ultrasonic additive manufacturing (UAM), which combines ultrasonic metal seam welding and CNC milling in the lamination process. UAM is the only method that can create metal structures at low temperature (66) (67).

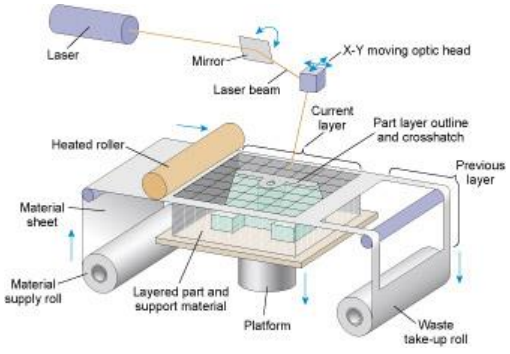

Figure 6 Schematic diagram of additive manufacturing: Laminated object manufacturing

Table 3 A Description of materials, applications of the main methods od AM process (21) (61) (64)

State of material	AM Process	Material Types	Materials	Resolution	Applications
Liquid	SLA	Polymers Ceramics	UV curable resin, Suspension of Zirconia, Silica, aluminia	10µm	Prototype, casting patterns, soft tooling, Biomedical
	MJM	Polymers	Wax, UV curable acrylic plastic	Inkjet: 5-200µm	Prototypes, casting patterns. Biomedical,
Filament	FDM	Polymers, Ceramics Composites	ABS,PC-ABS, PC, ULTEM. Aluminia, PZT,Si3N4,Zirconia, silica, bioceramic, Polymer-metal Polymer-ceramic, short fiber-reinforced composites	50-200µm	Prototypes, casting patterns Rapid prototyping, advanced composite parts, Biomedical, Education
Powder	SLS	Polymers Ceramics, Composites	Polyamide 12, GF polyamide, polystyrene. Alumina, Silica, zirconia, ZrB2, Bioceramic, graphite, bioglass, sands	80-250µm	Prototypes, casting patterns, metal and ceramic preforms. Biomedical, Electronics, aerospace
	SLM	Metals Composites	Stainless steel GP1, PH1 and 17-4, cobalt chrome MP1, titanium Ti6A14V. Metal-metal, metal-caramic, ceramic-ceramic, polymer-matrix, short fiber-reinforced composites	80-250µm	Biomedical, electronics, Aerospace
	EBM	Metals	Ti6A14V, Ti6A14V ELI, cobalt chrome		Tooling, functional parts
	LMD	Metals Composites	Steel H13, aluminum 4047, titanium TiCP, Cu-Ni alloy.		Tooling, metal part repair, functional parts

			CoCrMo/Ti6A14V		
	3DP	Polymers Ceramics, Composites	Acrylic plastics, wax. Zirconia, silica, aluminia, Ti3SiC2, bioceramic, sands. Polymer-matrix, metal-ceramic, ceramic-ceramic short fiber-reinforced composites	80-250µm	
Solid sheet	LOM	Composites	Polymer-matrix, ceramic-matric, fiber and reinforced composites	Depends on the thickness off laminate	Prototypes, c Paper manufacturing , foundry industries, electronics, smart structure

2.3 Medical Imaging

The importance of medical imaging in 3D printing medical applications is to obtain the 3D surface rendering of the anatomical structure to perform an exhaustive postprocessing using CAD/CAM software. There are several scanning modalities, from those normally found in radiology departments to small hand-held scanners that can be found in offices, laboratories or clinics.

Medical images can be obtained in two basic categories: capture data from whole body both internally and externally and those that only capture external data. The first category are medical imaging machines and the second one is 3D surface scanning that originates from engineering disciplines, a process often referred as “reverse engineering” that has been included in medical application by reconstructive surgery.

In recent years there has been a development of high technology and use of various imaging modalities, like how to process and analyze a significant volume of images so that high-quality information can be produced for disease diagnoses and treatment. There are several image modalities and depending of their process can provide more detail of the pathology or structure.

Table 4 Range of application of the most important radiologic imaging (68)

X-ray	**Breast, lung, bone**
γ-ray	Brain, organ parenchyma, heart function
MR	Soft Tissue, disk, brain
US	Fetus, pathological changes, internal organs

2.3.1 Principles of Magnetic Resonance Imaging

The principle of Magnetic Resonance Imaging (MRI) was discovered in 1940s (68). MRI is a tomographic imaging technique that produces images of internal physical and chemical characteristics of and object from externally measured nuclear magnetic resonance (NMR) signals (69). MRI Measures the spatial distribution of specific nuclear spins (usually those of protons) in the body. Electric signals from the spins are measured using precessional motion, or change in the directions of the axis, of the proton spins after they are excited by radiofrequency (RF) pulses in a static magnetic field. The spatial information necessary to generate an image is given by magnetic field gradients that are generated by gradient coils (70).

The relaxation times of proton spins are the most important parameters in MRI. The relaxation times are two-time constants T1 and T2 that indicates the energy emission stemming from the spinning molecules. In other words, is the time by which nuclear spins return to the initial state after irradiation by an RF pulse. MRI also produces a map of the hydrogen density throughout a volume of the patient. As the human body is composed mostly of water, therefore locations that have a high-water content show up in lighter shades of grey and areas containing little or no water show up darker (26) (68). T1 and T2 weighted images are very common in medical applications, and the three types of images used clinically can be seen in Figure 7.

T1 describes the return of magnetization vector along the z-axis (longitudinal axis) is generally used to visualize the degree of saturation or suppression of NMR signal or image intensity because tissues with longer T1 give suppressed NMR signal in T1-weighted. In humans, T1 values of most tissues range from 100-1500ms. T2 characterized the decay of transverse component and describes the lifetime of spin echo signal. T2 values range from about 20-300ms, and is generally used to distinguish pathologic tissues, because proton spins of pathologic tissues usually have longer T2 and

is largely independent of the field strength. This is in contrast with T1 that increments with the Strength of Magnetic field (68) (69) (70).

Figure 7 Three images T2-weighted (T2w), T1-weighted (T1w), and proton density (PD) images, obtained from the same cross section of a human head. Tissues with long T1 are dark on T1W images, Tissues with a long T2 appear bright on T2-weighted images (69)

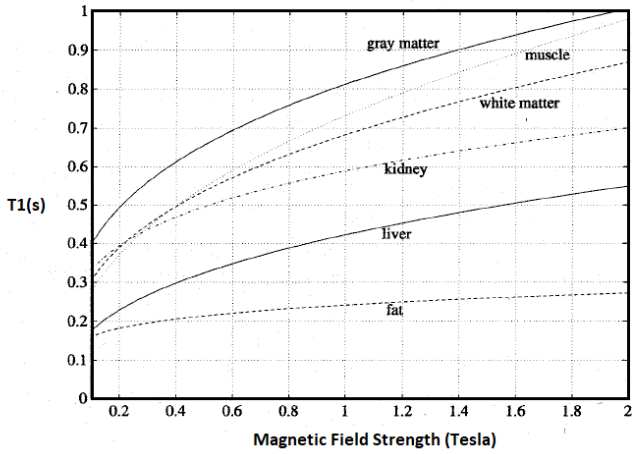

Tissue	T_2(ms)
Gray matter	100
White matter	92
Muscle	47
fat	85
Kidney	58
liver	43

Figure 8 Approximate values of T1 and T2 of some normal tissue types (69)

2.3.1.1 Image quality and Protocol of MRI

The accuracy of a 3D printed haptic models depends of the quality of the medical images. Resolution of the imaging data, presence of artefacts, noise and ease of segmentation as a function of image contrast are examples that influences the result of the medical model. The accuracy can be improved by design of an MRI protocol.

The accuracy of a model with respect to resolution is limited by the imaging technique rather than the printer. In the case of MRI, the cost of resolution comes with time and signal-to-noise ratio (SNR). Conducting 3D MRI scans take significantly longer than a typical session. Conducting an MRI is expensive and increasing the scanning time can cause anxiety and stress for the patient without accounting for the fact that MRI scans are a critical resource in most hospitals (71). For 3D Cartesian imaging, the acquisition of time increases by the square of the resolution, meaning to decrease voxel size by a factor of 2 in all 3 planes (voxel 2*2*2mm3 to 1*1*1mm3) requires a 4-fold increase in scan time. Generally, SNR is proportional to the size of the voxel times the square root of the acquisition time. The configuration of the MRI machine may be enhanced by the addition of more coils, increasing the signal strength, this type of configurations is conducting specially for neurosurgery (72).

The scan distances are other considerations to obtain accuracy results. The scan distances also is referred to as “pitch or distances between cuts,” unlike CT scans, MRI is not limited to the axial plane. To maximize the data available to produce a smooth model, the distances should be minimized. To produce a good result, the distances between scan must be 1-1.5mm. When they are greater than 2mm, the scan will give poor results, as the scan distance increases. However, taking thinner slices results in less signal strength per pixel being detected by the scanner but as more cycles are required, it increase the scan time. A typical MRI scan may be 256 x256 pixels at a pixel size of 1mm (71). A larger number of smaller pixels result in less signal strength per pixel (26).The application of MRI for 3D modelling requires larger time for scan, although MRI is safer than CT scans, the procedures may be uncomfortable and the delays in the radiology departments must be consider.

Anatomic structures like nerves such nerve optic, and brachial plexus, the biliary system and soft tissues like muscles, uterus ovaries and the prostates have a better visualization with MRI protocols that modified the image contrast with techniques such as taking an image with multiple sequences designed to maximize the contrast between different structures needed for the final model. In MRI the sequences determine the tissue contrast. For example, magnetic resonance angiography (MRA) to segment the blood pool of the heart uses cardiac-gated balanced steady state free precession (SSFP) (73), if the myocardium is the region of interest, a black-blood sequence may be more appropriate (74). 3D MPRAGE is well-used for intracranial structures. 3D MR

cholangiopancreatography (MRCP) provides very high contrast and excellent isotropic resolution of fluid containing structures (75) (71).

2.3.1.2 MRI Artefacts

Artefacts must be corrected during MRI acquisitions, if not, artefacts must be recognized by the person segmenting the data. Motion of the body contributes to generate artefacts and is the most common artefact in MRI. Some Anatomic regions of the body cannot remain still, like abdominal breathing motion, and heartbeat, creating ghosting and blurring that severely hinders segmentation. If an MRI with higher resolution is required, it requires more time. In such cases, and particularly for cardiac and thoraco-abdominal imaging, motion compensations schemes are required like using short sequences such as single shot fast spin echo (SSFSE). Flow artefact is caused by motion of liquids within the human body, like blood or cerebrospinal fluid. This artefact overlies normal or pathologic structures. Arterial flow artefact has not only a flowing but also a pulsating component. Blood flowing through a slice can undergo excitation from an incoming RF pulse but might already have left the slice before readout resulting in a vessel appearing be empty or at least less bright. The artefacts caused by flow might even appear bright. If blood flow is slow, a certain amount of unsaturated blood might follow the saturated blood, which has experienced a prior RF pulse (70). Techniques to reduce flow artefacts consists of flow compensations, saturations pulses, and cardiac triggering (76).

Metallic bodies and air-tissue interfaces can cause distortion and obscuration of data. Dense metals object as amalgam, gold fillings, braces, bridges, screws, plates and implants affect the magnetic field, resulting in artifacts in the scan image. The type of metal present determines the extension of the artifact, that can be dark patches or shadows. Metallic artefacts are less pronounced in spin-echo rather than gradient -echo images and can be further reduces using specialized sequences (72).

Figure 9 Flow artefact. The direction of the flow artefact is indicated by the arrows from the popliteal artery occurs along with phase-encoding direction anterior-posterior. (70)

2.3.2 Computed Tomography (CT)

Computed Tomography is a medical imaging modality desirable among physicians due to its speed and accuracy. However, the exposure to ionizing radiation and the potential for misdiagnosis of certain disease are the limitations of this modality. The effective radiation doses in adults are from about 2 mSv (0.2rad) for head CTs to about 8-10mSv for CTs of the chest, abdomen or pelvis CT is well used for a better bone detail, than MRI which provides better visualizations for soft-tissue contrast than CT does (77). CT scans principle consists in pass X-rays through the body and measuring the amount of the x-ray energy absorbed. A standard diagnostic CT scanner includes an X-ray source and a detector, positioned o opposite ends of the patient, mounted on a rotational gantry that can spins this imaging chin at very high speeds. The amount of X-ray energy absorbed by a known slice thickness is proportional to the density of the body tissue. By taking measurements from many angles, the tissue densities can be composed as a cross-sectional image using a computer creating a grey scale image where the tissue density is indicated by shades of grey (78).

Different tissues each have a different X-ray attenuation coefficient, μ. The attenuation coefficients for different materials can be normalized with respect to the coefficient for water (μ_w). This value is expressed as Hounsfield Units as the Equation 1 . The Hounsfield scale is a quantitative scale for the type of tissue (79).

$$HU = 1000 * \frac{\mu - \mu_w}{\mu_w}$$ *Equation 1 Hounsfield Units*

The Hounsfield scale is represented in a CT image as a grayscale for each pixel, whereby each HU represents 0.1% of the attenuation of water. The HU of a region of interest provide insights into the nature of the tissue. Tissues having low Hounsfield scale values darken the film such as lungs and fat, while tissues having higher Hounsfield values lighten the film and provide white spots such as hard bones. Air is represented by a value of -1000, darker, black value, the cancellous bone +700 to +3,000, dense bone (80), for additional information, see Figure 10.

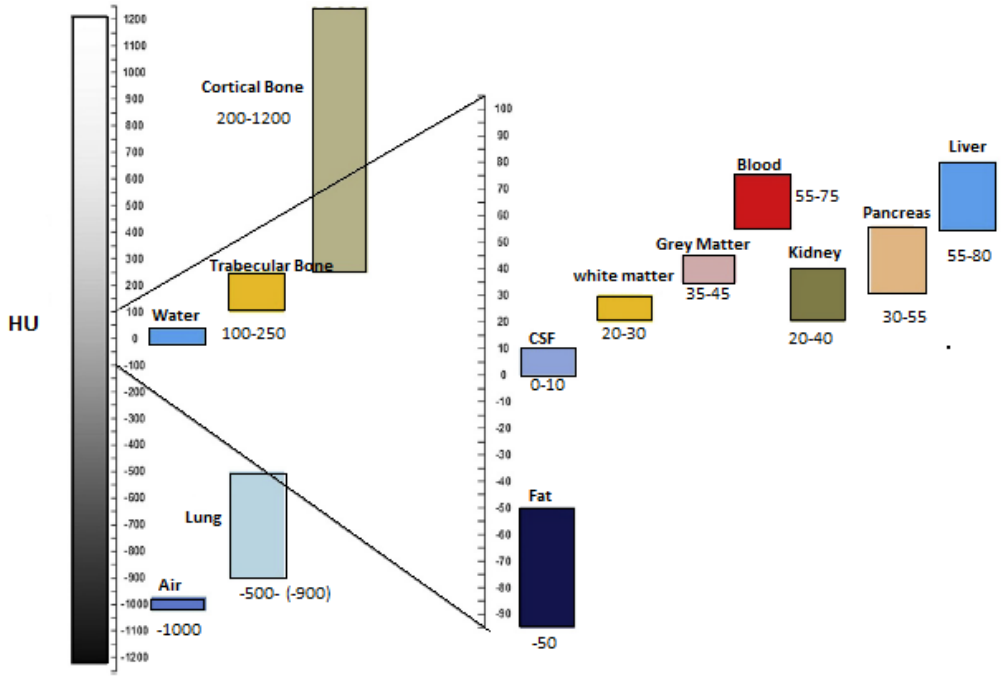

Figure 10 Hounsfield number for different human tissues (81)

CT scans must be minimized particularly in sensitive organs such eyes, thyroid and gonads due the ionizing radiation in the form of X-rays. Artificial contrast agents that absorb X-ray energy maybe introduced into the body, which makes some structures stand out more strongly in CT images. Recent technology allows CT machines to perform scans in a continuous spiral around the long axis of the patient, enabling 3D CT scanning to be performed faster. 3D CT scans are referred as a helical

CT. Modern CT scanner employ multiple arrays to enhance the rate of data capture and improve 3D volume acquisition. The slice thickness is the distance between a series of axial images. An interpolation is made from one image to the next to form cuboids, referred as voxels generating a 3D CT scan (26).

2.3.2.1 Image quality and protocol for CT Scans

CT volume is defined by the number of axial images taken and the field of view used for those images. The axial images consist of a fixed number of pixels, 512 *512. The field of view is the physical distances over which the images is taken. The field of view may be reduced to capture specific small areas of the required anatomy resulting in a smaller pixel size, increasing the physical accuracy of the scan. A CT scan of the head would be ~25 cm resulting in a pixel size of 0.49 mm while a field result in a pixel of 0.25 mm. To maximize the data acquired, the slice thickness should be minimized as 0.5mm, this value gives excellent results but a cost of increasing X-ray doses. The typical distances of 1-1.5 mm produce acceptable results. Scanning distances of 2 mm are adequate for larger structures such as long bones or pelvis. A scan distances greater than 2 mm will give poorer results. Another aspect of image protocol is the collimations. Collimation describes the thickness of the X-ray beam. The Scan distances and collimation should be the same, however using a slice thickness smaller than the collimation gives an overlap. The overlap may improve results when scanning for very thin sections of bone that lie in the axial plane. For 3D printing process, gantry tilt should be avoided, because provides errors in the images processing. Large gantry tilt angles are visualized in visual inspection and can be corrected but small angles may not be visualized and corrected them is difficult (82) (26). An example of gantry tilt compensation is illustrated in .

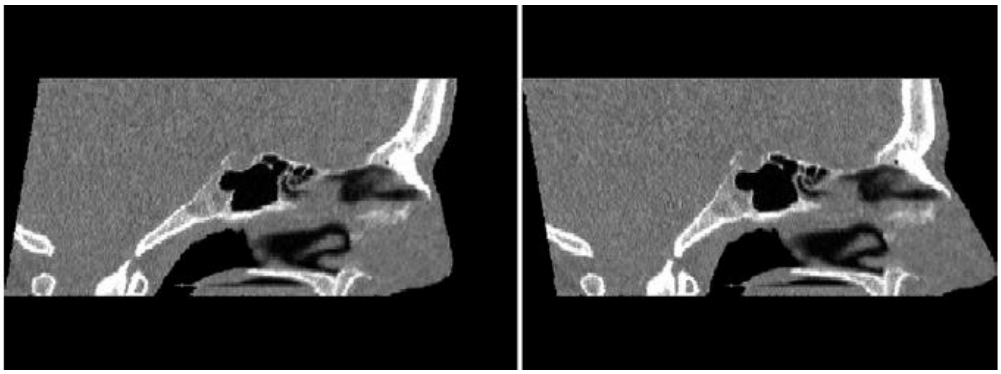

Figure 11 CT scan of superior maxillar representing an Uncorrected gantry tilt (left) and correct compensation (right) (26)

2.3.2.2 CT Artefacts

Artefacts are common in CT scans and may be considered as a source, or type, of noise. An artefact is any distortion or error in an image that is unrelated to the structure being studied. The origin of artefacts in CT images is the interaction between the subject and the machine and may be produced depending of the nature in source: Errors in X-ray attenuation measurements; alterations in the energy spectrum of the X-ray beam (beam hardening) as it passes through the patient; the presence of high-density foreign materials in the body; partial-volume averaging effect; motion of the patient; quantum mottle (noise); malfunction of the detector arising from errors in detector calibrations and balance, geometric effects, or machine peculiarity; inadequate temperature, humidity or the presence of small dust particles within the computer that causes and inadequacy in the reconstruction algorithm (83).

The artefact that from motion of the patient is visualized as black or white bands, dark spots, loss of resolution or distortion of anatomy (84). Theoretically, motion artefacts can be reduced by fast scanning, gating, tube alignment, corrective reconstruction or postprocessing of the scan. Precise control of fan-beam position is important for obtain high quality CT images. Performance of CT systems relies mainly on geometric precision and measurements quality. Inaccurate geometry, inaccurate alignment of X-ray tube with the detectors produce artefacts and blurring that limit spatial resolution (85). Beam-hardening artefacts result from the preferential absorption of low energy photons from the beam, this artefact is more pronounced in areas of large attenuation such as bone. The artefact manifests as a shadow beneath ribs. This effect can be compensated for using special filters or correction algorithms. Objects that have high or low attenuation can generate streaking artefacts by forcing the detectors to operate in a nonlinear response region (86). Objects such as amalgam or gold fillings, braces, bridges, screws, plates and implants scatter X-rays resulting in a streaked appearance in the scan images, as see in Figure 12. Metal fragments produces a star patterning the star effect is accentuated by motion. To avoid this artefact is changing the angle of the slice to exclude the foreign body. When tissues with different absorption occupy the same voxel, the beam attenuation is proportional to the average value of the attenuation coefficient of the voxel. A volume average is computed for such voxels, leading to the partial-volume error (83) (80).

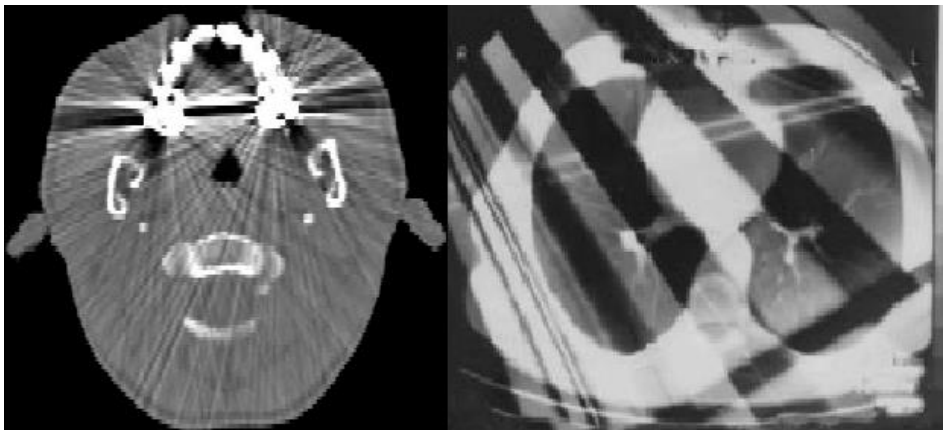

Figure 12 Common artifacts in CT scans, X-ray scatter artefact (left), Black and white bands and blurring artifacts on lung produced by inaccurate X-ray tube geometry (right) (83) (26).

2.3.3 Cone Beam Computed Tomography (CBCT)

In the last decade, Cone beam CT (CBCT) machines became available around the world. This medical image modality has become in the standard technique for 3D planning of implants. CBCT has many advantages over CT, the major one is the lower radiation dose to the patient, shorter acquisition times, lower cost and submillimeter resolution. Unlike the x-ray fan-beam geometry of conventional CT scanners, CBCT produce an X-ray beam in a conical configuration that enables a volume of tissue to be imaged in a single rotation (Figure 13). The cone angle of the X-ray beam can be increased by increasing the anode angle in the X-ray tube. A rectangular or round two-dimensional (2D) detector captures the projection data of the entire region of interest in a single rotation (87).

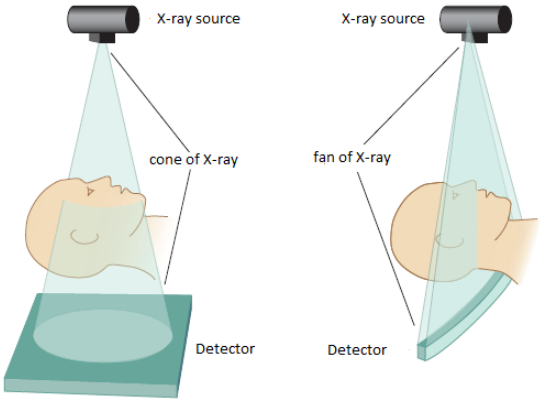

Figure 13 Schematic of the X-ray source configuration in (left) CBCT vs (right) fan-beam computed tomography (87)

A flat-panel detector converts X-ray energy into electrical signals for digitization. The imaging chain of a flat-panel-based CBCT scanner can be mounted on multiple different types of mechanical gantries for rotation, including specialized gantries for dental and maxillofacial images specially in temporal bone imaging, sinonasal imaging, musculoskeletal imaging, breast imaging, and imaging of implant devices, inclusive small-animal imaging, tissue engineering experiments and intraoperative imaging (88). CBCT equipment is implemented as a seated scanner such the imaging chain is rotated around a vertical axis with the patient seated at the isocenter, making it suitable for use in an office (78).

2.3.3.1 Image quality and protocol for CBCT

CBCT scans uses lower radiation dose than conventional CT, however the difference relies on the machine and the parameters used (Figure 14). Studies that have used dosimetry, phantoms based on craniofacial model cite reductions in the order of 15 times less than conventional CT. The voxel size of CT scan can be 0.5mm, Instead CBCT produces isotropic (equal in the X-Y-z dimensions) voxels as low as 0.076mm. Small fields of view correlate to increased resolution in a very local area. A small or focused field of view would be on the order of 5 cm or less, where 15 cm or more may be required for craniofacial applications. (26). CBCT has a high spatial resolution (150 µm), high volume coverage, ability to perform fluoroscopy/angiograph in conjunction with tomography, and the ability to monitor a temporally-evolving process. In CBCT imaging, spatial resolution is determined by many factors, such as focal spot size, detector element size, smoothing filter and reconstructed voxel size. However, CBCT has a lower contrast resolution, slower decay time of scintillation material and longer scan time (89). The lower contrast resolution is due to increased X-ray scatter in cone-beam acquisition and lower detective quantum efficiency compared with multidetector (87).

As in CT scans, in CBCT, the degree of x-ray attenuation is shown by gray scale (voxel value), however it is common that manufactures and software present gray scales as Hounsfield Units, but is important to be clear that the grey scale values are not true HUs. Although, there are studies that have shown a linear relationship between HU in CT scan and grey scale in CBCT and suggested that voxel value in CBCT can be used for estimation of bone density (90) (91).

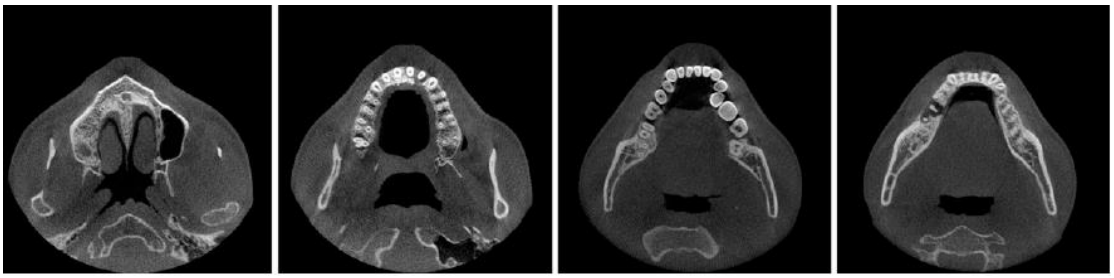

Figure 14 Reconstructed axial CBCT for mandibular section (92)

2.3.3.2 Artefacts

Noise in CBCT is higher than in conventional CT scans due to a relatively high amount of electronic noise in the detector and other factors. In the cases of artefacts in CBCT, the major source is X-ray scatter, which can result in shading and streaks similar appearance to beam hardening effects. X-ray scatter artefacts arise from data inconsistencies associated with X-ray photons undergoing Compton interactions in the patient and reaching the detector. Such false increases in signal results in and underestimate of attenuation values, for example, a darkening of the image reconstruction. Antiscatter grids can be employed to reduce X-ray scatter reaching the detector but may carry an increase in dose. Other common artefacts in dental CBCT are metal artefacts, which are the result of high X-ray absorption by high-density objects. Various effects contribute to metal artefacts, and the manner in that they appear in the image depends on the severity of these effects and the way the reconstruction algorithm deals with them (93). One contributing effect, that even occurs without the presence of metal is beam hardening. In the X-ray spectrum and the tube parameters section, an X-ray beam consists of a spectrum of energies with a maximum energy determined by the kVp and a mean energy at about 60% of the maximum. When passing through a material, low-energy X-rays have greatest probability of being absorbed, and the mean energy of the beam increases, like filtration. Beam hardening can occur at any beam energy and for any material and tends to be more pronounced for low energy beams and for denser materials. Other common artefact in dental CBCT is caused by the diameter of the FOV usually does not cover the entire patients head, truncation artefacts may occur. Another source of artefacts is patient motion (92).

An artefact that is produced by the hardware machine limitations and costs, is the use of a smaller flat-panel configuration with the source-detector axis positions offset to the center of rotation, resulting in the central part of the reconstructed volume is scanned over complete 360° rotation,

while locations at the periphery are only scanned over a 180° half-rotation. This abrupt transition results in a ring artefact in this area in the axial planes (93).

2.3.4 3D Medical Surface Scanning

3D scanning systems rely on light-based data acquisition. It is more practical and comfortable to obtain data from external shape or skin surface. Unlike CT and MRI, 3D scanning capture only the exterior topography of the patient to measure body shape and size, inclusive texture and color to diagnose and decide treatment/health status. The use of 3D scanners for medical application is emerging to facilitate the design of implants and eliminate manual measuring processes. As an example of the noninvasive power these techniques can have, the digital data obtained by 3D scanning can be applied for the creation of holograms and can be used for detecting scoliosis from a patient's back shape (94), There are many additional applications in sports performance and security (95).

This technology uses software and algorithms that automatically extract measurements during scanning and eliminates transcription and measurement errors. The principle of 3D scanning devices is like that of cameras, where many images are combined to construct a virtual 3D model. 3D scanning can be time-consuming and, in some cases, expensive, but is generally safe. There is less discomfort for the patient and no distortion of soft tissues caused by the pressure applied when taking casts or impressions. This technology combined with the ability to manipulate data makes the approach suitable to applications in prosthetic reconstruction and rehabilitation (26) (96).

3D scanning techniques depends on "line of sight", that means that areas that are obscured or a too great an angle to the line of sight will not appear in the scan data. Depending on the shape of the object, many scans may be necessary. Despite using multiple scans, some areas may remain difficult to capture. Transparent, dark or highly reflective surfaces can cause problems when 3D scan. As with the other medical image modalities, the movement of the patient during the scan will lead to poor data. If there is enough overlap between adjacent scans, they can be aligned by suitable computer software. 3D scanners capture many thousands of points at a tie. Most of these points will fall accurately on the surface of the object being scanned. However, due to tolerances and optical affects some of these pints will deviate from the object surface. If enough points deviate from the surface, it will affect the quality of the data, these errant points are referred as noise.

Filtering selectively removes data points that deviate greatly from the vast majority of neighboring points

Three main process are used to create 3D models: photogrammetry, stereo vision, and fringe projection.

2.3.4.1 Photogrammetry

Photogrammetry is a field of science that consists in the acquisition, accumulation and transformation of information about the shape of an object, its location against other objects in space, and its movement or deformation (97). Photogrammetry images can be made in various wavelengths of electromagnetic radiation, the most common is the visible range, microwaves and X-rays are also used. Cameras and scanners are used for the visible and infrared bands.

Photogrammetric methods are used most frequently in orthopedics and in dermatology to examine the surface of the skin to facilitate early melanoma diagnosis (98), in forensic cases to analyze the damage to hard and soft tissues (99), in dentistry to study the morphology of the facial skeleton, orthodontics and orthognathic and reconstructive surgery (100).

2.4 3D Geometry in Medical Image Processing

This section describes how medical image data obtained from medical images modalities are processed to obtain a 3D haptic biomodel by using CAD software for further analysis.

The process of generating 3D objects from medical imaging data requires an analytical process. The first step is the acquisition of image data, obtained from medical images modalities such as MRI, CT scans, CBCT , and even ultrasounds; the second one is the extraction of the chosen region of interest, using segmentation algorithms, the third is transformation of the data from volumetric to a 3D triangular mesh, and finally transfer of the data to a 3D printer.

The image acquisition consists in manipulated medical data. Medical data can be acquired using medical image modalities saved in a specific format. Digital imaging and communications in medicine (DICOM) is an internationally standard for all medical imaging modalities. The DICOM standard format enables the transfer of medical images to and from software and scanners from different manufacturers and aided the development of picture archiving and communication

systems, which can be incorporated with lager medical information or record systems. DICOM format includes data such as patient name, reference number, study number, dates and reports (26).

3D medical models can be printed from any volumetric image dataset that has enough contrast to differentiate tissues. CT images are most commonly used for 3D printing because the relative ease of image postprocessing. The high contrast, signal-to-noise ratio, and spatial resolution enhance structure differentiation an minimize partial volume effects that could limit 3D printing (101).

As we describe in 2.3 Medical Imaging, MRI, CBCT and CT images consist of grey scale pixels. It is advisable to work with the original data rather than any 3D reconstruction derived from it, that is the reason why medical images are often manipulated in the pixel format. However medical images are presented in 2D in which the element is pixel, as well in 3D domain, represented by voxels. In some cases, 3D images are represented as a sequential series of 2D slices as see in Figure 15.

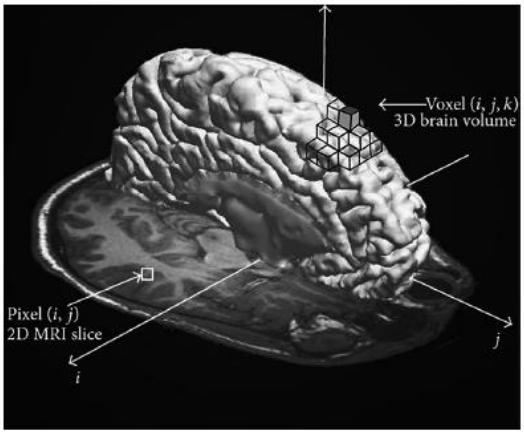

Figure 15 Representation of pixel and voxel elements on a brain obtained from MRI scan

2.4.3.1 Medical image processing

Medical images can be considered a cluster of voxels in 3D space where each voxel represent a CT value or HU value associated with it. In medical image processing the implementation of algorithms like image segmentation are necessary. In an image segmentation procedure, whether manual or using and algorithm, voxels can be sub-grouped for a range of values which will provide the 3D

geometry for that range. A preset threshold value can be assigned to generate a volumetric region in different software. This preset threshold value can be different for bones and soft tissues.

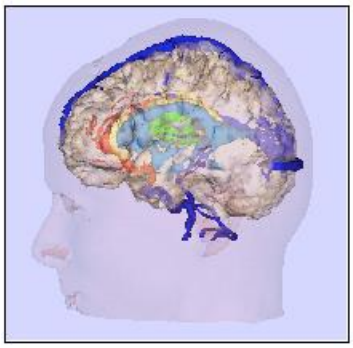

Figure 16 3D rendering of segmented skin surface (pink), brain tissue (brown), major blood vessels (blue) and tumor (green) from MRI. (69)

Image segmentation is defined as a partitioning of an image into regions that are meaningful for a specific task like the detection of a brain tumor form MR or CT images. Segmentations is one of the first steps leading to image analysis and interpretation. Image segmentation approaches can be classified according to the features and the type of techniques used. Features include pixels intensities, edge information and texture. Techniques based on these features can be broadly classified into structural and a statistical method (69).

Structural methods are based on the spatial properties of the images like edges and regions. However, such algorithms are sensitive to artifacts and noise. Region growing is another structural technique, in which one begins by dividing an image into small regions, “seeds”. Then all boundaries between adjacent regions are examined, strong boundaries are kept, and the weak boundaries are rejected. The process is carried out iteratively. Statistical methods label pixels according to probability values, which are determined based on the intensity distribution of the image (69).

The medical image processing consists in extraction the region of interest (ROI) through and automatic or semiautomatic process. As mentioned before, image segmentation has been used in medical applications to segment tissues and body organs(Figure 16). Some of the applications consist of border detection in angiograms of coronary, surgical planning, simulation of surgeries, tumor detection and segmentation, brain development study, functional mapping, blood cells automated classification, mass detection in mammograms, image registration, heart segmentation and analysis if cardiac images. Medical research segmentation techniques have been employed to differentiate tissues form each other, through extracting and classifying features (102).

2.4.3.2 Region-based methods and thresholding-based methods

Region-based methods refer to methods where a region is composed of some pixels which two by two are neighbors and the boundary is made from differences between two regions. Thresholding and region growing are the most popular region-based methods

Thresholding is considered the simplest and fastest segmentation methods based on the assumption that images are formed from regions with different grey levels. The histogram of images has different grey levels. The histogram of images has different peaks and valleys which can divide images into different parts (Figure 17). Threshold is a value in a histogram that divides intensities into two parts one considers the foreground, having pixels with intensities greater than or equal to the threshold and the second part is the background, having pixels with intensities less than the threshold. An inappropriate threshold value leads to poor results. Multi-thresholding is used to separate multiple objects with different grey values (102).

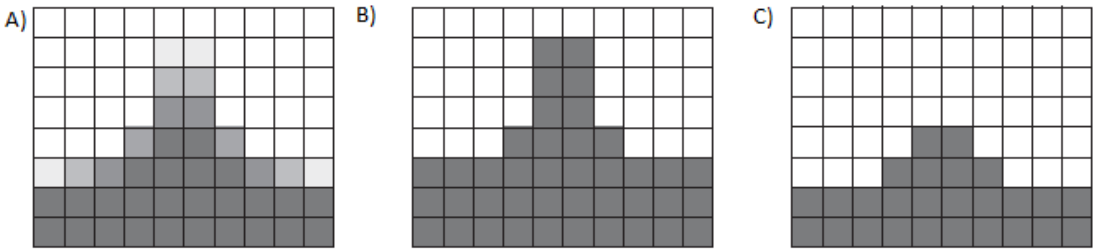

Figure 17 A) Original CT image, B) effect of a low threshold C) The effect of a high threshold (26)

However, thresholding segmentation does not consider the spatial information of images which lead to sensitivity to noise and intensity in homogeneities (103). Inhomogeneity in the imaging equipment and the partial-volume effect (multiple tissue class occupation within a voxel) give rise to a smoothly varying, non-linear gain field while the human visual system easily compensates for this field, the gain can perturb the histogram distributions, causing significant overlaps between intensity peaks and thus leading to substantial misclassification in traditional intensity-based classification methods. This occurs in joints (69).

Thresholding-based methods are effective for obtaining segmentations from images with well-defined contrast difference, usually performed in CT scans, because of HU values. The presence of abnormal imaging patterns affects this class of methods.

Region-growing is an interactive segmentation method which requires seed points as explained before. This method separates a region of images based on some predefined law according to intensity information. Region growing requires one seed point and the region will be growing based on its homogeneity properties according to neighboring pixels (Figure 18). There are some region-based methods which have differences in homogeneity criterion definition. However, the result significantly depends on the seed point selection and the selection of the seed relays in the expertise of the researcher (104). Although noise sensitivity is less than thresholding, but it can make a hole in the extracted shape or produce a disconnected area. Is only required for a single pixel (0.25 mm) to connect two regions for the software to assume that they are the same structure. Therefore, structures that are separate but in proximity or contact may need to be separated manually before region growing is applied (26).

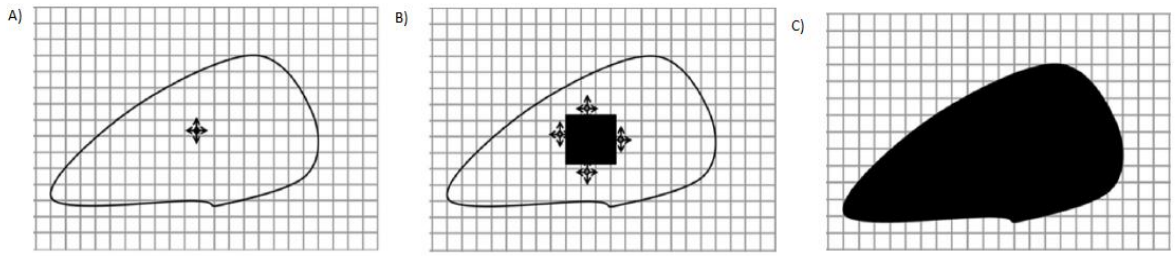

Figure 18 A general representation of the region-based segmentation: approaches start with a seed point and then grow as they add neighboring pixels or voxels to the evolving annotations as long as the neighborhood criterion is satisfied A) shows the initial point, the seed point (black circle) and growing direction) growing process after a few iterations (black area) C) final segmentation.

Region-based segmentation serves as an efficient tool for extracting homogeneous regions such as lungs with no to mild pathological conditions, or as tumor detection in mammograms. In addition to region-based methods, other methods that have been introduced include watershed transform, graph cuts, random walks and fuzzy connectedness. In terms of efficiency, region-based methods are considered efficient because the timings and the computational cost. One potential weakness tradeoff for this efficiency is that the repeatability of the segmentation using this method depends on the location of the seed point (105).

2.4.3.2 3D Meshing

Certain software packages can import DICOM images, segment data, and create a mesh file. These include open-software such as 3DSlicer (https://www.slicer.org) Osirix (Pixmeo, Geneva, Switzerland), and ITK-Snap (http://www.itksnap.org), as well as commercial software such as Mimics (Materialise Interactive Medical Image Control System; Materialise, Lueven, Belgium) and Vitrea (Vital Images, Minnetonka, MN)

After the medical image processing is complete, a surface is extracted from the volumetric data by converting the data from voxels into a mesh composed of a series triangular facets touching one another without overlap as seen in Figure 19. The voxel surface is smoothed to the Stereolithography (STL) format, also known as "standard triangle language" or "Standard Tessellation Language" and can be exported for mesh generation for further analysis.

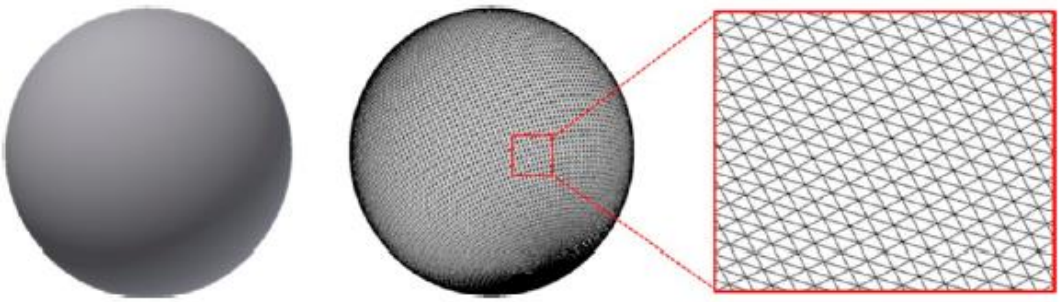

Figure 19 Representation of information in a STL format. The surface of the object is triangulated. (106)

Meshes can be developed by different methods from CAD surfaces depending on the type of mesh needed for the analysis. The types of mesh and the association with different types of surfaces retrieved through medical images can be categorized in three ways: unstructured mesh, mixed mesh, and structured mesh.

The unstructured mesh made of tetrahedral elements can be achieved directly from voxel matrix 3D CAD enclosed volumes for ROIs from medical scans. Algorithms like Delaunay meshing are used to generate the mesh, as well as grid-based methods (voxel and volumetric marching cube meshing) can be used directly to convert voxels from 3D medical image to unstructured tetrahedral or hexahedra mesh. The voxel-based method can be used to capture details of the complex human body shapes, like bridging vein structures in brain segmentations, heart valves in different chambers

and trabecular architecture. The accuracy of meshing theses detailed geometries deepens mainly on resolution and segmentation efficiency of algorithms. Structured meshes consist of continuous hexahedral elements, are preferable due to satisfying the basic requirements behind FE-based approach for solving physics problems. However, there is no fully robust, automatic algorithm available, and therefore the hexahedral meshing of complex assemblies with components having nonuniform geometries like the human body is quite consuming laborious. (81)

2.4.3.2 Mesh optimization for 3D printing

The mesh must not have any holes/tears in its surface. The process to optimize the mesh is called "creating a manifold model" and verify that the model is "watertight". Sometimes the 3D surface rendering doesn't have a determined wall thickness. Some software provides and further analysis to check that the mesh has a minimal thickness of the wall of the 3D object. Wall thickness is simply the distances between one surface and its opposite. Internal overlapping or surface interference is considered error in the mesh. There is software that can solve this problem automatically, and in complex cases the implementation of a Boolean operation can be done. To determine the model volume of an object it is necessary to distinguish between the inside and outside of a surface mesh. A reversed face or inverted normal means that the surface of the mesh is facing in the wrong direction (107).

There are several methods to optimize a mesh to balance surface representation with the file. Decimation may be required to reduce the number of faces of an overall mesh or a portion of a mesh reducing the size of the file and data processing may be accelerated as a result (Figure 20 y Figure 21). However, the increment of the facets around topographies with high curvature to increase the surface quality, dividing the existing mess by a factor. The tessellation of meshes may also be adjusted to suit preferences; with relatively consistent curvatures, a mesh can be retriangulated (26).

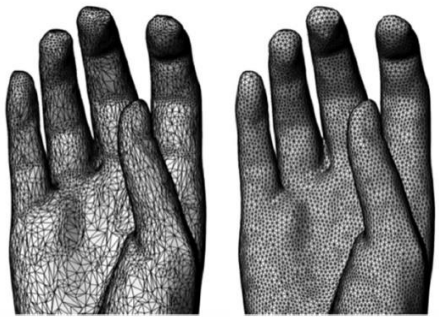

Figure 20 Effect of remeshing, left decimated scan, right remeshed with a maximum 2mm edge length

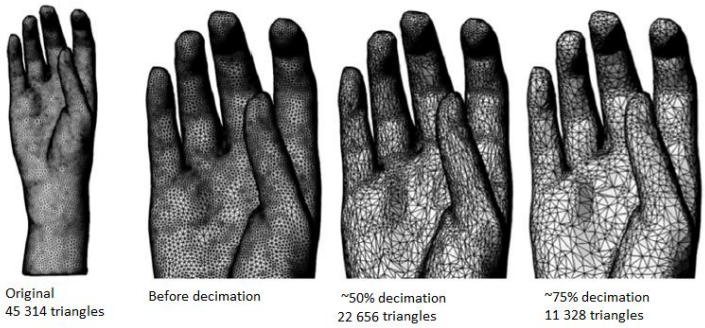

Figure 21 Effects of decimation on geometry and facet count (26)

2.4.4 Converting DATA STL to GCode

The STL file format, developed by Hull at 3D systems, has been accepted as the gold standard for data transfer between CAD software and 3D printer. The STL format stores the information for each surface of the 3D model in the formulated sections, where de coordinates of the vertices are defining in a text file. The first line describes the direction of the facet normal. This indicates which surface is the outside of the facet, the subsequent three lines gives the coordinates of the three corners or vertices of the facets. STL files can be in binary or text (ASCII). Binary format is smaller.

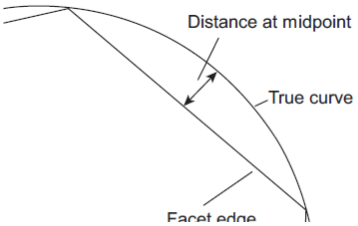

Figure 22 Facet Deviation (26)

STL files can vary in size from 50KB to hundreds of megabytes. Highly complex parts may result in excessively large STL files. The resolution parameter of the STL file can be specified as the maximum deviation (Figure 22). The deviation will be the perpendicular

distance between a facet and the original CAD data. Smaller deviation represents more accurate representation of the CAD model, with a greater number of facets (26). The 3D printer interprets the coordinates derived from STL file by converting the file into a G-code via slicer software. The G-code divides the 3D STL format into a sequence of two dimensional horizontal cross sections, which allows the 3D object to be printed, starting at the base in consecutive layer (106).

2.5 Maxillofacial Surgery

Obtaining highly accurate anatomic biomodels can facilitate preoperative planning and improve postoperative facial contour symmetry in various surgical interventions such as reconstruction of the mandible, the maxilla and the orbits. Improving and practice of different techniques results in a reduction of the operating time and minimizes errors. Virtually planning and printing pre-contoured grafts and plates can improve surgical outcomes and reduce operating time. Another application is offering high-accuracy prostheses that can enhance the aesthetic and psychological status of patients suffering from significant scarring, deformation and asymmetry. There have also been cutting-edge simulation models to enhance surgical education proposed (108).

Three-dimensional planning is a routine technique for procedures such as dental implants and orthognathic surgery. Its advantages include more precision, fewer complications and reduction of the operation time. Recently, surgical cutting and positioning guides were developed to treat a wider spectrum of maxillofacial deformities and conditions (10).

Reconstruction models can be employed when a patient suffers fracture of the chin and jaw from trauma. In other patients, cancer may spread to a region of the jaw and the infected tissue needs to be removed. Three-dimensional printing may be applied to replace the entire jaw or a portion of the jaw. This is done through a powder metallurgy-based AM process known as selective laser melting (SLM). Bioresorbable maxillary and mandibular implants using calcium phosphate have also been fabricated (109).

Orthognathic surgery is used to correct maxillary and mandibular deformities from dental malocclusion deformities injuries, disease, as to improve the facial appearance

In the case of implant guide planning the surgeons needs to ensure the size and correct placement of implants. This can be done using dental software, but the visual-spatial appreciation is needed. Using CBCT and 3D haptic biomodels, bone quality, bone quantity or density such skeletal size. The success of dental implants depends in the quantity of bone available based of the bone resorption in the trabecular following tooth extraction.

2.6 Esophageal Atresia (EA)

The first record of a baby with esophageal atresia (EA) was in 1670, however it was not until 1939 that a baby survived a surgical intervention (110). EA has a spectrum of anomalies and several categories have been described. The distal tracheoesophageal fistula (TEF) is the most common variant in the EA spectrum and occurs with a frequency of 85-88% of all EA cases (111). The proximal esophagus is hypertrophied and dilated from amniotic liquid pressure. Second most common anomaly is pure EA 8% associated with poorly developed distal esophagus, A representation of all types of EA is showed in Figure 23 (112).

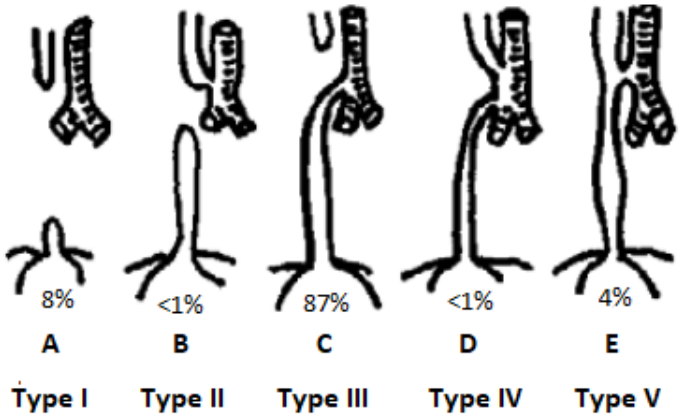

Figure 23 Types and frequency of esophageal malformations (112)

EA occurs in one of every 2,500-5,000 newborns with a slight male predominance of 0.5-1 above the average. The risk of having a baby with EA increases after the first pregnancy, with older mothers and twin pregnancy. Teratogenic influence has been identified after prolonged use of estrogen, progesterone or thalidomide during pregnancy and infants born to diabetic mothers (112).

The symptoms appear in the first hours after birth. The symptoms are excessive salivation, first feeding causing reflux, asphyxia and cough followed by cyanosis, respiratory distress and inability to pass an orogastric tube. The diagnosis of EA is confirmed after watching a coiler orogastric tube in the proximal esophagus in simple chest x-ray films. A constant distance of 10-11 cm between the bars and proximal esophageal pouch is most often found (112).

The first thoracoscopic repair of EA was performed in Berlin in 1999. The first thoracoscopic repair of EA and TEF was in 2000. The mean patient age at operation is 1.2 days, the mean weight is 2.6

kg, the mean operative time is 130 min, the mean days of ventilation is 3.6, and the mean days of hospitalization are 18.1.

The surgical technique consists in positioning the baby in a supine placement on the operating table and the oropharynx is suctioned following bronchoscopy, the baby is intubated and placed in the left lateral decubitus position. A small roll is placed under baby's shoulders and left flank to enhance the right intercostal spaces. A 12-14 French catheter is then placed through the baby's mouth and into the upper esophageal pouch, and the table is tilted slightly to the left in reverse Trendelenburg. The surgeon stands on the left side of the table with the camera operator to the surgeon's left. The scrub nurse is usually opposite the surgeon at the level of the camera operator. The monitor is situated opposite the surgeon for optimal viewing. An explanation of the complexity of the surgical procedure is detailed below.

The first cannula is usually positioned at approximately the eight intercostal space in the posterior axillary line. This 4-5 mm port is inserted using a cut-down technique, and a cannula with a blunt trocar is advanced into the thoracic cavity. This cannula is used for the telescope and camera. A 45° or 70°, 4-5 mm telescope is then introduced through the cannula and the thoracic cavity is visualized. The optimal location of the two working ports can be determined. 3-mm cannulas are introduced at the 4^{th} and 5th or 4^{th} and 6^{th} intercostal spaces in the mid-to posterior axillary lines as working ports. If needed, a fourth cannula can be positioned posteriorly and inferiorly around the 10^{th} or 11^{th} intercostal spaces through which another instrument can be introduced for additional lung retraction.

The azygos vein is seen as is usually the proximal esophageal pouch with the silicone catheter in it, if it is not high in the thoracic cavity. As the TEF has been identified preoperatively at bronchoscopy, the surgeon has a good idea of where the TEF enters the trachea. The azygos vein is kept intact if possible. If not, it is divided with cautery. Once the fistula is identified, the pleura overlying the fistula is incised and the fistula is gently mobilized.

Once the TEF has been identified, the next step is to identify the proximal esophageal pouch to gain a better understanding of the amount of proximal pouch mobilization that will be needed in preparation for the esophageal anastomosis as opposed to proceeding with fistula ligation at this time. If the two esophageal segments are close to one another, little dissection of the proximal and distal esophageal segments will be needed. However, if the segment is widely separated it may be necessary to dissect the proximal pouch high into the thoracic inlet to gain esophageal length for a

tension free anastomosis. Once the proximal esophagus has been mobilized and is ready for anastomosis, the distal fistula is then ligated and divides. A nonlocking metal clip is the most common way. Once the fistula is divided, the esophageal anastomosis is performed in a similar fashion as with the open operation. After completing the anastomosis, attention is turned towards trying to separate the esophageal suture line from the fistula closure on the trachea. The anesthesia is the terminated and the baby is transported back to the intensive care unit.

The thoracoscopic approach is transpleural and requires a longer operative time, however there is better visualization and a much lower risk of systemic infection than with an open operation. The open approach is extra pleural in most instances. Performing an anastomosis high in the chest may be easier with thoracoscopy, assuming there is no significant tension on the anastomosis, but this can be quite difficult at thoracotomy. In the case of anesthesia, is extremely important with thoracoscopy and is relatively standard with thoracotomy. Other advantages of the thoracoscopic approach over the open approach is the reduction/absence of musculoskeletal morbidity following the thoracoscopic approach. (2)

However, thoracoscopy is very challenging technical operation. Not all surgeons can perform a thoracoscopic EA/TEF repair, and experience is required. Due to the very low level of pathological incidences in live births of EA, it is very difficult, and sometimes practically impossible for surgeons to acquire a working expertise. They must therefore rely on their general surgical skill.

A large benefit of performing EA repair using minimally-invasive techniques is avoiding a posterolateral thoracotomy in a neonate. This has been shown to be associated with a high degree of scoliosis and shoulder girdle weakness later in development. Another is the improved cosmetic result. The thoracoscopic approach is the superior visualization of the anatomy and especially the fistula. Because the fistula is visualized perpendicular to its insertion to the membranous trachea, the exact site for ligation can be identified easily, minimizing the residual pouch attached to the trachea (113).

2.7 Breast Reconstructive Surgery

Cancer is a worldwide health problem, accounting for an estimated 9.6 million deaths in 2018. The most common cancers are: Lung (2.09 million) Breast (2.09 million), Colorectal (1.80 million), prostate (1.28 million), skin cancer (1.04 million), stomach (1.03 million). The most common causes of cancer death are:1st- lung cancer with 1.76 million deaths, and 5th - breast cancer with 627,000 deaths (114). In Mexico, the story is not different. Cancer has remained the second or third leading cause of death. In 2000, cancer was responsible for 12.7% of deaths; in 2013, cancer accounted for 12.8%, and the proportion was higher for women. 45.4% of all cancer deaths occurred in the working-age population (15 -64 years) with higher mortality rate in northern Mexico (115). Coahuila reported 18 cases per 100,000 women, Mexico City 17 per 100,000 and Nuevo León 14 per 100,000, The lowest rates are in the southern states, such as Chiapas (1.15 per 100,000) and Quintana Roo (1.45 per 100,000). It is possible that these poorer southern states are also under-reporting due to lack of adequate epidemiology resources or high percentages of rural cases that are never reported (116) (117)

It is estimated that the extent of cancer in Mexico by 2020 will increase to 79 per 100,000 habitants. At the same time, is estimated that people living with cancer in Mexico will increase annually by 109,500 from 518,891 in 2014 to 1,262,861 in 2020. The proportion of all-cause mortality represented by cancer (13%) is still low in Mexico, compares with developed nations like the United States (23%), United Kingdom (29%) and Germany (28%). This analysis is based on available data sources in Mexico, alerting the Mexican health care system of cancer control (118).

The increase in the incidence of cancer in Mexico forced the government to reorganize the health system. Until 2003, Mexicans who were not covered by social security or without private insurance were not entitled to any benefits or health care plans and faced a high risk of catastrophic expenditure. In 2001 to 2006, the *Programa Nacional de Salud* (National Health Program) established the *Seguro Popular de Salud* (Popular Health Insurance), which aimed to extend health care coverage to the entire Mexican population (119). Because of its rising incidence in Mexico, breast cancer was included in the fund for the protection against catastrophic expenses (FPGC) covered diseases list in 2007 (120).

In Mexico, mammographic equipment is scarce, as are trained personnel to adequately address screening needs. In 2000, there were 63 mammography machines in public health centers; those amounts increased to 413 machines by 2006. According to WHO in 2010, there were 314 mammography machines in the public sector of Mexico and 366 in the private sector with a density per population of 37 per 1,000,000 women aged 40 years or older, compared for example with 72 per 1,000,000 in Canada (114) (121).

In Mexico, reproductive factors such as age of menarche and menopause, parity and age at first full-term pregnancy are associated with risk of breast cancer and an increase in risk with high-caloric and high-carbohydrate diets. 7-20% of Mexican patients have strong family history of breast cancer. A small exploratory analysis noted 9% of BRCA1and BRCA2 mutations in patients aged 35 years and younger at diagnosis of early-onset breast cancer. It was reported that in Mexico City 90% of breast cancers were diagnosed through a self-detected breast lump, and therefore often detected in advanced stages.

There are different treatment modalities for breast cancer, such as surgery, radiotherapy, chemotherapy, HER2-directed therapy, and endocrine therapy. The focus of this project is in support of the processes required for the surgery as treatment modality. The covered interventions by the Seguro Popular Public Insurance System included mastectomy, breast conserving surgery, sentinel lymph node dissection, resection of metastatic sites and Oophorectomy. However, breast-conserving surgery is the less-common treatment modality. In a statistical review, at Seguro Popular Public Insurance, 3,654 surgical treatments were performed, which 83.2% consisted in mastectomy and just 16.8% were related with breast reconstructive surgery (122). The *Seguro Popular* covers breast-cancer diagnosis and treatment through a network of 42 affiliate hospitals. In Mexico 62 public institutions have oncology services; one of these institutions is the National Institute for Cancer (INCAN), two are federal hospitals, and 39 are state cancer centers. At 2010 986 oncologists were practicing in Mexico: 59% were oncologist surgeons, 23% medical oncologists, 14% pediatric oncologists and 4% gynecological oncologists, most of them practicing in big cities (123).

In Mexico, the estimation of the average cost per year per patient in a social security institution with data from 2006, was $6,734 USD. However, data published in 2010 in Mexico, indicate that in the public health system, the treatment of breast cancer accounted for 21.2% of the total expenditure allocated by the (FPGC), which in turn represented 1.98% of the total public expenditure on health in the country (118).

Breast cancer surgery is any surgery that aims to maintain quality of life and an acceptable breast appearance whilst at the same time being uncompromising on oncological effectiveness. However, the primary goal is always the oncological effectiveness, leaving the acceptable breast appearance as a secondary outcome. Breast reconstructive surgery also known as breast-conserving surgery intends to mitigate the negative impact of the surgery.

Many techniques of breast cancer reconstructive surgery have been developed, but they focus on three techniques: 1) the use of breast reduction techniques, initially to remove cancers that were located in areas of the breast that could be removed as part of a standard reduction technique but later to include the use of modified techniques to allow resection of any part of the breast; 2) the use of volume replacement techniques, initially using variations on LD flaps but later local perforator-based flaps; and 3) the use of various techniques to allow *en bloc* closure of breast defects, from simple patterns of skin reduction to modifications of cosmetic mastopexies (124) (125).

The main focused in a breast cancer surgery is the collaboration between oncological, plastic and microsurgical skills. Understanding and applying the range of mastectomy techniques available and how they best apply to different oncological and reconstruction options will give the best potential outcomes. Even the traditional mastectomy needs to be performed with thought and planning. The use of contralateral breast reduction with unilateral simple mastectomy in extremely ptotic or large-breasted patients has nothing to do with reconstruction but everything to do with an oncoplastic approach and quality of life.

Poor cosmetic outcome after local excision is best predicted by the percentage of breast tissue being removed and the location of the breast cancer although many factors contribute. Excisions over 5-15% are generally associated with unsatisfactory outcomes if oncoplastic surgery is not used. The main breast reconstructive requirement here would be thoughtful incision planning, an understanding how breast deformity occurs in order to avoid it as well as careful issue handling. Any oncological cavity within the breast will collapse and pull both parenchyma and skin towards the cavity. Any skin excision or incision will contract and create distortion. Central, medial cavities have relatively less laxity and volume, so they create more deformity (126).

After mastectomy, breast reconstruction includes surgery with either saline or silicone implants, autologous tissue reconstruction procedures that use a woman's own tissue transferred from elsewhere on her body to recreate the breast mound. Breast reconstruction is widely assumed to

provide psychological benefits to women, such as increasing quality of life and alleviating the posttraumatic psychological sequelae of breast cancer surgery. New legislation has to be leading to provide reconstructive surgery and other post-mastectomy benefits, due to many if not most insurance company or health maintenance organizations not providing this procedure. Healthcare providers have as a high priority to eliminate health care disparities like differences in access or availability of facilities and services.

Health-related quality of life encompasses physical, psychological, and social domains of health, which are influenced by and individuals' experiences, beliefs, expectations and perceptions. Economic, social, and cultural contexts influence view on what constitutes health, and health-related quality of life. However, feminist scholars have critiqued the normalization of breast reconstruction as a necessary or essential to a woman's psychological recovery (127).

Breast measurements are an important fact in the planning of both reconstructive and cosmetic breast surgery procedures. Breast volume should be measured in breast cancer because the tumor in the breast volume ratios is significative with respect to breast-conserving surgery. Also a volumetric analysis of the breast is necessary for selecting the approach to be used in all types of breast surgery, such as reduction, augmentation, reconstructive and oncoplastic, in order to obtain symmetry of both breasts and to evaluate the cosmetic results more objectively (128). Assessing the breast volume for comparison with the contralateral side would provide a valuable information about the difference in volume, suitable implant size and flap design. However, a method of volumetric analysis has not been identified in the literature yet. Computed Tomographic Angiographs (CTA) and mammographs are considered the imaging choice in perforator flap surgery for the selection of donor site, perforators and flap design. However, due to the advance in technology as 3D surface scanning and 3D printing haptic biomodels, provides a superior mode for visualizing the spatial relationship between anatomical structures and the dimension to preoperative planning. The knowledge of accurate breast volume can enable the estimation of the optimal size of implant or a flap in order to achieve a symmetrical satisfactory outcome (129).

There are measurements of volume methods that are classified in volume, Shape and surface area, depend ending of the measure.

Three-Dimensional Scanner Volume Measurement consists in the construction of the 3D Model. Usually there are two types of devices. Laser scanning machine, in which a beam that is projected onto the breast is reflected and captured by a scanner that can determine the orientation of the

incoming lights. As the distance between the light source and the target and the angle of the light source and target are known, the distance between the target are known, the distance between the target point to the scanner can be calculated based on the principle of triangulation. After millions of points on the breast have been calculated in this way, a 3D model of the breast surface can be constructed. The stereo camera method consists in the perception from two slightly different angles and is used to construct a 3D image like the way the human visual system works. The stereo camera system is therefore composed of several synchronized cameras placed at different angles. Images taken by such a camera system are then used to construct a 3D model. In the case of the use MRI scanning, after the MRI images are obtained, researchers manually define the breast in each scanned layer; the volume of the layer is the calculated as V=A, and the volume of all the layers is summed to obtain the breast volume. Mastectomy Specimen Water displacement, the mastectomy specimen is immersed in a beaker filled with water and the volume is determined by calculation the amount of water displaced, using Archimedes' principle. This method is a reference to validate the accuracy of other measurement methods. (128). Another method applying Archimedes' principle, is Breast in situ water Displacement, the patients are placed in a prone position and the breast is immersed in water in a container. The most used method is Grossman-Roudner Measuring Device, this method consists in a circular piece of plastic, the device forms a cone around the breast and the volume is reads from a graduated scale on the overlapping edges (130), however The linear measurement is well used to determine the breast volume. This method consists in measuring the linear distance between anatomical landmarks on the patient's body and then use a formula to calculate the breast volume. There are two formulas that can be used, based on the calculation of the geometry volume of a cone proposed by Brown and Qiao et al. Equation 2 (131) (132). The second formula is based on the polynomial regression of a large data sample such as Breast V and the formula was proposed by Sigurdson and Kirkland (133).

$$Breast\ volume = (\pi/3)(MP^2)(Mr + Lr + Ir - MP)$$

Equation 2 Qiao et al. Breast volume equation

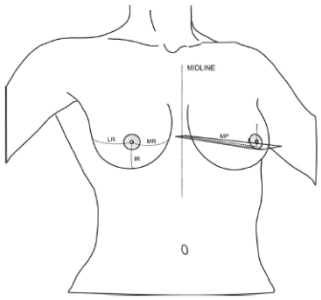

Figure 24 Anatomic Linear measurement (128)

Although the method of mammography is considered determinant for early diagnosis, the process is uncomfortable. In this method, the length and width of mammogram as well as the compression thickness is obtained. The breast is then considered as a cone or a half- elliptic cylinder for volume calculation (3).

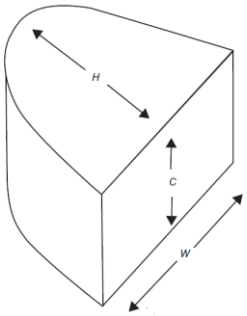

Figure 25 Mammographic breast volume measurement method (128)

3D model reconstruction and MRI have relatively high reproducibility and accuracy, but with a higher cost and are time consuming. Linear Measurements and mathematical models have relatively high reproducibility but are less accurate and cheaper (16). Volumetric analysis using reverse engineering methods like 3D scanning and photogrammetry are cheaper compare to conventional medical image modalities, like MRI, providing useful information for the breast reconstructive surgeons.

Chapter 3 Methodology

There should be no boundaries to human endeavor. We are all different. However bad life may seem, there is always something you can do, and succeed at. While there's life, there is hope.
— ***Steven Hawking*** (134)

3.1 3D Haptic Biomodels for Maxillofacial Surgery

3.1.1 Image acquisition

Data for generating 3D haptic biomodels were acquired from hospital radiology departments by the CBCT image modality in DICOM format. The permission for the use and handling of medical images was obtained from the maxillofacial surgeons in each case. See Appendix 8.2 Ethical considerations and privacy aspects for more details

3.1.2 Medical Image processing

The CBCT images were processed using 3D slicer, an open-software piece of extensible software that specializes in visualization and computation of medical images (www.slicer.org). CBCT images in DICOM format were imported in advanced mode DICOMScalar Volume Plugin, MultiVolumeImporterPlugin, DICOMSlicerDataBundlePLugin A new label map was created using Threshold Effect. The best value that isolated the bone from the rest of the scan was selected in a range of 500-3700 (can be increased in case of noisy result).

The tool *save island* was used to remove disconnected pixels with the same label. This is a way to clean up the results of a thresholding process and separate a single connected structure from other structures.

The module *Model maker* was used to create a 3D surface from the ROI. *Model maker* parameters:

Table 5 Model maker parameters

Start label	**-1**
End label	-1
Smooth	10
Filter type	Sinc
Decimate	0.25

Finally the 3D surface was exported as an STL file for editing.

3.1.3 Mesh optimization

3D model edition was performed using the free software Autodesk Meshmixer (Autodesk, San Rafael, CA, USA) and MeshLab (http://meshlab.sourceforge.net). MeshLab allows the manipulation of the 3D triangular mesh, to remove artefacts and isolate specific sections of the model.

The mesh optimizations consisted in removing duplicated, unreferenced vertices, and filling holes. Filter was Laplacian Smooth (surface preserve) parameters

Table 6 Laplacian Smooth parameter

Max normal deviation	0.5
Iterations	0.3

Filter Simplification: Quadric based Edge Collapse Decimation

Table 7 Filter simplification parameters

Target number of faces	Default
Percentage reduction	0.2
Quality threshold	0.3
Preserve boundary of the mesh	yes
Boundary Preserving Weight	Default
Preserve Topology	yes
Optima position of simplified vertices	yes
Post simplification cleaning	yes

Meshmixer was used for a more detailed smooth sculpt and a final mesh analysis. Orientation and overhangs analysis were applied. Once these operations have done, the mesh was exported as an .STL file (ASCII).

3.1.4 Gcode and 3D printing

The open source slicing software Ultimaker CURA 3.6 (Ultimaker, Geldermaslen,Netherlands) was used to generate the Gcode for printing using RODO 3D R1 & ROBO R2 (ROBO 3D, San Diego, CA, USA) with 1.75mm polylactic acid (PLA) filament (color plus, white shark). After the printing of the 3D haptic biomodel, the final step was post processing, in which the support was removed, and final details were finished with a Dremel tool.

Table 8 Value of parameters using Ultimaker CURA for 3D printing haptic biomodels

Parameter	**Value**
Layer Height	0.3mm
Wall thickness	0.8-1.2 mm
Top/bottom thickness	1.2 mm
Infill density	10%
Extruder Temperature	206
Build Temperature	60
Print Speed	50 mm/s
Outer Wall Speed / internal wall Speed	25mm/s / 50mm/s
Support density	10%
Support Overhang angle	45
Build Plate Adhesion Type	Brim

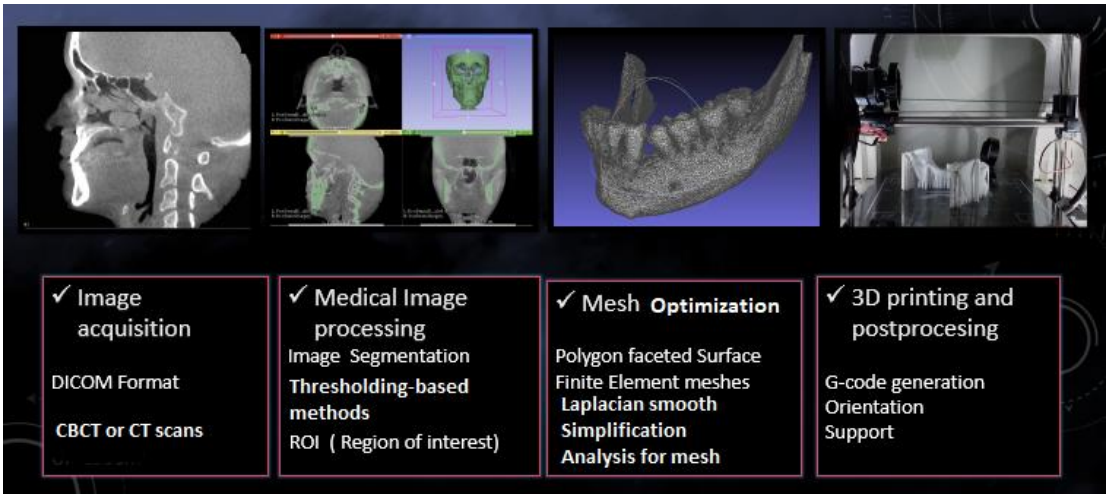

Figure 26 Diagram of workflow for 3D printing haptic biomodels for maxillofacial surgery

3.2 Surgical Training Model for Pediatric Surgery

3.2.1 Image Acquisition

CAT scan image data were obtained from “Hospital del Niño Poblano” (Puebla Children’s Hospital), a public hospital in Puebla, Mexico. Medical images were not obtained from a patient with EA/TEF. Exposing a newborn to a CT scan is contraindicated due to the relatively high level of X-ray exposure. CT scans are not considered as a diagnostic method for EA/ TEF congenital pathology.The exposure of CT scan X-ray in a newborn infant can lead to the development of ionizing radiation-induced abnormalities that can be an unacceptable health risk. MRI scans can be complex to perform due the constant movement of the baby, generating artifacts difficult to avoid. Many, if not most pediatric cases require sedation, a highly contraindicated intervention for a child already in such a delicate medical state (135).

CAT scan images were obtained from the data base of radiology department from a 1-year old girl. Physicians considered a CTA due the contrast and the observation of trachea and esophagus. The surgeons then offered feedback on the scaling of the model to achieve neonatal characteristics from the provided medical imaging.

Table 9 Specification from DICOM format CAT

Slice thickness	**1.25mm**
Images series slices	248
Spacing Between Slices	3.75
Pixel Spacing	0.242188, 0.242188
Rows & columns	512 * 512
Data Collection Diameter	250 mm

3D scanning of newborns was performed using the Structure sensor (Occipital) to correlate the measurement of newborns of different ages and design the surgical training model with the required aspect.

3.2.2 Medical Image Processing

CTA scan data was imported in DICOM format into the open source 3DSlicer software. The organs segmentation consisted of heart, aorta, pulmonary vein, pulmonary artery, superior cava vein lungs, trachea, esophagus, ribs, and soft tissue from thorax.

The segmentation of the anatomical structures was performed using semi-automatic methods, such as *ThresholdEffect* and *FastMarchingEffect*. *FastMarching* is a statistics-based region growing 3D segmentation algorithm. The function *LevelTracingEffect* was used to define the seed voxels, and *march* function to initiate the region growing. Manual segmentation was applied for further details using *PaintEffect* and *LevelTracingEffect* and *EraseLabel*.

Multiple label maps were created, one for each anatomical structure. After defining the individual anatomical structures, the *merge all* function was used to put all he volumes back into the merge volume.

Table 10 Segmentation algorithm for ROI

Left Lung	***FastMarching***
Right Lung	*FastMarching*
Trachea	*FastMarching*
Esophagus	*Fast Marching*
Aorta	*FastMarching*
Left ventricle of heart	*FastMarching*
Right ventricle of heart	*FastMarching*
Superior cava vein	*FastMarching*
Pulmonary vein	*Fast Marching*
Pulmonary artery	*FastMarching*
Bone Thorax	*ThresholdEffect*
Soft skin	*GreyScaleModel Maker*

The Model maker *module was used to create a 3D surface from the ROIs and finally exported into STL format*

Table 11 Model Maker parameters

Start label	**-1**
End label	-1
Smooth	10
Filter type	Sinc
Decimate	0.25

3.2.3 Mesh Optimization and Model design

Because the model being create is a designed model meant to approximate patient characteristics obtained from one or two low-dose reference X-rays, and not a patient-specific tomography due to neonatal tomography limitations, the standard neonatal model must have the pathology designed into it based on these references. A Type-C Anastomosis (Figure 23 Types and frequency of esophageal malformations) was designed using Meshmixer software. The specifications were provided by physicians and the literature, with the final model being approved by the physicians as representative of what they could see in the reference X-ray.

The *Select Tool* was used in brush mode, *unwrap brush* allowing back faces.

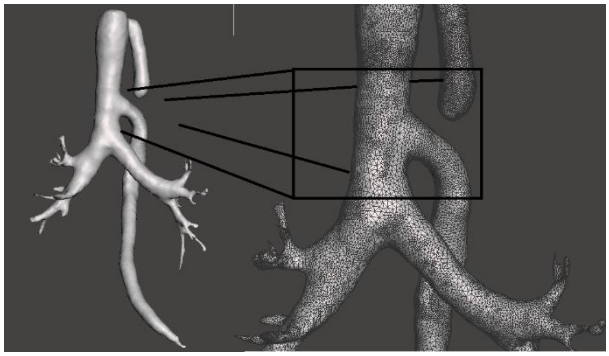

1. *Edit* function and *Discard* were used to erase parts of the mesh of the esophagus and create the Proximal portion and distal portion
2. *Soft transform* was used to create the Tracheoesophageal fistula TEF, between the trachea and the distal portion of the esophagus
3. *Sculpt* function was used to design and create the 3D model realistic
4. *Smooth* brushes with no refinement was applied.

Netfabb Autodesk software was used for further repair of the file.

1. Invert normals were corrected in automatic repair and manually.
2. Holes were corrected in automatic repair and manually.
3. Remeshing local surface mesh

Meshmixer was used to analyze the orientation/rotation of the 3D model for 3D printing considering:

1. Strength: minimize the number of weak points
2. Support Volume: minimize the build Volume
3. Support Area: minimize the surface area of the model that will require support

Mesh mixer was used to analyze the overhangs and generate supports considering the parameters in Table 12:

Table 12 Generated supports parameters

Angle Thresh	25	**Post diameter**	2mm
Contact Tol	0	**optimization**	50
Y offset	2mm	**Solid min offset**	.02
Max angle	45	**Tip Height**	1 mm
density	20	**Base Height**	2mm
Layer Height	0.1mm	**Strut density**	0
Tip diameter	0.6 mm	**Post side**	16
Base diameter	4mm	**Allow top connections**	yes

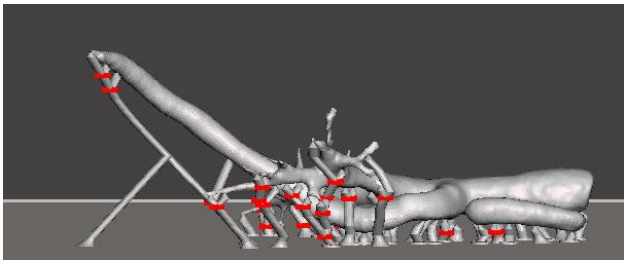

Figure 27 EA model with support designed by Meshmixer.

Meshmixer is a versatile software dedicated to model design with 3D-printing extensions. The analysis tools for orientation and overhangs enable making the 3D printing process more effective by simulating orientations and supports overhangs, making it easier to remove and save material.

Lungs were fixed using Netfabb Autodesk software for further repair of the file.

1. Invert normals were corrected in automatic repair and manually.
2. Holes were corrected in automatic repair and manually.
3. Errors in mesh were corrected

Meshmixer sculpt brushes were used for further smoothing of the mesh.

1. No refinement was applied

Injection molds for right lung and left lung was design using NetFabb Autodesk

1. Primitives were imported
2. Boolean operations subtraction was applied to create the mold for both lungs

Aorta was fixed using Netfabb Autodesk software for further repair of the file.

1. Invert normals were corrected in automatic repair and manually.
2. Close holes were corrected in automatic repair and manually.
3. Errors in mesh were corrected
4. Remeshing was applied in local surface

Meshmixer sculp brushes were used for further smoothing of the mesh.

1. No refinement was applied

Sacrificable mold injection was design using meshmixer

1. Offset tool was applied
    a. Distance 1.2
    b. Accuracy 50
    c. Regularity 25
    d. Soft transition 0

Heart ventricles, pulmonary artery, pulmonary vein, superior cava vein were fixed using Netfabb Autodesk for further repairs in the files

1. Invert normals were corrected in automatic repair and manually.
2. Holes were corrected in automatic repair and manually.
3. Errors in mesh were corrected
4. Boolean operations were applied and remeshing was performed
5. Each 3D object was imported as one individual object, and then exported as one object

Meshmixer sculp brushes were used for further smoothing of the mesh.

1. No refinement was applied

Sacrificial mold injection was designed using Meshmixer

1. Offset tool was applied
    a. Distance 1.2
    b. Accuracy 50
    c. Regularity 25
    d. Soft transition 0

Sacrificial molds for heart and aorta were done using the *offset* tool instead of *hollow*. The *offset* tool is like *extrude* but is a more complex operation. The distance parameter was set at 1.2mm to ensure printability. Using the *offset* instead of *hollow* tool avoided the loss of material and the modification of the models. InFigure 28 the design and parameter variables for *offset* are found. (*Toggle visibility* shows the spatial appreciation)

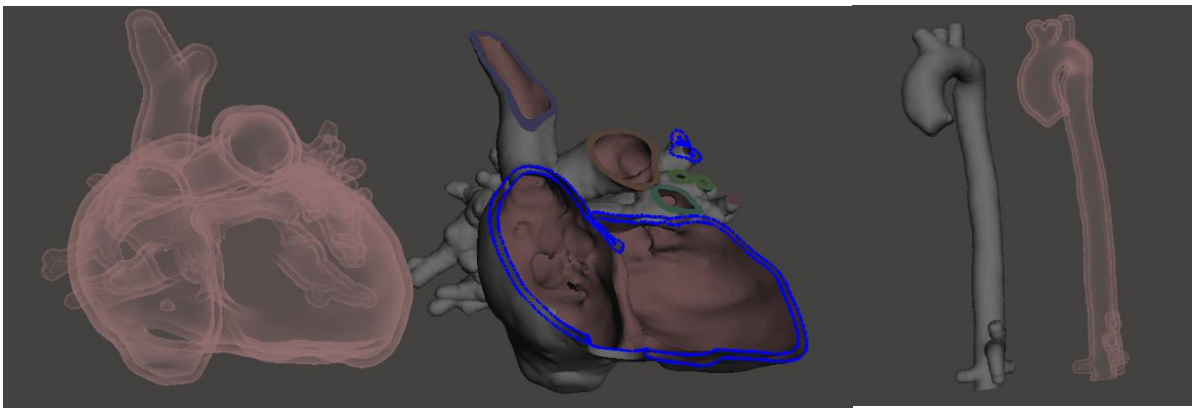

Figure 28 Toggle visibility and plane cut representation of the heart and aorta. The offset parameter 1.2mm is shown

Thorax bone and skin were fixed using Netfabb Autodesk

1. Invert normals were corrected in automatic repair and manually.
2. Holes were corrected in automatic repair and manually.
3. Errors in mesh were corrected

Meshmixer sculp brushes were used for further smoothing of the mesh.

1. No refinement was applied

Thorax bone analysis was implemented using Meshmixer to analysis the orientation/rotation of the 3D model for 3D printing, considering:

1. Strength: minimize the number of weak points
2. Support Volume: minimize the build Volume
3. Support Area: minimize the surface area of the model that will require support

Meshmixer was used to analysis the overhangs and generate supports considering the next parameters:

Table 13 Parameters for generating supports

Angle Thresh	25	**Post diameter**	2mm
Contact Tol	0	**optimization**	50
Y offset	2mm	**Solid min offset**	.02
Max angle	45	**Tip Height**	1 mm
density	20	**Base Height**	2mm
Layer Height	0.3mm	**Strut density**	10
Tip diameter	0.6 mm	**Post side**	16
Base diameter	4mm	**Allow top connections**	yes

Every organ was fixed and optimized. The dimensional analysis was performed comparing the dimensions of the esophagus, trachea, 3D scans and the experience of the consulting surgeons. A typical neonatal trachea has a length of 4 cm from the larynx to the carina. The typical neonatal esophagus has a length of 7-14 cm.

3.2.4 3D Printing and Silicone Casting

Anastomosis EA /TEF, Trachea & esophagus 3D model STL were converted to GCode using opens source Ultimaker CURA 3.6.0. The filament used was PVA (soluble in water) filament by ROBO R1.

Table 14 Gcode parameters using Ultimaker CURA 3.6.0

Layer height	.1mm	**Flow rate**	100%-120%
Walls thickness	.8 mm	**Retraction**	no
B/T thickness	1.2	**Extruder Temp**	193
Infill density	0%	**Build platform Temp**	50
Print speed	20 mm/s	**Supports**	no

After 3D printing of the Anastomosis EA/TEF sacrificial mold, this mold was subjected to postprocessing stage to remove supports and filament material to maximize the smoothness of the silicone surface. The sacrificial mold was sanded using Dremel with extreme caution to not alter the surface itself but merely remove support points.

A silicone elastomer (Smooth On Co.) was manually mixed with catalyst at 1:1 ppv. This elastomer has a hardness of 00-10 Shore A, to ensure the mimicking of the tactile sensation of the tissue. The sacrificial mold was coated with the elastomer and the cured for 6 hours at room temperature.

The PVA sacrificial mold was dissolved in water for 10 hours, creating a complex hollow anastomosis EA/TEF made consisting entirely of elastomer.

Sacrificial molds of heart and aorta were printed with PVA using open source Ultimaker CURA 3.6.0.

Table 15 Gcode parameters for PVA using Ultimaker Cura 3.6.0

Layer height	0.3mm	**Flow rate**	100%-120%
Walls thickness	1.2 mm	**Retraction**	no
B/T thickness	1.2mm	**Extruder Temp**	193
Infill density	0%	**Build platform Temp**	50
Print speed	20 mm/s	**Supports**	no

The postprocesing consisted in removing supports and extra filament material.

Elastomer was manually mixed with catalyst at 1:1 ppv and has a hardness of 00-30 Shore A, to ensure the mimicking of the tactile sensation of the tissue. The sacrificial mold was cast with elastomer and the cured for 6 hours at room temperature. Consequently, the sacrificial molds were dissolved in water for 4 hours

Inverse molds for lungs were printed using the open source Ultimaker CURA 3.6.0. The filament was PLA 1.75 mm and the 3D printer MM1 (MakerMex).

Table 16 Gcode parameters for PLA using Ultimaker Cura 3.6.0

Layer height	0.3mm	**Flow rate**	100%
Walls thickness	1.2 mm	**Retraction**	yes
B/T thickness	1.2mm	**Extruder Temp**	206
Infill density	10%	**Build platform Temp**	60
Print speed	50 mm/s	**Supports**	Yes

The molds were subjected to a postprocessing stage to maximize the smoothness of the silicone surface. PLA Lung Molds parts were sanded with Dremel and then coated with XCT-3D, a resin, and left cure for 3h. The model was additional protected with parafilm and plasticine in the connecting areas between parts, to prevent elastomer leakage.

Elastomer was manually mixed with catalyst at 1:1 ppv and has a hardness of 00-10 Shore A. elastomer was poured inside the inverse molds. The elastomer was cured for 4 hours and the removed carefully.

The Thorax bone was divided in 2 parts and printed using open source Ultimaker CURA 3.6.0. The filament was PLA soft 1.75 mm and the 3D printer ROBO R1.

Table 17 Gcode parameters for PLA Soft using Ultimaker Cura 3.6.0

Layer height	.3mm	**Flow rate**	120%
Walls thickness	.8 mm	**Retraction**	NO
B/T thickness	.8mm	**Extruder Temp**	203
Infill density	10%	**Build platform Temp**	50
Print speed	20 mm/s	**Supports**	no

The 3D printed Thorax bone was summited to a post processing that consisted of removing the supports and extra filament. Final sanding was performed using Dremel with extra caution.

Thorax soft tissue skin.

The Thorax soft tissue was divided in two parts and printed using open source ROBO for CURA. The filament was PLA color plus (skin color) 1.75 mm and the 3D printer ROBO R2.

Table 18 Gcode parameters for PLA using CURA for ROBO

Layer height	.3mm	**Flow rate**	100%
Walls thickness	.8 mm	**Retraction**	yes
B/T thickness	.8mm	**Extruder Temp**	205
Infill density	5%	**Build platform Temp**	60
Print speed	60 mm/s	**Supports**	no

The 3D printed Thorax bone was summited to a post processing that consisted of sanding using Dremel with extreme caution and then coating with the XCT-3D, resin, and left to cure for 3 h.

Different layers of elastomers were applied to mimic, skin, fat and muscle tissue. The hardnesses were 2A, 000-35 and 00-30 A Shore, respectively. The different elastomers layers were cured for a total time of 7 hours at room temperature and then removed carefully as one layer.

Multipart structures were glued together according to the assembly simulation using an elastomer adhesive. Artistic representation was done by painting and adding layers without interfere on the original simulation assembly.

3.3 3D Volumetric Analysis for Breast Reconstructive Surgery

3.3.1 Image acquisition

Each patient was given an informed consent form (forms can be found in 8.2 Ethical considerations and privacy aspects) with personally identifiable information blocked or removed for patient privacy). Each patient was under standard medical care and had medical approval to participate in this study.

Each participant was given a study code for identification of the patient file. Age and diagnosis were the only patient-specific data recorded to maintain =patient privacy. The 3D scanning session avoided the face, just the torso was included in the frame mark, to avoid privacy violations. After the 3D scanning session, the 3D model and photos were showed to the patient to verify again the privacy of and identity protection, and the patient gave final consent to use the acquired scans and photographs for this research.

Participants were scanned in standing position with feet slightly apart and arms abducted. The 3D scanner used was Structure sensor (Occipital) and a Nikon 3300 camera was used for the stereo method.

3D scanning structure sensor:

1. The participant remained in a fixed position during the scanning procedure while proceeding to capture the scan at 160-180 degrees.
2. The distances between the participant and the scanning was at least 1 m.
3. Anthropomorphic landmarks were measured and used as a reference marker

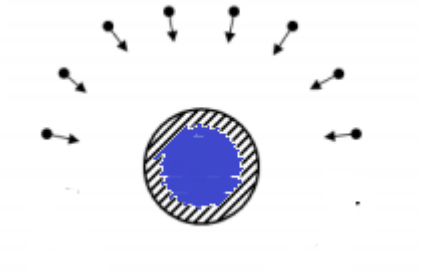

Figure 29 Correct position to take the scan and photos

Stereo Camera

1. The participant remained in a fixed position during the scanning procedure while photos were taken at 180-degree intervals.
2. Several pictures were taken with low ISO and manual mode, with good light (daylight) and avoiding flash.
3. Anthropomorphic landmarks were measure and used as reference markers.
4. Each photo used the frame size: the participant should take up the maximum areas

3.3.2 Data Extraction and Manipulation

The Structure sensor generated the 3D mesh in real time while the scanning was performed.

1. 3D mesh was imported in .obj format into MeshLab
2. The breast boundary was defined, and the breast area of 3D model was selected
3. A chest wall was simulated by the software to generate a close object in which the volume is calculable

Stereo Camera

The set of photos taken in the scanning session were imported (40-80 photos) into Agisoft Photoscan

1. Align photos

   Accuracy -> high

Pair Selection -> Disable

Key Point Limit-> 40000

Tie Point Limit-> 4000

2. Dense Point Cloud Parameters

   Quality -> low

   Depth filtering-> aggressive

3. Model reconstruction parameters

   Surface type-> arbitrary

   Source data -> Dense

   Quality-> high

   Face count-> 180,000

4. 3D mesh was imported in .obj format into MeshLab
5. The breast boundary was defined, and the breast area of 3D model was selected
6. A chest wall was simulated by the software to generate a close object in which the volume is calculable.

3.3.2 Validation

Linear shape measurements were taken directly on a patient's chest using tape. These anthropometric metrics were calculated by the physician who calculated the volume of the breast using conventional methods. To avoid bias the neither of the value of the volumetric analysis were revealed until the validation portion of the procedure.

Chapter 4. Results and Discussion

"Women's" war has its own colors, its own smells, its own lighting, and its own range of feelings. Its own words. There are no heroes and incredible feats, there are simply people who are busy doing inhumanly human things."

-Svetlana Alexievich (136)

4.1 3D Haptic Biomodels for Presurgical Planning in Maxillofacial Surgery

3D printing in surgical planning such as in maxillofacial surgery is creating a great impact. In these procedures all the capacities of image processing and the use of CAD systems can be brought to bear for improved patient care and patient-doctor communication.

The types and numbers of maxillofacial surgical haptic biomodels printed were:

N= 16 maxillary

N= 15 mandibles

N=6 facial skull (splanchnocranium)

3D slicer is an open source program with python platform for medical image informatics, image processing and 3D visualization. It has over two decades of development supported from the National Institutes of Health and worldwide developer community. That is the main reason why 3D slicer was selected as the medical image processing software in this project (137). The creation of extensions and the continuous feedback of the community make this program a versatile and experimental software that can adjust to the needs of the developers and users.

In the cases of maxillofacial surgery, CBCT DICOM images were used, due the lower exposer of X-Ray and low cost, compared with conventional CT scans, was described in 2.3 Medical Imaging The main disadvantage of this medical application is its sensibility to artefacts and noise. Artefacts and noise complicate the accuracy of image segmentation. Although some researchers consider HU and grey scale values of CBCT comparable with low difference between them (91), we found minimal

difference in the threshold values level applied to generate the label map desire with the lowest artifact and noise.

3D printing medical applications has a great impact in dentistry and maxillofacial surgery, especially in preoperative planning of implant surgery and cutting guides for orthognathic surgery. The clinical conditions in this type of surgery requires an analysis of the bone condition for the implant success. Clinical conditions reported that affect the bone quality are smoking habits, intravenous medications interactive with bone metabolism and radiotherapy (101).

The bone quality consists of the amount of bone height and the width of the alveolar crest at an edentulous site. Aging and clinical conditions develop atrophy of the bone, it means amount of loss of normal alveolar bone secondary to the loss of a tooth, other aspects that define the bone quality are the bone physiology, the degree of mineralization, the morphology and type of trabecular pattern. If the bone quality is poor, the implant will not be a success due to the lack of support and retention (90).

The use of radiography to evaluate the bone quality is widely used, however the surgical planning has moved to study the 3D nature of the anatomical structure using CBCT. There is not a universally-agreed classification of the range of grey scale to evaluate the bone quality in the maxilla and mandibula. In preoperative planning, surgeons need to ensure the size and the correct placement of implants, this can be done by using CAD dental software. Although the use of 3D haptic biomodels provide a better spatial-visualization of the 3D anatomy, bone height and width can be measured using surgical calipers and the distances to anatomical structure such mandibular canal and sinuses are better appreciated. Even when the bone is not enough for support the dental implant, a bone grafting can be evaluated. Bone grafting is an extraction of bone section from other area of the body, like maxillary. The 3D haptic biomodels enables to evaluate the region of bone extraction inclusive intraoperatively (108).

*Figure 30 CBCT images for maxillofacial surgical planning, artifact visible. A) Axial plane B) Coronal plane C) sagittal plane. Image spacing 0.32mm, umbral threshold range (1410 - 3505), image dimensions 468 * 468*

Image acquisition and processing are important steps to planification and for the accuracy of 3D haptic model. In CBCT the grey values are not consider HU like in CT modality due the inaccuracies in grey values of CBCT that depends of the variability in the axial plane (beam hardening, FOV, domain artefacts), variability of axial slices and high image noise stochastic effects Figure 30. The correct filter to reduce the noise of medical images is a decisive part of the process. however, not all filters are suitable for each case. The values of thresholds are determined for each case

To determine the most accurate level of threshold segmentation value, a volume analysis was done previously by obtaining the histogram of the scalar volume of the CBCT study as can be seen in Figure 31. The threshold of the histogram was fixed to reduce domain artefacts.

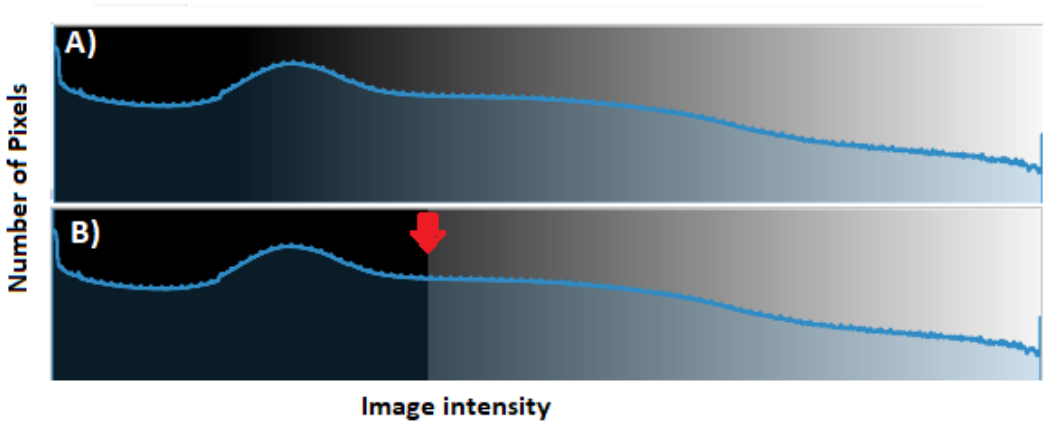

Figure 31 Threshold values from CBCT images (figure 28), A) histogram values (1410 - 3526) B) Red arrow indicate the set of 500-3526 on histogram

The analysis of the histogram permits a better visualization of the scalar volume values. In CBCT images segmentation, threshold-based methods are the principal for fast and simple selectin of

ROIs. In this case study of the mandible and the facial skull, the inferior nasal concha (2), lacrimal bones, Maxilla, Nasal bones, Palatine bones, Vomer and zygomatic bones are necessary for symmetrical analysis (Figure 32).

Figure 32 CBCT images. Defining threshold values with 500-3526. All voxels with values <500 where set to 0, as background.

3D slicer permits the generation of a multiple labels map for specific anatomic structures. Figure 33 shows an axial series of a CBCT image using different label maps. In this case, the cervical slices are not necessary and can be excluded for the final 3D surface rendering to generate the 3D model. The same can be done, separating maxilla and mandibula, to generate two 3D models or for volumetric analysis.

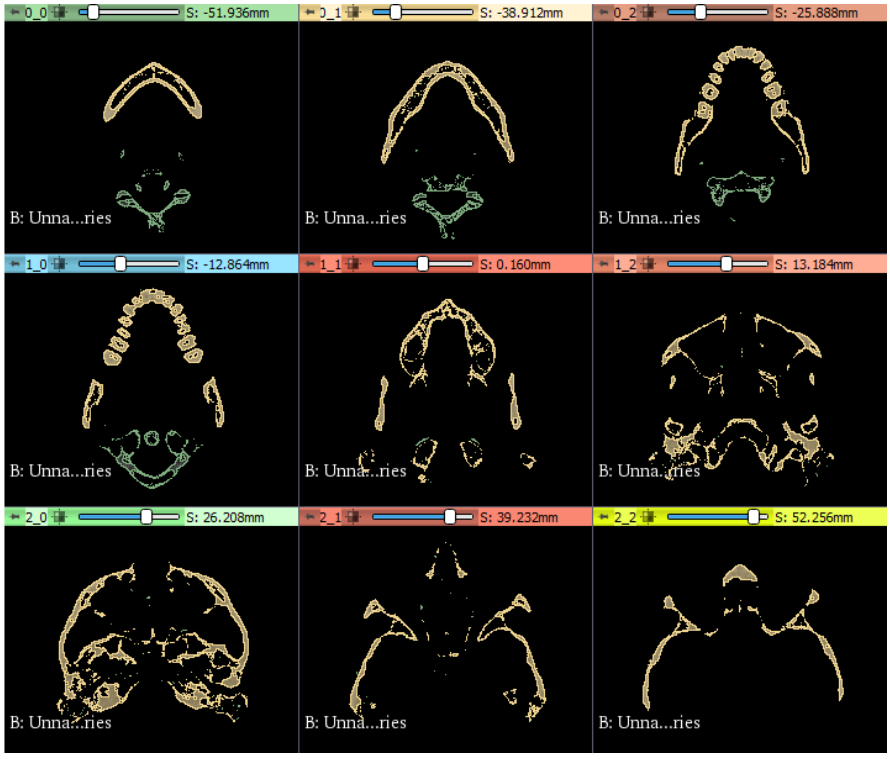

Figure 33 CBCT images in three planes. Threshold level effect: green represents the anatomical structure represented in scalar volume of the cervical that are discarded for the 3D haptic model; yellow segmentation label is considering the ROI.

One of the major problems in CBCT image processing for bone segmentation are the “holes”. Holes are local minima in the grayscale topography that are not connected to boundaries of the images. For example, in CBCT images trabecular areas of the bone show up as lower HU values than the outer bone surface making it difficult to segment the bone region using simple thresholds. To solve this problem morphological filters can be applied to the volume series. *GrayscaleFillholeImageFilter* filled the bone regions to accomplish the needed bone segmentation. The filter *smooth* over local minima was applied without affecting the values of local maxima(Figure 34 and Figure 35).

Figure 34 CBCT image Comparing filter Gray scale Fill Hole Filter in Axial plane

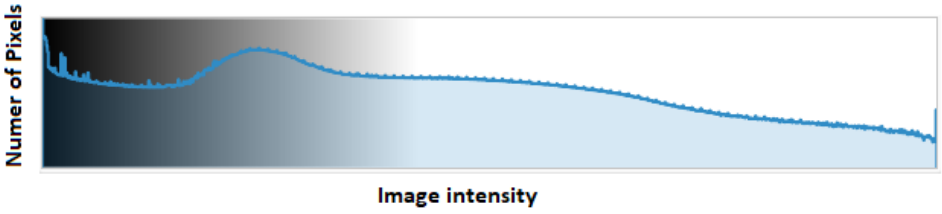

Figure 35 Histogram representation for CBCT scalar volume with filter gray scale fill hole.

The presence of gray level non-uniformities in CBCT contributes to artifact generation, the most common artifact in dentistry is the ring artifact related with the scanner, and metal distortion. CBCT has a low contrast resolution and is affected by noise due to this, making difficult to differentiate low-density tissues and affecting the segmentations

The *GaussianBlurImageFilter* was applied to the CBCT image series as is observed in Figure 36. The applications of denoising filters can minimize de disturbance of the gray level in CBCT to blur the image reducing the noise. The degree of smoothing is determined by the standard deviation of the

Gaussian. The effect is to remove high spatial frequency components from an image but a cost of undefined the border edges. This is because the Gaussian filter is a low-pass filter that removes high frequency components (edges) as we can compare the histogram of unprocessed CBCT series and the histogram with the filter applied. Th e difference in the histograms is the denoise step which removes the disturbance of the histogram

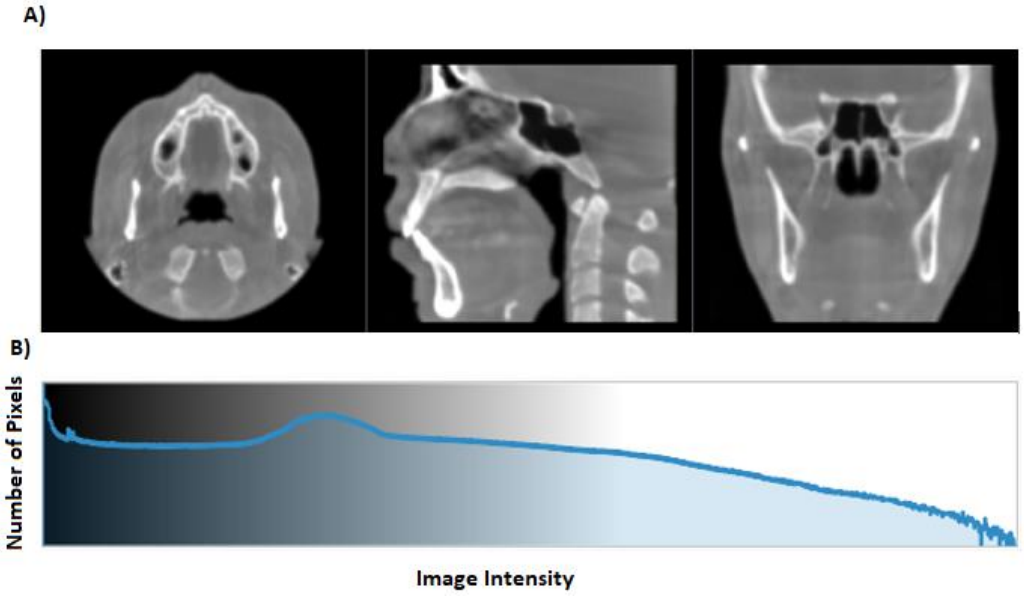

Figure 36 A) CBCT images in three planes, axial sagittal, coronal with denoising filter Gaussian using Sigma 1. B) the histogram is obtained after application of GaussianBlurImageFilter

The use of the adequate filter for image processing determine de accuracy of the 3D structure. A comparison of different labels maps was done to determine the best filter and thresholding. Table 19 indicates background, Skull label map with histogram thresholding of 550-3526. Skull G indicates the label map using Gaussian filter, Skull ffG indicates the label map with morphology filter grayscalefillholeimage and gaussian blurring, Skull ff indicates the label map for grayscalefillholeimage only. All the label maps were obtaining using Thresholding effect with a value of > 550. Count indicates the number of pixels in the label volume that have the value indicated. Volume mm3 is the product of the pixel spacings (volume*pixel) times the count in cubic millimeters, volume cc is the volume per pixel times the count in cubic centimeters Figure 37. The mean and standard deviation (StdDev) are elements of descriptive statistics on the gray scale pixel values at the locations that correspond to the label value threshold.

Table 19 Label Statitistics

Type	Count	Volume mm³	Volume (cc)	Mean	StdDev
background	84944442	2783456.82	2783.45	-409.714893	531.410464
Skull	4647781	152298.343	152.29	994.380484	357.422473
Skull G	4263110	139693.455	139.69	946.467064	440.700755
Skull ffG	4198326	137570.615	137.57	955.006444	436.274299
Skull ff	4672322	153102.501	153.1	991.096996	359.44153

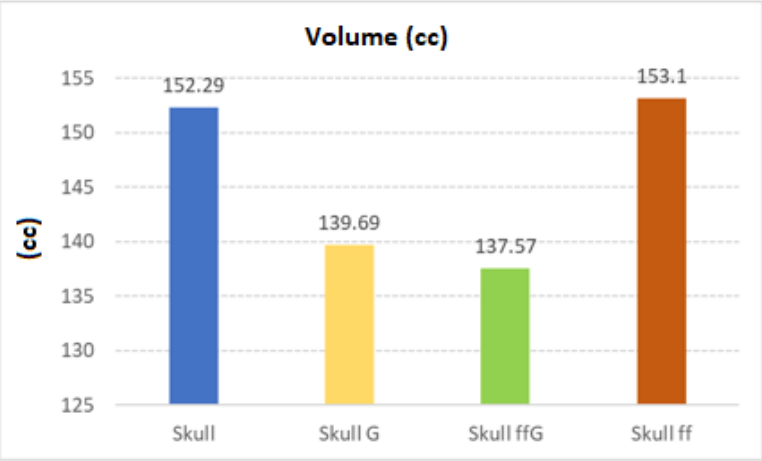

Figure 37 Graph comparing the label maps for volume (cc). The label map Skull ff has a volume of 153.1 cc. due to the extrapolation across the hole of the gray level values adjacent to a hole. In this case the skull facial was filled. However, the label map Skull ffG has a volume of 137.57 cc. due to the lossof border definition and disturbance of the histogram. These values have a STd.Error of 4.09 and Std Dev of 8.19

According with the comparison volume analysis of the label maps using different filters but with the same thresholding effect value (500), applying the Gaussian filter for denoising the images, results in a loss of volume that affects the 3D surface rendering. Although the 3D model resulting from segmentation using the Gaussian filter is considerably "cleaner" compared to the 3D model without processing, it cannot be implemented for pre-surgical planning in maxillofacial surgery due to the lack of bone tissue, which may result in poor evaluation of bone quality. This observation is demonstrated in Figure 38 and Figure 39 , shows less bone tissue in the maxilla, palatine, nasal bones and vomer bones.

The variability and the disturbance in grayscale values of CBCT complicate the image segmentation. However, thresholding level segmentation is adequate for CBCT images. The adequate value of thresholding selects the pixels that have a particular value or are within a specified range. To analyze the histogram of every study can give a better approximation of the correct value for that study. In

this case setting the threshold to 500, indicate that levels below 500 are set to black. For this process, anatomical structures (in this case, skull facial bones) are separate from the background.

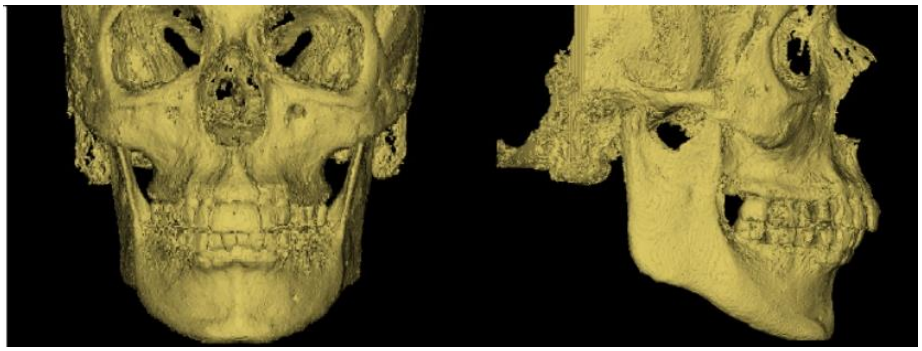

Figure 38 3D surface rendering from label map segmentation of unprocessed volume scalar

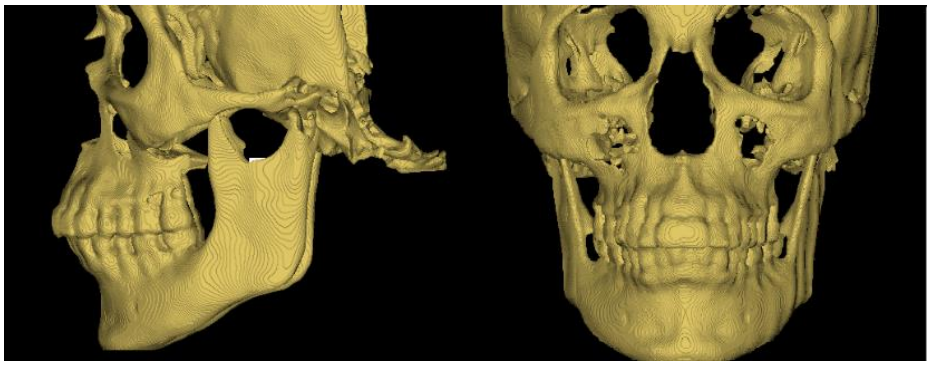

Figure 39 3D surface rendering from label map segmentation of gaussian filter volume scalar

Around 37 image segmentations were performed and the thresholding levels were between 450-600 for 3,500 for CBCT images. However more precise analyses need to be performed to ensure a closer range and normalization for CBCT images.

3D mesh optimization was performed using open source MeshLab software and Meshmixer. The first step was unifying vertices by MeshLab. The mean tessellation of skull facial bones is 2,500,000 triangular faces, while for a mandible the mean is 500,000 triangles or facets. Manipulating the skull facial bones in CAD system with 2,500,000 triangular faces represents a high computational cost. Using simplifying filters with a factor of 0.3 reduced the triangular faces without significant loss of accuracy of the original mesh. Laplacian smooth filtering was done for 3 iterations, more than that

causes unacceptable losses in the original mesh. Automatic Repair is done by Netfabb Autodesk software (Educational License) to ensure holes are closed rendering a watertight model, remeshing the mesh and avoiding manifold structures. The metallic artefact can be minimized by manual modification of the mesh. Final smoothing was performed by Meshmixer (Figure 40) represents the final 3D model optimization ready for 3D printing

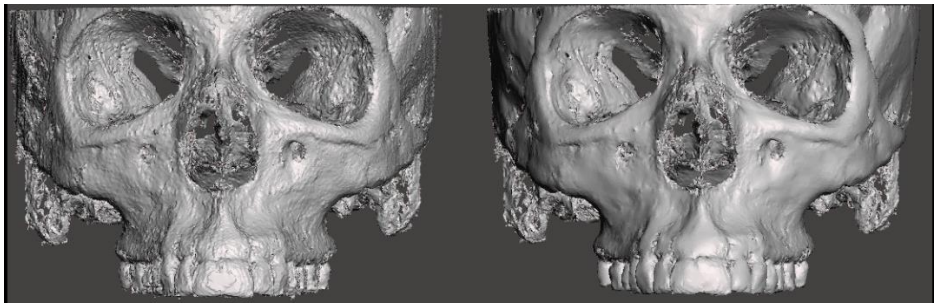

Figure 40 Before (left) and after (right) CAD post-processing. Simplification: quadric edge collapse decimation, preserving topology and boundary of the mesh. Laplacian smoothing, surface-preserving filters specifications were applied by Meshlab and Meshmixer open source software.

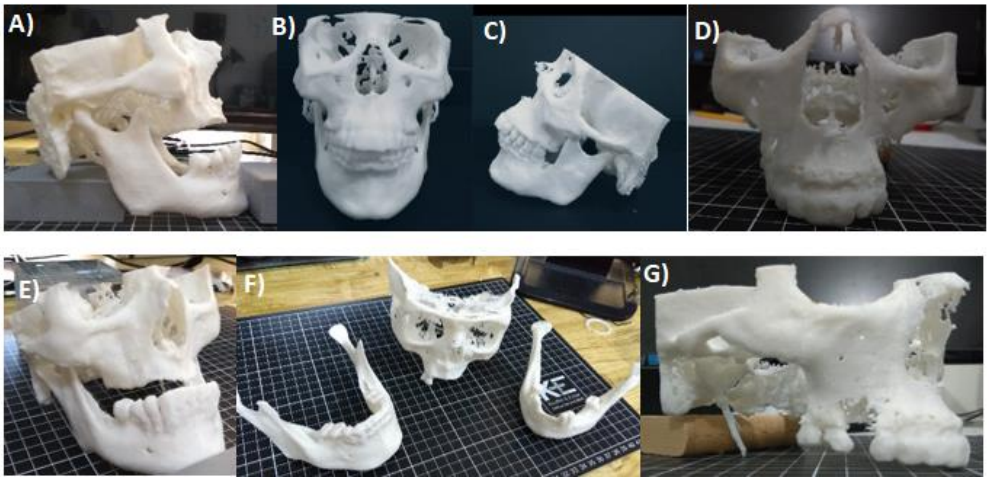

Figure 41 3D Haptic model por presurgical planning in maxillofacial surgery, Severe atrophic maxilla is observed in A,) E) and F), malocclusion is observed in B) and D and Eagle syndrome and porous region of bone, not suitable for Bone grafting are shown in G).

One aspect that concerns the 3D printing process is the accuracy of the 3D haptic model. During the conversion of formats from the acquisition of medical images, information is lost or distorted. In the same way, the physical properties of the material used during the additive manufacturing process can interfere with the precision of the design. To counteract this, it is essential to perform a dimensional analysis between the FDM and the STL models, finding the correction factors that can avoid the lack of precision in the model. It is also a way to analyze the accuracy of the printer.

Table 20 Description of mandible measurements

Variable Number	Measurement	Definition
V1	Bicondylar breadth	Direct distance between the most lateral points on the two condyles
V2	Bicoronoid breadth	Direct distance between the points at the tip of the two coronoid processes
V3L	Minimums ramus breadth Left	Minimum breadth of the mandibular ramus measured perpendicular to the height of the ramus
V3R	Minimums ramus breadth Left	Minimum breadth of the mandibular ramus measured perpendicular to the height of the ramus
V4aL	Mandibular notch breadth Left	Direct distance from the condyloid superior pint to the coronion
V4bR	Mandibular notch breadth Right	Direct distance from the condyloid superior pint to the coronion
V5L	Breadth of mandibular body Left	Maximum breadth measured in the region of the mental foramen perpendicular to the long axis of the mandibular body
V5R	Breadth of mandibular body Right	Maximum breadth measured in the region of the mental foramen perpendicular to the long axis of the mandibular body
CD	Condyles Right	Distance of the breadth
CI	Condyles Left	Distances of the breadth

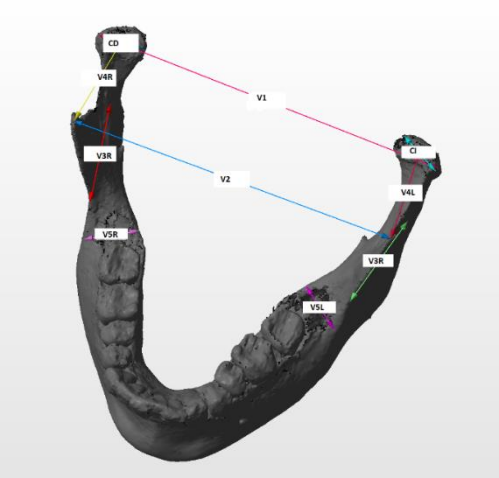

CBCT images from 6 patients were processed to obtain the 3D models in STL format for posterior printing at 0.3mm layer height. The same parameter for slicing the models were used in the six STL models. The slicer program was Ultimaker CURA 3.6.0.

Ten anatomical linear measurements were selected shown in Figure 42 and the description is in Table 20 Description of mandible measurements. The STL models' linear measurements were measured with three different CAD tools, Meshlab, NetFabb Autodesk and 3Dslicer. The haptic biomodels were measured with digital electronic caliper.

Dimensional error was obtained by calculating the deltas between CAD model measurement and FDM haptic model, represented mathematically **¡Error! No se encuentra el origen de la referencia.**:

$$Dimensional\ Error\ \Delta = CAD - FDM$$

Equation 3 Dimensional Error

The dimensional error was obtained for each variable (linear measurement). The Correction factor was defined as the ratio of STL model measurement to FDM haptic model, expressed mathematically in Equation 4 .

$$CF = \frac{CADmeasurement}{FDM\ measurement}$$

Equation 4 CF

CF values were calculated for each measurement and the mean of these values was the overall Correction Factor for the FDM machine employed. For the machine in this work, (Robo 3D and MM1) This value was 0.97. This value can be used to scale the STL.

Table 21 Description of the dimensional error, CF and mean for each variable

	CAD	Std.Dev	Std.err	FDM	Std.Dev	Std.Error	Dimensional error	CF
V1	112.74	6.56	1.54	112.89	7.312	2.98	0.148	.99
V2	93.79	2.95	0.69	92.39	3.33	1.36	-1.39	1.01
V3L	29.43	2.62	.61	31.66	2.41	.98	2.22	.92
V3R	28.85	2.80	.66	30.23	1.65	0.67	1.38	.95
V4L	28.99	7.7	1.8	32.31	5.34	2.18	3.32	.89
V4R	30.88	4.19	.98	29.75	4.78	1.95	-1.13	1.03
V5L	15	1.69	.39	15	1.65	.67	-0.038	.99
V5R	14.99	1.57	.37	14.48	1.96	.80	-0.51	1.03
CD	17.81	3.44	.81	17.29	3.12	1.27	-0.51	1.02
CI	15.46	1.43	.33	17.03	2.29	.93	1.56	.90

Statistical analysis was perform using Sigma Plot Software. Values of descriptive statistic were obtained, for a detailed statistical analysis see appendix 8.1. STATISTICS. Non-parametric test for 3D Haptic Biomodels for Presurgical Planning in Maxillofacial Surgery. The sample size of the variables is not suitable for parametric test. However, a normality test non-parametric Kolmogorov-Smirnov was done for each variable using a $P > 0.05$. The variables CAD CR CAD CL CADV4L , CADV3L and CADV1 failed the test. A test that fails indicates that the data varies significantly from the pattern expected if the Data was drawn from population with normal distribution. T-student Kolmogorov-Smirnov was performed to compare the differences between the values measurement by CAD and FDM for each variable using a $P< 0.05$. In case the Normality Test Kolmogorov-Smirnov failed. Mann Whitney Tests were done to compare the groups using a $P < 0.05$. No statistically-significant differences were found in the sample represented by CAD measurements and FDM measurements. It suggests that the measurements don't vary statistically and present the accuracy need for presurgical planning. However, more data needs to be analyzed to minimize the error. A larger sample size would be needed to study the size of the effect in every variable combination test.

The benefit of the implementation of additive manufacturing in the medical sector is not only because of the precision of the models but also because of the reduction in costs of carrying out preoperative surgical planning adequate. In the case of maxillofacial surgery, physicians have expressed a considerable reduction of surgical time (18). In the literature, the most frequent uses

for 3D haptic biomodels is the anatomical models in maxillofacial surgery and for preoperative planning, follow by surgical guides, implants, and molds. Most of the cases reviewed in the literature affirm a reduction of 2+ hours per surgical intervention. Another advantage is a greater understanding between physician and patients. If a patient had a much better understanding about their condition and subsequent surgical treatment this improves consent and helps reduce patient abandonment of the prescribed treatment path (103).

Table 22. Description of the cost-timing-benefits to implement 3D printing technology and 3D haptic biomodels FDM printed

Mandible						
	CAD Time (min)	Layer Height (mm)	Print Time (min)	Post-Process (min)	Printed material mass (g)	Prod. Cost (MXN)
	180	0.3	285	20	54	$ 43.20
Skull (Facial)						
	180	0.3	866	90	155	$124.00
Max Sup					g	cost prod
	70	0.3	172	20	28	$ 22.40

Table 22 expresses the overall time, material, and estimated final costs to produce various haptic models. CAD time represents the time in minutes to process images, optimize the mesh, and to obtain a 3D model ready for 3D printing. The slicing parameters can modify the printing time, making it faster or slower. The layer height is considering the quality parameter for 3D printing. Most FDM technology has the capacity to print 0.1mm layer height resulting in the highest quality for FDM printers. However, for most haptic biomodels this level of layer precision does not represent a significative difference in model quality and utility, but due to the nature of the FDM process results in a nearly linear increase the time of printing. For example, increasing the model resolution by halving the layer height doubles the number of layers required to achieve the same model. Each layer prints roughly in the same amount of time (with cooling times providing one of the higher degrees of variability in that linearity). Thus, having a workable model at 0.2 mm layer height instead of 0.1 can cut the production time nearly in half. If the model is acceptable, there is no economic or

medical reason to push for unnecessary increases in time. If a very fine resolution (0.01 to 0.1 mm, roughly) is required, such as for printing splints or surgical guides for drillubg, FDM technology is not adequate, and technologies that can work at higher resolutions without time downsides (such as finishing whole layers at a time instead of single points at a time as with FDM) such as SLA technology are recommended.

Table 23 Description of cost-time benefits in reducing the cost of operation time by implement 3D haptic biomodels FDM

Surgeries	TIME (Hours)			OR Cost ($ 1500 / h).
	Mean	RANK	Reduction	Savings(MXN)
Long (Resection / reconstruction)	9	8 to 14	2	$3,000
short	5	4 to 6	1.5	$2,250

For the cost-time analysis, dollar value estimations were taken from the real MXN cost and estimated at the published exchange rates in April 1, 2019 of $19.19 MXN/ USD. The mean time to obtain a final mandible 3D haptic biomodel was 8.1 hours with a cost production of ~$43.00 MXN. (~2.24 USD). Comparing this cost with conventional methods like stereolithography or plaster models, the commercial costs start at $2,000 MXN (~104 USD), and the acquisition time is 3-5 working days. In the case of facial skull, the overall time was 18.9 hours, however the time can be reduced with a double-extrusion printer, and the implementation of a water-soluble filament (PVA) to remove the supports. The production cost was $124 MXN (~6.24 USD). The commercial cost can vary from $4,100 –$9,000 MXN (~208- 469.12 USD) with an acquisition time of 3-5 labor days. Some companies add a further cost for the conversion of DICOM to STL format.

The analysis of the cost that represent the reduction of operating time is represented in Table 23.In maxillofacial surgery there are two types of surgery according to the duration time. Long-term surgery includes reconstruction and resection, the length of these surgeries is in the range of 8-14

hours. The reduction time of 2 hours represents a savings of $3,000.00 MXN (~156 USD) minimum considering that the hospitals have an average initial charge of $3,000.00 MXN (~156 USD) for the first hour and subsequent $1,500.00 MXN (~78.19 USD) of OR costs. The cost of operating time represents 30 to 40% of total hospital expenses. The major advantages are not just financial, the reduction of operating time represents the decreasing the exposure time to general anesthesia, and the possible complications. Shorter surgical times have also been shown to have a significant impact on the recovery period (109).

4.2 Surgical Training Model for Pediatric Surgery

The use of 3D printing in the physical recreation of complex pathology can lead to improved surgical skills for difficult cases such as the repair of EA / TEF. EA is a congenital pathology where the esophagus does not develop correctly, instead the esophagus ends blind-ended rather than connecting to the stomach (2).

There are four primary types of this condition, but the surgical training model is focused in the type C, the most common, with a frequency of 86% of all EA cases. Type C occurs where the lower esophagus connects to the trachea creating a fistula, affecting 1/2500 newborns. There are two approaches for surgery: an invasive thoracotomy, considered “the gold standard”, and a minimally-invasive thoracoscopic surgery. The first thoracoscopic surgery was in 1999, and in 2011 it seems to have finally been considered superior to open surgery (112) (2). However, it has to be performed by experienced surgeon, and the surgical learning curve is slow and is more difficult to teach. This procedure demands the highest degree of minimally invasive surgical skills, in a pathology that occurs so infrequently that it is difficult and maybe even impossible to acquire a working expertise in the problem. The importance of 3D printing models in surgical training like this can be a difference in the learning curve for such technically challenging surgeries. The literature considers a normal learning curve requires 10-20 thoracoscopic EA repairs, while many pediatric surgery centers perform 5-10 EA repair per year (111).

The design and dimensions of the model were made according to the literature (138) (139), and the specifications provided by the head of surgery of the children's hospital in Puebla and its team of residents in pediatrics and laparoscopy. In addition, 3D scans were performed on newborns under the supervision of the surgery chief and resident of the Puebla Children’s hospital and its residents,

to obtain different body measurements according to the procedure. All medical information was obtained in accordance to and subject to the hospital's privacy protections clause and informed consent and date use consent forms. The hospital had general consent forms for all the patients, and non-personally identifiable scans with parental authorization additional to the hospitals permission, and under the supervision of medical staff.

The organs segmentations were performed using 3Dslicer. Multiple labels maps were implemented for trachea, esophagus, lung right, left lung, pulmonary artery, pulmonary vein, superior cava vein, aorta, left ventricle, right ventricle. thorax bone and soft tissue skin thorax (Figure 43). The Fastmarching process was performed, to use a region-growing algorithm for segmentation. Thresholding was used just for bone thorax segmentation. Thorax segmentation was not complete due the level of HU, not considering the cartilage. This part needed to be done manually.

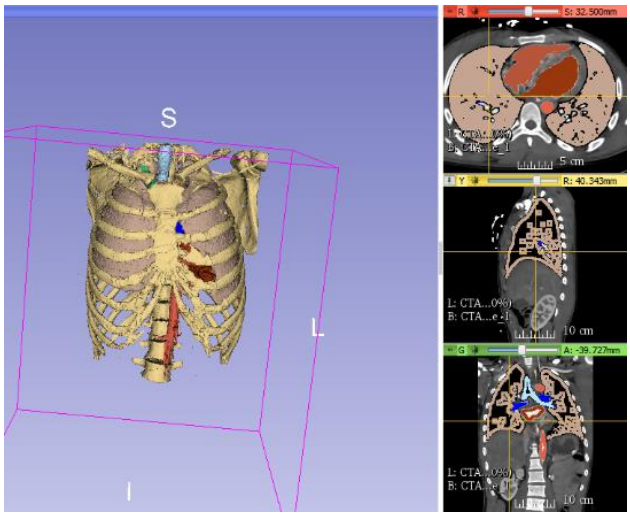

All the segmentations were performed by *merge all*, *label maps* and *build the model* to not affect the position and orientation of the organs (Figure 44). The esophagus is difficult to observe in CTA scans due to its physiology. The segmentation of the esophagus was not complete due the peristalsis of the organ.

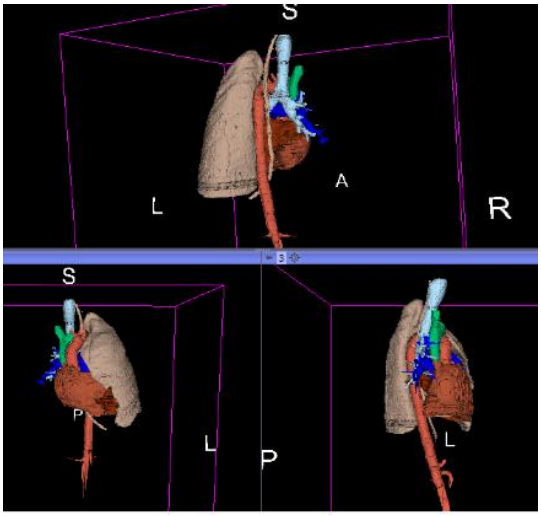

Figure 44 3D slicer Scene for "Merge all" and "build

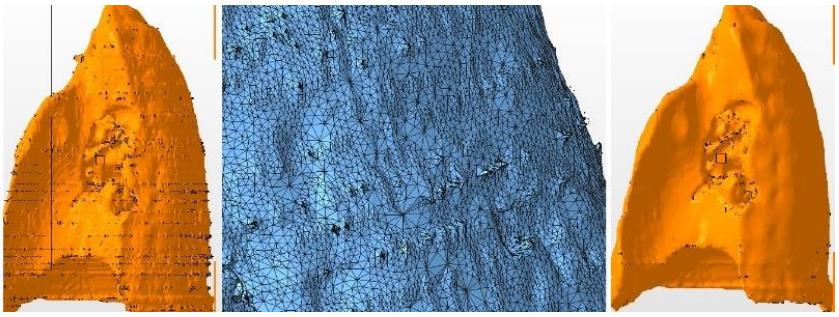

Figure 45 Representation of before and after file repair and mesh optimization by NetFabb

Manual design and remeshing was performed using NetFAbb Autodesk. Degenerated Faces were removed, tiny shells, double triangles and all the holes were closed (Figure 45). Every 3D model organ was fixed with Netfabb Autodesk to produce fixed, watertight shells.

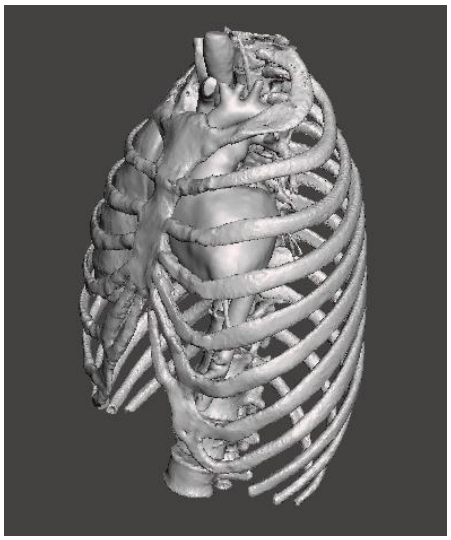

Figure 46 All the anatomical structures were scaled with CF = 0.3849

Finding the correction factor was essential to ensure the dimensional accuracy of the model. The correction factor to achieve the dimensions of a neonate from the 1-year old model was found to be 0.3849. All the anatomical structures were scaled using this factor (Figure 46).

All the anatomical structures were printed on an FDM 3D printer (Robo R1 and MM1) using ABS and PLA, to ensure the correct dimensional measurements and merge operations in the initial prints. ABS was used for its ability to dissolve in acetone and create a smooth surface. By using the "cold vapor" method, the ABS piece smooths slowly and in a non-uniform process. The surgical training model was done by parts, mimicking primary tactile sensation from every organ and tissue. For the lungs, an inverse model was designed using Boolean operations with Netfabb Autodesk and casting the resultant inverse mold with an elastomer with a specific hardness to ensure the tactile sensation. The thorax bone was printed with PLA soft. This was to mimic neonatal bone, as these are flexible soon after birth. For complex and hollow structures, sacrificial molds were designed and printed with PVA, a water-soluble material. However, other materials that have the capacity to dissolve

were tested like HIPS and ABS but the management of acetone and limonene is risky and special ventilations is need. Although the cost of PVA was nearly quadruple that of standard materials, rising as high as MXN$ 1,400.00 per 0.500g, its simple handling and easy dissolving makes its cost viable, besides, it prints easily with parameters for flexible filaments (Figure 47 y Figure 48).

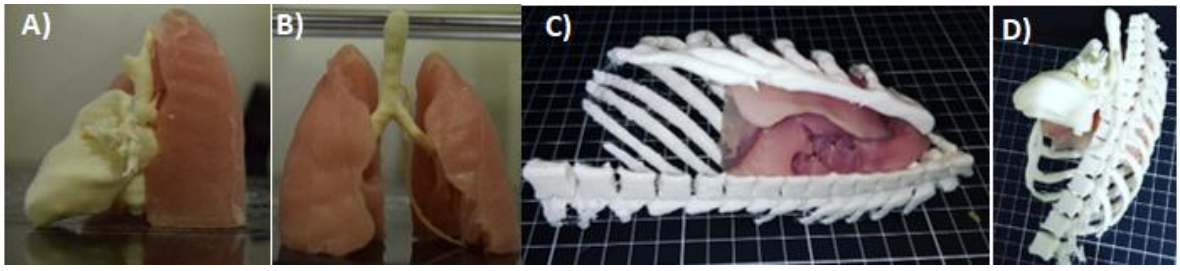

Figure 47 Visual-spatial representation for the anatomical structures to be used in the neonatal model: A) Right lung made of elastomer merged with the ABS heart model B) lungs made using elastomers and EA anastomosis representation. C) PLA soft used to represent the thorax bone with right lung. D) PLA softt , heart ABS, EA anastomosis and lung.

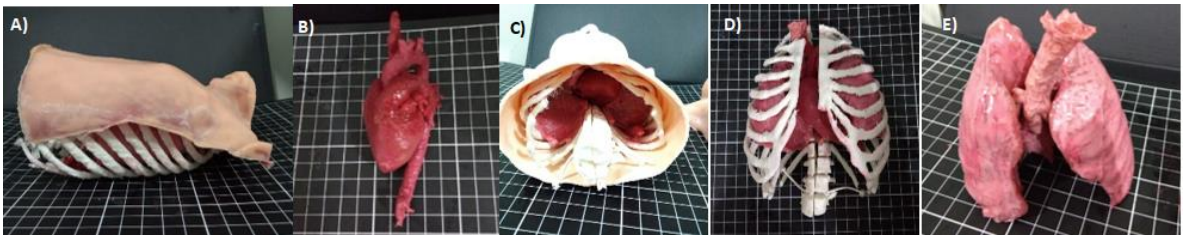

Figure 48 Representation of the anatomical assembly for the surgical training model. A) Skin soft tissue front section, with a realistic representation of multiple layers and stiffnesses enables the surgeon to additionally practice sutures, B) heart and aorta merge C) internal view of the anatomical representation. D)Thorax bone and internal organs representation, E) lungs and anastomosis, hollow structure representing the trachea.

The parts of the model can be replaced without the need to replace the entire model, ensuring cost reduction. The total production time is represented in Figure 49 and Table 24 indicate the time and the cost production for the surgical training model prototype for EA repair.

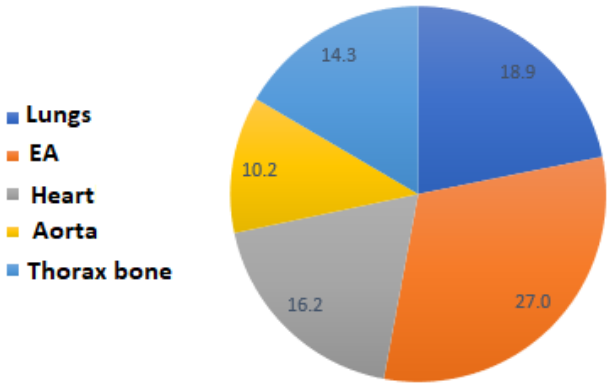

Figure 49 Representation time in Hours to build the surgical training model for EA repair via the minimally invasive approach. The total time is 86.3 hours that represents 3.6 days if performed on a single machine. This process time includes everything from image processing model deign, to the final realistic representation with elastomers

The EA anastomosis anatomic structure required 27 hours to be build, due the precise post-processing using elastomers. Physicians need to practice the sutures in this anastomosis. Mimicking the real tactile sensation, required multiple coats with different hardness elastomers that required various cure periods at room temperature. Also, the period to create the hollow structure is longer due to the limited surface exposure of PVA in water. Thorax bones required large printing time due the parameters required, because PVA is flexible and needs to be printed at a low printing speed, a 20 or 10 mm/s. Aorta, heart and lungs require similar time process due at the casting technique. However, lungs don't require much post processing time because no dissolution material is required. Instead the inverse models just required to be printed one time all the process requires 85.7 hours that equals 3.6 days of production by one person and counting just one 3D printer. The time for CAD processing can be neglected, because, this process is needed just one time to create the molds which can be. The total cost production of the surgical training model was $ 482 MXN. This represents a considerable reduction relative to market for other types of medical simulators. NEONASIM is consider the medical simulator company of recognized excellency. The simulator for a NENAsim carries a cost of $ 22,950.00 USD, that converted to MXN hast a cost of $ 441,787.50 however this commercial surgical training tool has difference attributes, making it suitable for patient management and care but not for training surgery (13). Also, there is not a commercial training model for the approach described in this thesis.

Table 24 Representation of specific process times for surgical training model prototype EA and cost production MXN

Anatomical structure	Processing Time						COST (MXN)		
	CAD	Printing	POST Printing	TOTAL (MIN.)	TOTAL (HR.)	TOTAL (Days)	Material	Elastomers	TOTAL
Lungs	230	634	270	1,134	18.9	0.8	$159	$97	$256
Ea Anastomosis	120	103	1,395	1,618	27.0	1.1	$6	$14	$20
Heart	363	86	525	974	16.2	0.7	$18	$60	$78
AORTA	78	70	465	613	10.2	0.4	$13	$7	$19
Thorax bone	160	700		860	14.3	0.6	$109		$109
TOTAL	951	1,593	2,655	5,199	86.7	3.6	$305	$178	$482

The cost-benefits analysis suggests a savings of $124,112 per person per hospitalization. When compared to Mexico's average salary of XXXXXX/month, this can be a significant difference to a patient's family and caretakers. The major benefits rely in the capacity to shorten the learning curve for thorascopic EA repair. Recalling that the learning curve requires at least 15 procedures, however most hospitals have on the order of five EA procedures each year. The thoracoscopic approach, reduces the operative time and recovery time period, generate more capacity in the hospital to cycle through more procedures. Table 24 describes the cost-benefits for the surgical training model EA repair prototype

Table 24 Cost -benefits representation for the implementation of surgical training model prototype EA repair

Births in Mexico	EA (1/2500)	Pediatric Hospitals	Surgeries in Mexico	Learning Curve	Number of procedures	Time-to-Expertise (years)	Surgical time (horas)	Recovery time (days)	Hospital costs $MXN
Thoracotomy Approach									
2220708	888	32	128	15	4	4	3	21	162,897
Thoracoscopic EA simulator prototype									
2220708	888	32		15	30	6	1.5	5	38,785
Estimated Saving per patient									124,112

4.3 Breast Reconstructive Surgery

The innovation of technologies like 3D printing can contribute significantly in medical procedures that require preoperative planning reduce the risks and outcomes. interventions that affect a great part of the population such as breast cancer can be immediately benefited from these problems.

The problem in preoperative planning in breast reconstruction is a lack of volumetric analysis. Most of the reconstructive surgeons still rely on 2D images and subjective visual assessment for evaluating breast volume which varies depending on the experience and the ability. The application of reverse engineering in this scenario can help to solve this outcome. The use of 3D scans generates a surface rendering that provide additional information about shape and contour. 3D models can be printed and provide extra dimension. The knowledge of breast volume can enable the estimation of the optimal size of the implant or flap in order to achieve asymmetrical result

Construction of the 3D model is obtained by 3D scan or photos. The obtention of the 3d model, the breast boundary is defined, and the breast area of 3D is selected, the boundary can be selected by palpation and marker before the scanner or defined based on the landmark of the 3D model. A chest wall is then simulated by CAD software (Figure 50). A closed object of the breast is obtained, and the volume is calculated. In the unilateral breast reconstruction, the analysis of the discrepancy between the surface are of the two-breast can assist the planning to improve symmetry.

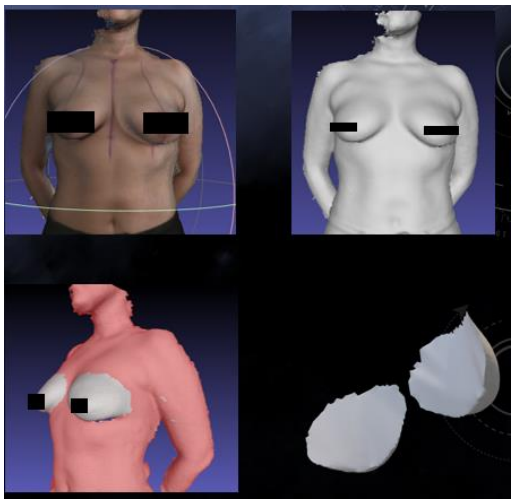

Figure 50 3D model reconstruction using Structure Sensor.

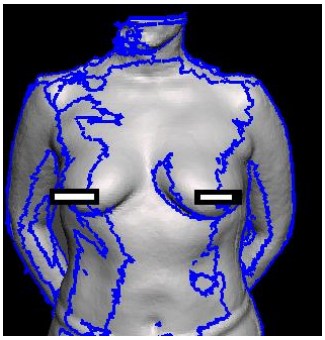

Figure 51 Mesh problems

The 3D Structure sensor was used to generate the 3D model of the participant. The time savings to obtain the 3D model in real time is the major advantage for this method. However, due to the manipulation of the 3D scanner, the 3D model is created with multiple shells, making a complex post processing (Figure 51). The files can be used importing the 3D *.obj model into MeshLab and exported as STL format.

Table 25 shows the values of measurements in cm^3 obtained after volumetric analysis, using Blender (CAD) , Agisoft Photoscan (Ag) and the anthropometric measurements were obtained using Equation 2 and provided by the surgeon. A difference was made between right and left breast due to the loss of data in the point cloud generation using Agisoft Photoscan.

Table 25 volume values in cm^3

	CAD Left	CAD Right	Ag Left	Ag Right	M Left	MRight
1	151.91	143.9	120	134	140	142
2	233.60	382.40	--	350	260	330
3	291.5	320	--	310	300	330
4	414	461	418	--	423	430
5	295	391	293	385	310	367

Because the size of the sample was small, the statistical test to validate the 3D modelling options vs. established methodologies used was a non-parametric test, Kolmogorov-Smirnov. The statistical analysis can be seen in Appendix 8.3 STATISTICS for volumetric analysis for breast reconstructive surgery.

All the groups passed the Normality Test for Kolmogorov-Smirnov, indicating that the data matches the pattern expected if the data was drawn from a population with normal distribution.

The difference in the mean values of the two groups was not great enough to reject the possibility that the difference is due to random sampling variability. There was not statistically significant difference between the group CAD Left Vs AGleft. CADleft Vs MLeft ($P<0.05$)

The difference in the mean values of the two groups is not great enough to reject the possibility that the difference is due to rando sampling variability. There is not statistically significant difference between the group CAD Right Vs AG Right. CADRigh Vs MRight , CADright vs AGRight ($P<0.05$)

Correlation among the three breast volume measurement techniques was done using Pearson Correlation. Pearson correlation tests were done for left breast and right breast, revealed that 3D scanning showed the best agreement with photogrammetry (AG) ; $r= 0.995$, $P < 0.05$, for the right breast and revealed that photogrammetry (AG) has the best agreement with anthropomorphic method ($r=1$ $P < 0.01$)

Chapter 5 Discussion

5.1 3D Haptic Biomodels for Presurgical Planning in Maxillofacial Surgery

The implementation of 3D printing in maxillofacial surgery is constantly extending its applications in variable surgical cases, like production of custom-fit implants that can be used for surgical planning and training. The developing of new materials and high-resolution printing is necessary, however, despite the potential of cost limitations to acquire expensive 3D printing machines, 3D technology is continuing to be drive down in terms of the price of devices and materials. The limitation excluding the cost can be addressed to create suitable materials with desirable mechanical and biological properties that can be printed directly. (140)

The most used materials for maxillofacial and craniofacial surgery are ceramics, metallic oxides, calcium phosphate and glass ceramics. These materials exhibit good compatibility and bioactivity. However, low fracture toughness and ductility makes them not suitable for load-bearing application (141). New materials have been developed for an alternative for metallic and ceramic biomaterials are polymers. Degradable polymers that have been investigated for maxillofacial defect repairs include poly (glycolic acid) (PGA). This material has osteoconductive properties in vivo but does not resist the mechanical strain of normal activity, with a consequent decrease in molecular weight and degradation. Other materials include PLA, and copolymer (PLGA) (142), poly (ε-caprolactone) (PCL) which offer good biocompatibility and mechanical properties (143), and poly (propylene fumarate) (PPF) (144), a composite that can improve the repair of maxillofacial fractures and polyamide/hydroxyapatite, which shows excellent biocompatibility and cell attachment but a limited mechanical stiffness (145).

Despite all these new materials developed, only a few polymers have been used for bone replacement. Polyetheretherketone (PEEK) has emerged as a new trend for bone replacement. PEEK can be manufactured for FDM technology, produced Apium PEEK 450 Natural 1.75mm filament from medical grade PEEK, with excellent chemical resistance and the perfect combination of strength, toughness and stiffness and suitable for sterilization. Despite this new material, PEEK filament can be only printed a high temperature, with print extruder temperatures up to 520° C and print bed temperature up to 160°C (146). There are very few 3D printers that can print at these temperatures. One of them is Apium P220, an industrial FDM 3D printer, manufactured in Germany

that cost between $10,000.00 – 50,000.00 USD (147), (~$192,224.00 - 961,615.00 MXN). Despite the advance of being able to directly print a medical grade material using FDM technology, there is still the limitation of the accessibility of the equipment and the corresponding certifications for medical applications. However, it could take 5 years for this technology to be more accessible. The advantage would be that the process of creating a 3D haptic model for implants would not vary with the current method to create 3D haptic models for surgical planning. Having the potential in reducing the financial burden on the overall healthcare sector, the importance lies in having the human resources, training, and manufacturing equipment and capacity to make it possible. The correction of maxillary and mandibular deformities from dental maloclussion, diseases, injuries can be done by the creation of osteotomy guides as seen in Figure 41.

Maxillofacial surgery is not only limited to mandibular and maxillary reconstructions or implant design. Orbital surgery is a challenging procedure due the complex anatomy. However, the design of a 3D haptic model in this case follows the same procedure presented in section 3.1 3D Haptic Biomodels for Maxillofacial Surgery. A research group in Germany designed a simulation Device for Orbital surgery. They created a 3D-model of the orbit segmenting the bone tissue (hard tissue) and the soft tissue was manufactured using silicone model. However, they employed a compound powder processed by selective laser sintering using PA2200. The soft tissues structures were manufactured as a single use model by distinct silicone mixtures (SLM SOLUTION & SMOOTH-ON) on negative mold models, created by 3D printing. The 3D Simulation Device represented all hard and soft tissue characteristics needed for the appreciation and manipulation of orbital anatomy, inclusive reducing the training expenses (148).

Comparing their process with the one presented in section 3.1 3D Haptic Biomodels for Maxillofacial Surgery and section 3.2 Surgical Training Model for Pediatric Surgery, the difference consists in the material and type of 3D printing technology. SLS technology is considered a professional and industrial AM process. The cost of material PA2200 is around EUR 0,75 (excl. 19% VAT, or ~EUR 0,90 incl. 19% VAT**)** per cm^3 material volume (149)**,** Representing an approximate cost in MXN currency of $ 16,146.00 for 1 Lt (excl. 19% VAT, Type currency $1 Euro – $21.54 MXN at April 2,2019). Despite the reduction in cost that creating a 3D device for simulation and training using 3D technology represents, in Mexico the reality is quite different. Public hospitals in Mexico operate with a low funding, that health sector operate with 6.23% of GDP, compared with USA 17.09% of GDP or Germany 11.29% of GDP (150), and total expenditure on health per capita of $1,122.00 USD,

$9,403.00 USD and $5,182.00 USD, respectively (151). Nevertheless, 3D printing technology is making a difference with respect to conventional methods of manufacturing, especially in the medical sector.

5.2 Surgical Training Model for Pediatric Surgery

3D haptic models for pre-operative planning do not just represent a better visual-spatial appreciation to prevent possible outcomes during the surgical performance, they can also help understand the pathology more precisely and enhance communication between patient and surgeon. A good example for this is the prenatal complex cases, where 3D haptic models contribute to help the parents understand the actual pathology and physicality of the unborn child, providing an essential prenatal tool, facilitating communication between parents and members of the surgical team (152). The workflow to obtain 3D haptic models for a prenatal case, is the same as the implemented in section 3.1 3D Haptic Biomodels for Maxillofacial Surgery, however, in prenatal cases it is much common to acquire the image DICOM form an ultrasound , instead of MRI or CAT. Nevertheless, 3D Slicer has the extensions to process images from ultrasound, being ideal inclusively for prostate pathologies or breast cancer.

Implementation of 3D haptic models prevent the risk in the surgical performance, not only in maxillofacial surgery as we describe in the section on 3D Haptic Biomodels for Presurgical Planning in Maxillofacial Surgery. The advantage from manipulating and create a 3D physical representation of a specific anatomical structure has a distinct advantage in pre-surgical planning. The application of CAD/CAM has spread widely from medical sector, due to the detailed representation of complex anatomical structures and the possibility of manipulating the 3D CAD model for the requirements of the surgeons for pre-operative planning or the ability to design a specific model to represent a congenital malformation that may be difficult to analyze using just medical images. 3D haptic models can be used to create an osteotomy guide to evaluate the exact cut line's planned position in the operating room, and even other applications such the surgical guide for genioplasty, the elaboration of osteotomy guide fitted on the mandibular incisor for genioplasty. Although no images are shown with the cutting guides in the 3D models, the models were used to measure and test the surgical guides, dental implants, cutting guides, angle analysis and bone quality for maxillofacial and orthognathic surgery. One model was even printed on flexible TPU material, which had a print duration of 52 hours, for cutting training purposes.

The methodology proposed in the present work has the versatility to respond to the needs of several medical disciplines, which require an analysis and novel proposals for surgical planning and even solve intraoperative problems. Although an FEA analysis was not proposed, the *.stl model can be used for these analyzes. These FEA analyzes are implemented above all in the design of cranial implants, which would correspond to a future work of this project. Vascular anatomy models such as the aorta, veins, arteries and even the heart are used for fluid analysis and vascular testing. The proposed methodology for the realistic representation used in the training model in the section Surgical Training Model for Pediatric Surgery can be applied to pressure and vascularity tests to simulate cerebral aneurysm.

The facilities and cadavers for surgical training are expensive and some institutions don't have access to the limited resources while in others cadaver training is being minimized or phased out. As mentioned before, a FEA method can be applied to these generated models, such as in the simulation of brain retraction and displacement, for example (153).

The combination of CAD/CAM system, FDM technology, silicone casting and coating techniques contributed to the design and production of an affordable surgical simulator. The pediatric surgical model for EA/TEF repair consists in hollow structures representing EA/TEF anastomosis, using the technique of silicone coating, that can be applied to build silicone arterial replicas to train surgeons on spacing, orientation, clips and sutures (154).

In the case of surgical training models for pediatric surgery, CAD/CAM design, FDM technology and silicon coating and casting techniques were integrated, to maximize the realistic sensation of the anatomical structures using different densities of silicone (SMOOTH-ON). Using these methods, every anatomical structure can be fabricated separately, ensuring the low cost for model replacement. The silicone material ensures the possibility to practice sutures and clips, such as in the cerebral aneurysm simulator. Another important low-cost model for training for a minimally-invasive surgery was in the case of esophageal atresia with tracheoesophageal fistula (EA/TEF) repair. This model was made with household materials such as a piece of wood, corrugate plastic tubes (OVS of different sizes to simulate ribs, intercostal spaces, trachea and spine), and tubular latex balloons to simulate the esophagus and lungs to make the basic model. This device was inserted into thoracic cavity of a rubber dummy simulating a newborn, this entire model has a cost of $ 50 USD (155) (~$ 961.21 MXN). The simulator fabricated in this project has a cost of $ 482.00 MXN, with more realism in the anatomical structures, without requiring an extra dummy that can

represent an extra cost, and the workflow can be modified for different requirements and needs of the surgeons. For example, a surgical team could practice all the types of EA, and different ages of the newborn patient, adding more complexity to the training and preventing outcomes in the surgical procedure.

5.2 Breast Reconstructive Surgery

3D printing and medical image segmentation can be applied to analyze tumor shape and dimensions as well as to represent whole body structures. 3D haptic biomodels of tumors could provide additional information for the radiologist and breast surgeon. A research group in Germany, implemented 3D printing to construct several breast tumor models, using semiautomated delineation for the MRI medical images of the breast cancer (156). The semiautomated algorithm consists of a grow-region algorithm, like the applied in lung segmentation for EA/TEF design model. For more detail revise 3.2.2 Medical Image Processing

Guidelines for breast cancer reconstructive surgery require the surgeon to specify the information about scar and if applicable the donor site, and this information should be discussed with the patient. However, many women express dissatisfaction, regret and negativity relative to these conversations (157). Providing appropriate preoperative information, by the application of tumor segmentation and volumetric analysis using 3D haptic biomodels, medical image processing, and reverse engineering provide a better understanding for surgical approach, this can lead in a decrease for cancer recurrence and empower patients with a better understanding of the pathology.

Additionally, there is all too little information about how women are supported after surgical procedure and see their aesthetic appearance. Research conducted by Paraskeva et al. in England, explored women's thoughts, expectations and behaviors to the aesthetic results of their mastectomy or breast reconstruction, suggesting ways in which breast care teams, physicians and familiars might be able to give supportive care and intervention (158) (159).Patient reactions to their post-surgical procedures were characterized by the relief that the cancer had been removed, and that their appearance was better or about the same as they had imagined. The negative feelings described by the patients were expressed as more distressing than anticipated. Some women had unrealistic expectations regarding the outcome of breast reconstruction, including donor-site scarring (160) (158).

Following similar methodology as section 3.3 3D Volumetric Analysis for Breast Reconstructive Surgery can the fabrication of soft tissue prostheses can also be undertaken. These soft tissues are designed using reverse engineering, 3D scanning a part of the body (161). Design consists of an inverse model and casting with medical-grade silicone. This method can be applied in reconstructive surgery and can contribute to solving the problem of high costs in soft tissue prostheses.

Determination of breast volume could mitigate all the outcomes for breast interventions, including the emotional and psychological outcomes. However, all the calculations used for determining breast volume exhibit variable reliability. Some techniques are expensive (MRI), uncomfortable (casting), and/or messy and imprecise (Archimedes principle).

As mentioned in section 2.7 Breast Reconstructive Surgery, this project focused on reverse engineering implementing 3D scanning and photogrammetry and anthropomorphic methods due the simplicity. With anthropomorphic methods the variability can be caused from the simplifcation of the beast form to the geometrical shape that was defined in the Qiao equation (Equation 2), though this form does not necessarily correspond to the patient's natural form.

Using CAD/CAM systems like 3D scanning for reverse engineering, the advantage is the ease and speed in obtaining a 3D model of the breast, inclusive the 3D model can be acquired without body contact, making the patient more comfortable. The 3D model does not represent a deformation of the breast, as in mammograms. Comparing with photogrammetry, the illumination (high ISO) is a determinant factor that can represent noise and loss of information. In fact, that's the reason why there is no useful data in 3 samples using photogrammetry presented in Table 25. Several studies have concluded that 3D scanning and using CAD/CAM system could make a difference in the determination of the breast volume relative to conventional methods (162) (128). Much more work is needed for validation of these methodologies. Another limitation is the need for very experienced CAD/CAM management to make the analysis, relying a new "outsourcing" for breast surgical procedures.

As there was not a significative difference between the results obtained through various methods, there is greater confidence that all of these methods could be acceptable for generating the desired measurements. This would suggest that the cheapest, fastest, and most non-invasive option (like 3D scanning) could therefore be the optimal choice. A significant limitation, however, was that the sample was too small. The Linear Measurements were done using the formula by Quia (132). In one volunteer's case, the mastectomy had already been performed. The use of Agisoft Photoscan can

lead in loss of capture scanning due the intense light. More photos are needed to generate a more stable capture. However, photogrammetry can be useful for nipple reconstruction. This study could be described as preliminary and further investigation are needed.

Chapter 6 Future Work

"It is not the strength of the body that counts, but the strength of the spirit."
— *J.R.R. Tolkien* (163)

Different procedures have been presented for surgical planning in maxillofacial surgery, pediatric surgery and breast cancer reconstructive surgery. However, future work must be considered according to the advancement of technology and the needs that arise. The proposals for further work progress would be the development of algorithms and kernels for the processing of medical images. Slicer3D is compatible with Python and Matlab, which allows modification and development of extensions for a better process of medical image analysis. In this way one can automate the workflow and at the same time receive feedback on ideas.

The implementation of new materials for FDM technology can result in the creation of anatomical models for more versatile educational purposes. The simulation of haptic models for 3D printing with biomaterials can be performed. The incorporation of SLA technology for intraoperative haptic models. The validation of the EA repair prototype through a qualitative analysis with expert laparoscopic surgeons and residents of pediatrics.

Increasing the sample size on the volumetric analysis of breast cancer can validate the method and provide enough individuals for correlation and comparison of the final volume during the mastectomy, including integrating new algorithms of computer vision and image recognition to create a 3D model with fewer photos.

Chapter 7 Conclusions

"I was surprised to see how hard and fragile the kitchen of science could be, and how worthy was the work of the chefs who made it work, I decided to become a diner instead of a cook, and go out and taste the best dishes"

-Pere Estupinyá (164)

In the last decade, 3D printing has revolutionized the perspective of medical diagnosis. However, the implementation of this technology has not been uniform in all sectors due to the lack of resources for the purchase, maintenance and handling of industrial equipment. However, the implementation of FDM technology, which is lower cost and has relatively less space requirements, can be considered as the beginning to adapt 3D technology in clinics and hospitals for the benefit of society, including the most vulnerable sectors.

The development of the procedure from obtaining medical images to post-processing in medical applications requires time and knowledge of image processing, anatomy, radiology, design, and handling in 3D printing, which makes it a highly multidisciplinary procedure. The processing of images is important when defining the region of interest, which makes it one of the most complex challenges in the design of haptic models, due to the computational capacity and available algorithms to obtain a rendering of the anatomy, with the lowest artifact and noise possible. which can interfere with the diagnosis and surgical planning. The proposed work method focused on CBCT, which have a high noise and are prone to artefacts. However, the recommended thresholds and methods of segmentation were proposed, as well as the post-processing filters to obtain a haptic quality model, suitable for surgical planning in maxillofacial surgery.

The design of haptic models in cases of maxillofacial surgery, show an improvement in the diagnosis and surgical planning. This improvement translates into greater precision in the surgical procedure, reducing costs and operating room times, and benefits the patient with a lower risk of exposure to infection. However, not only has an economic benefit been shown in the work presented here, but also there were instances of a better understanding between patient and doctor, which can reduce adverse outcomes such as abandonment of treatment. In the same way, the anatomy of pathologies is understood and known, which can be directly applied in training and medical education.

At present there are industrial-grade 3D printers that can print on different materials depending on their degree of stiffness and color, but most if not, all have a very high cost. Many cases would be necessary to amortize the cost and maintain consumables. Therefore, the link between companies, universities, hospitals and clinics is of great importance and necessary, to be able to implement 3D printing in full capacity in medical applications – especially in a country with an economy like Mexico.

The EA prototype is an example of the versatility and compatibility of materials that can be implemented using an FDM desktop printer. This creates an advantage in the development of training models with specific anastomoses.

The work method presented in this thesis can be adapted to the needs and requirements of specific pathologies, such as neurosurgery, tumor removal, and malformations or on the equally-important task of education. An advantage of the proposed work method is that the materials used are more like human tissue, in contrast to those used in industrial-grade printers. The implementation of a surgical model of training for pediatric surgery would result in the reduction of the training curve, resulting in an effective saving for the hospital cost. The implementation of a work model using FDM technology allows multidisciplinary application, making possible the development of different training models, and haptic models for the different disciplines of medicine

The integration between CAD / CAM systems and 3D printing is of vital importance to obtain a haptic model. Similarly, the manipulation of anatomical models, such as those obtained by reverse engineering by means of 3D scanning, can be subjected to more accurate mesh analysis for work with such advanced tools like FEA, as well as more fundamental tasks like obtaining more precise dimensional volumes and correction factors or adjustments.

These processes are all necessary in breast cancer reconstructive surgery. Analysis of symmetry and dimensions through CAD / CAM systems, allows a greater understanding of the anatomy, without requiring high costs. The proposed work methods are even recommended for hospitals and clinics with low resources and located in inaccessible places. However, the difference between both methods varies in the time of data processing, being the use of the ideal 3D scan for extremities and body parts of larger size. For small anatomical structures with more detail, the use of photogrammetry with specialized Macro lenses is ideal because the produced images have a higher resolution, at the cost of more processing time. Even the proposed work method is adaptable to orthopedic surgery and disciplines such as physiotherapy, in the same way obtaining a 3D model

with texture allows a postoperative analysis for the evaluation of new asymmetries according to time and even for the study of pattern recognition in cancer of skin.

Despite the advantages of implementing 3D technology in medical applications such as maxillofacial surgery, pediatric surgery and breast cancer reconstructive surgery, there are still limitations in terms of materials, prices and especially in time and trained personnel. However, the interest in 3D printing has been spreading in the general public, which can result in a greater advancement and acceptance of technology, developing more efficient machines, reducing costs, greater trained personnel and new collaboration policies that integrate the 3D technology industry with medicine

Inequality in society is increasing because medical technology is expensive and that limits access to medical care. We believe that the work presented here show that the processes refinement and workflows to adapt 3D printing technology so that it is available to all sectors of society can be done. Furthermore, it can be done without forgetting the most vulnerable members of the population. Given that about 95% of Mexico's medical technology is imported (165).

Doing research, improving educational programs, forming multidisciplinary teams, creating, and bringing these creations to market is the way to innovate in biomedical science and engineering, Innovating is not only creating new things, it is adapting technology to the needs.

"It matters if you just don't give up."

— *Stephen Hawking* (134)

.

References

1. **Sagan, Carl.** *Dragons of Eden: Speculations on the evolution of human intelligence.* s.l. : Ballantine Books, 2012.

2. *Thoracoscopic surgery for esophageal atresia.* **GW, Holcomb III.** s.l. : Pediatr Surg Int, 2016.

3. *Mammographic determination of breast volume:comparing different methods.* **Kalbhen CL, McGill JJ, Fendley OM, Corrigan KW, Angelats J.** 1643-1649, s.l. : AJR Am J Roentgnol, 1999, Vol. 173.

4. **Mundial, Banco.** Banco Mundial. [Online] 2019. [Cited: 02 10, 2019.] https://datos.bancomundial.org/indicador/SP.POP.GROW?locations=MX.

5. **Nations, United.** World Population Prospects. [Online] 2017. [Cited: 02 10, 2019.] https://population.un.org/wpp/DataQuery/.

6. **Mundial, Banco.** Banco Mundial Salud. [Online] 2019. [Cited: 02 10, 2019.] https://datos.bancomundial.org/tema/salud?locations=MX.

7. —. Banco Mundial. [Online] 2019. [Cited: 02 10, 2019.] https://datos.bancomundial.org/tema/salud?locations=MX.

8. **Data, The world Bank.** The World Bank Data. [Online] 2019. [Cited: 03 20, 2019.] https://data.worldbank.org/topic/health?contextual=default&locations=DE-US-BR-KR-CL-JP-MX-1W.

9. *The utility of a multimaterial 3D printd model for surgical planning of complez deformity od the sull base and craniovertebral junction.* **PacioneD, Tanweer O, Berman P.** 1194, s.l. : J. Neurosurg, 2016, Vol. 125.

10. *three-dimensional planning in craniomaxillofacial surgery.* **Rubio-Palau, prieto-Gndin, Azalla AA.,.** 2, s.l. : Annalsof Maxillofacial Surgery, 2016, Vol. 6.

11. *Image Guided 3D Printing and Haptic Modelling in Platic Surgery.* **Chae PM, Hunter-Smith DJ & Rozen MW.** 2014.

12. *Relative effectiveness of high-versus low-fidelity simulation in learning heart sounds.* **de Giovanni D, Roberts T, Norman G.** 7, s.l. : Med Educ, 2009, Vol. 43.

13. **Scientific, 3B.** 3B Scientific. [Online] 2019. [Cited: 03 10, 2019.] https://www.a3bs.com/neonatal-patient-care,pg_155.html.

14. *Cost: The missing outcome in simulation-based medical education resarch: A systematic review.* **Zendejas B, Wang TA, Brydges R, Hamstra JS, Cook DA.** 2, s.l. : Surgery, 2013, Vol. 153.

15. *Cost-effective simulation. In: Walsh H, editor. Cost effectiveness in medical education.* **Ker J, Hogg G. .** s.l. : Oxon: Raddclife, 2010.

16. *Objective Breast VOlume,Shape and Surface Area Assesment Asystematic Review of Breast Measurement Methods.* **Wenjing Xi, Trisliana A, Yeesiang Ong.** 1116-1130, s.l. : Aesth Plast Surg, 2014, Vol. 38.

17. **Drexler, Erick.** *Engines of Creation.* s.l. : Anchor, 1990.

18. *3D Printing techniques in a medical settings: a systematic literature review.* **Philip Tack, Jan Victor, Paul Gemmel and Lieven Annemans.** 115, s.l. : BioMed Eng OnLine, 2016, Vol. 15.

19. **ASTM.** *ASTM F2792-10 standard terminology for additive manufacturing technologies.*

20. *Economiv implications of 3D-printing:market structure models in light of additive manufacturing revisited.* **Weller C., Kleer R, Piller FT.** 43-56, s.l. : Int.J.Prod.Econ, 2015, Vol. 164.

21. *Additive manufacturing: technology, applications and research needs.* **Nannan GUO, Ming C. LEU.** 3, s.l. : Front. Mech. Eng., 2013, Vol. 8, pp. 215-243.

22. **Amanda Su, Subhu J. Al'Aref.** History of 3D Printing. *3D printing aapplications in cardiovascular Medicine.* s.l. : Academic Press, 2018, pp. 1-10.

23. *Automatic method for fabrication a three-dimensional plastic model with photo-hardening polymer.* **H, Kodama.** 11, s.l. : Rev Sci Instrum, 1981, Vol. 52, pp. 1770-3.

24. *History of additive manufacturing.* **Wohlers T, Gornet T.** 2014.

25. **US5340433, Patent.** Modeling Apparatus for three-dimensional objects. *google patents.* [Online] https://www.google.com/patents/US5340433.

26. **Richard Bibb, Dominic Eggber , Abby Paterson.** *Medical modelling: the application of advanced design and rapid prototyping techniques in medicine.* s.l. : Woodhead Publishing, 2015.

28. *Surgical applications of three-dimensional printing: a reviewof the current literature and how to get started.* **Don Hoang, David Perrault, Mila Stevanovic, Alidad Ghiassi.** 23, s.l. : Annals of Translational Medicine, 2016, Vol. 4.

29. *Preoperative stereolithographic model plannins for primary reconstruction in craniomaxillofacial trauma surgery.* **C. Kermer, a. Lindner, I. Friede, a. Wagner,W. Millesi,.** (3), s.l. : j. Craniomaxillofac. Surg, 1998, Vol. 26, pp. 136-139.

30. *Application of 3D rapid prototyping technology in posterior corrective surgery for Lenke 1 adolescent idiopathic scoliosis patients.* **Yang M, Li C, Li Y, .** s.l. : Medicine, 2015, Vol. 94.

31. *Clinical application of three-dimensional printing in the personalized treatment of complex spinal disrders.* **Wang YT, Yang XJ, Yan B.** s.l. : Chin J Traumatol, 2016, Vol. 19.

32. *Use of a three dimensional printed cardiac model to assess suitability for biventricular repair.* **Farooqi KM, Gonzalez-Lengua C, Shenoy R, .** s.l. : World J Pediatr Congeit Heart Surg, 2016, Vol. 7.

33. *Three dimensional patient-specific cardaic model for surgical planning in Nikaido procedure.* **Valverde I, Gomez G, Gonzalez A.** s.l. : Cardiol Young, 2015, Vol. 25, pp. 698-704.

34. *From 3-Dimensional printing to 5-Dimensional Printing: enhancing thoracic surgical planning and resection of complez Tumors.* **Gillaspie EA, Matsumoto JS, Morris NE.** s.l. : Ann Thorac Surg, 2016, Vol. 101.

35. *Myocardial 3-Dimensioanl Printing for Septal Myectomy Guidance in a patient with obstructive hypertrophic Cariomyopathy Circulation.* **yang DH, Kang JW, Kim N.** s.l. : Circulation, 2015, Vol. 132.

36. *Surgical Planning by 3D printing for primary cardiac Schwannoma Resection .* **Son KH, Kim KW, Ahn CB.** s.l. : yonsei Med J, 2015, Vol. 56.

37. *Pediatric cardaic trnasplantation : three-dimensioanl printing of anatomc models for surgical planning of heart transplantation in patients with univentricular heart.* **Sodian R, Weber S, Markert M.** s.l. : J Thorac Cardiovasc Surg, 2008, Vol. 136.

38. *Three dimensional printing of intracariac defects from three-dimensional echocardiographic images: feasibility and relative accuracy.* **Olivieri LJ, Krieger A, Loke YH.** s.l. : J Am Soc Echocardiogr, 2015, Vol. 28.

39. *A three-dimensioanl mediastinal model created with rapid prototyping in a patient with ectopic thymoma.* **Akiba T, Nakada T, Inagaki T,.** s.l. : Ann Thorac Cardiovasc Surg, 2015, Vol. 21.

40. *Three dimensional printing for perioperative planning of compplex aortic arch surgery.* **Schmauss D, Juchem G, Weber S.** s.l. : Ann Thorac Surg, 2014, Vol. 97.

41. *Thorascoscopic anatoical subsegmentetomy of the right S2b +S3 using a 3D printing model with rapid prototyping.* **Nakada T, Akiba T, Inagaki T.** s.l. : Interact Cardiovasc Thorac Surg, 2014, Vol. 19.

42. *Custom fenestration templates for endovascular repair of juxtarenal aortic aneurysms.* **Leotta DF, Starnes BW.** s.l. : J Vasc Surg, 2015, Vol. 61.

43. *Patient Specific biomodel of the whole aorta-the importance of calcified plaque removal.* **Hakansson A, Rantatalo M, Hansen T.** s.l. : Vasa, 2011, Vol. 40.

44. *3D printing in surgical management of double outlet right ventricle.* **Shi-Joon Yoo & Glen S. van Arsdell.** 289, s.l. : Frontiers in Pediatrics, 2018, Vol. 5.

45. *Mitigation of tracheobronchomalacia with 3D-printed personalized MEdical Devics in Pediatric Patients.* **Robert J. Morrison, Scott J. Hollister, Matthew F. Niedner, Maryam Ghadimi Mahani, Albert H. Park, Deepak. Mehta, Richard G. Ohye and Glenn E. Green.** s.l. : Sci Transl Med, 2015, Vol. 29.

46. *Simulation-based Medical education: An Ethical Imperative.* **Ziv A, Wolpe RP, Small DS Click S.** 8, s.l. : Academic Medicine, 2003, Vol. 78.

47. *3D printing materials and ther use in medica education: a review of current technology and trends for the future.* **Garcia J, Yang Z, Mongrain R, Leask R and Lachapelle K.** 27-40, s.l. : BMJ, 2018, Vol. 4.

48. *Creation of a 3D printed temporal bone model fron clincal CT data.* **Cohen J, Reyes SA.** s.l. : AM J Otolaryngol, 2015, Vol. 36, pp. 619-24.

49. *A novel temporal bone simulation model using 3D printing techniques.* **Mowry SE, Jammal H, Myer C.** s.l. : otol Neurotol, 2015, Vol. 36, pp. 1562-5.

50. *Comparison of cadaveric and isomorphic three-dimensional printed models in temporal bone education.* **Hochman JB, Rhodes C, Wong D,.** s.l. : Laryngoscope, 2015, Vol. 125, pp. 2353-7.

51. *Rapid prototyping of temporal bone for surgical training and medical education.* **suzuki M, Ogawa Y, Kawano A.** s.l. : Acta otolaryngol, 2004, Vol. 124, pp. 400-2.

52. *A neurosurgical simulation of skull base tumors using a #D printed rapid prototyping model containig mesh structures.* **Kondo k, Harada N, Masuda H.** s.l. : Acta Neurochir, 2016, Vol. 158, pp. 1213-9.

53. *Creation of an in vitro biomechanical model of the trachea using rapid prototyping.* **Walenga RL, Longest PW, Sundaresan G.** s.l. : J Biomech, 2014, Vol. 47, pp. 1861-8.

54. *3D rapid prototypiing for otolaryngology head and neck surgery: applications in image-guidance, surgical simulation and patient-specific modeling.* **Chan HH, Siewerdsen JH, Vescan A.** s.l. : PloS One, 2015, Vol. 10.

55. *Three-dimensional printing to facilitate anatomic study, device development, simulation and planning in thoracic surgery.* **Kurenoc Sn, lonita C, Sammons D.** s.l. : J Thorac Cardiovasc Surg, 2015, Vol. 149, pp. 973-9.

56. *Three-dimensional printing in cardiac surgery and interventional cardiology: a single -centre experience.* **Schmauss D, Haeberle S, Hagl C.** s.l. : Eur J Cardiothorac Surg, 2015, Vol. 47, pp. 1044-52.

57. *Erratum to: 3D printed modeling of the mitral valve for catheter-based structural interventions.* **Vukicevic M, puperi DS, Grande-Allen KJ.** s.l. : Ann Biomed Eng, 2016, Vol. 44, pp. 3432-12.

58. *Do 3D printing models improve anatomical teaching about hepatic segments to medical students? A randomized controlled study.* **Kong X, Nie L, Zhang H.** 1969-76, s.l. : World J surg, 2016, Vol. 40.

59. *Cerebrovascular biomodeling for aneurysm surgery:simulation-based training by means of rapid prototyping technologies.* **Wurm G, Lehner M, Tomancok B.** 294-306, s.l. : Surg Innov, 2011, Vol. 18.

60. *Dual-material 3D printed meta materials with tunable mechanical properties for patient-specific tissue-mimicking phantoms.* **Wang K, Wu C, Qian Z.** 31-7, s.l. : Addit Manuf, 2016, Vol. 12.

61. *Additive manufacturing and its societal impact: a literature review.* **Samuel H. Huang., Peng Liu., Abhiram Mokasdar., Liang Hou.** s.l. : Int J adv Manuf Technol, 2013, Vol. 67, pp. 1191-1203.

62. *Stereolitography for manufacturing ceramic parts.* **Doreau F,Chaput C, Chartier T.** 8, s.l. : Advanced Engineering Materials, 2000, Vol. 2, pp. 493-496.

63. *Projection microstereolithography using digital micro-mirrir dynamic mask.* **Sun C, Fang N, Wu D M, Zhang X.** 1, s.l. : sensors and actuators. A, Physical, 2005, Vol. 121, pp. 113-120.

64. *Additive manufacturing (3D printing): A review of materials, methods, applications and challenges.* **Tuan D. Ngo, Alireza Kashani, Gabriele Imbalzano, Kate T.Q. Nguyen, David Hui.** s.l. : Composites Par B, 2018, Vol. 143, pp. 172-196.

65. *3D printing of polymer matrix composites: a revies and prospective.* **Wang X, Jiang M, Zhou Z, Gou J,Hui D.** s.l. : Compos B Eng, 2017, Vol. 110, pp. 442-58.

66. *Multifunctional metal matrix composites with embedded printed electrical materials fabricated by ultrasonic additive manufacturing.* **Li J, Monaghan T, Nguyen TT, Kay RW, Firel RJ, Harris RA.** s.l. : Compos B Eng, 2017, Vol. 113, pp. 342-54.

67. *Interfacial shear strength estimates of NiTi-Al matrix composites fabricated via ultrasonic additive manufacturing.* **Hehr A, Dapino MJ.** 2015, Vol. 77, pp. 199-208.

68. **Meyer-Bäse, Anke.** *Pattern Recognition for medical imaging.* s.l. : Elsevier Academic Press, 2004.

69. *Medical Image Processing Overview.* **Zhu, Hongmei.**

70. **Hiroshi. Yoshioka, Philipp M. Schlechtweg, Katsumi. Kose.** Magnetic Resonance Imaging. [book auth.] BarbaraN. Weissman. *Imaging of Arthritis and Metabolic Bone Disease.* s.l. : Elsevier, 2009.

71. *3D Printing from MRI Data: Harnessing Strengths and Minimizing Weaknesses.* **Beth Ripley, Dmitry Levin, Tatiana Kelil, Joshua L Hermsen, Sooah Kim, Jeffrey H Maki, Gregory J Wilson.** 00, s.l. : J Magn Reson. Imaging, 2016, Vol. 00.

72. *Metal-induced artifacts in MRI.* **Hargreaves BA, Worters pW, Pauly KB, Pauly JM, Koch KM, Gold GE.** 547-555, s.l. : Am J Roentgenol, 2011, Vol. 197.

73. *Whole-heart steady-state free precession coronary artery magnetic resonance angiography.* **Weber OM, Marting AJ, Higgings CB.** 1223-1228, s.l. : Magn REson MEd, 2003, Vol. 50.

74. *Blood pool segmentation results in superior virutal cardiac models than myocardial segmentation for 3D printing.* **Farooqi KM, Lengua CG, Weinberg AD, Nielsen KC, Sanz J.** 1028-1036, s.l. : Pediatr Cardiol, 2016, Vol. 37.

75. *MP RAGE: a three-dimensional, T1 - weighted, gradient-echo sequence-initial experience in the brain.* **Brant-Zawadzki M, Gillan GD, Nitz WR.** 769-775, s.l. : Radiology, 1992, Vol. 182.

76. *Pulmonary magnetic resonance angiopgraphy.* **Meaney JF, Johansson LO, Ahlstrom H.** 326-338, s.l. : J Magn Reson Imaging, 1999, Vol. 10.

77. *CT scanning: a major source of radiation exposure.* **Wiest PW, Locken JA, Heintz PH, Mettler FA.** 5:402-10, s.l. : Semin. Ultrasound CT MR, 2002, Vol. 23.

78. *Advances im Computed Tomography Imaging Technology.* **Ginat DT and Gupta R.** 431-53, s.l. : Annu. Rev. Biomed EN., 2014, Vol. 16.

79. *Principles of computer assisted tomography (CAT) in radiographic and radioisotropic imaging.* **Brooks RA, Di Chiro G. .** 689-732, s.l. : phys. Med. Biol, 1976, Vol. 21.

80. *Artifacts in CT: Recognition and Avoidance.* **Julia F. Barret, Nichlas Keat.** 1679-1691, s.l. : RadioGraphics, 2004, Vol. 24.

81. **Kalra, Anil.** Developing FE Human Models From Medical Images. [book auth.] King-Hay Yang. *Basic Finite Element Method as applied to injury biomechanics.* s.l. : Elsevier, 2018.

82. *Clinical CT: Techniques and practices London UK.* **S, Henwood.** s.l. : Greenwich Medical MEdia LTD.

83. ***Issa Al-shakhrah, PdD and Tariq Al-Obaidi.*** *s.l. : applied radiology, 2003.*

*84. The double*fissure sign: Amotion artifact on thin section CT scan.* ***MAyo RJ, Muller NL, Henkelman RM.*** *580-581, s.l. : Radiology, 1987, Vol. 165.*

85. REal tme x-ray fan beam z axis position measurement. ***Gard, Michaek F.*** *295-298, s.l. : IEEE trans instr Meas, 1994, Vol. 43.*

86. Computed Tomography of the whole Body . ***Haaga JR, Alfidi RJ.*** *s.l. : Mosby Company, 1988.*

87. Conebeam CT of the gead and neck, part 1: physical principles. ***Miracle AC, Mukherji SK.*** *1088-95, s.l. : AM. J. Neuroradiol, 2009, Vol. 30.*

88. Cone beam micro-CT system for small animal imaging and performance evaluation. ***Zhu S, Tian J, Yan G, Qin C, Feng J.*** *960573, s.l. : Int. J. Biomed. Imaging, 2009, Vol. 2009.*

89. Flat-panel volume CT: fundamental principles, technology, and applications. ***Gupta R, Cheung AC, Bartling SH, Lisauskas J, Grasruck M.*** *2009-22, s.l. : Radiographics, 2008, Vol. 28.*

90. Deriving Hounsfield units using grey levels in cone beam computed tomography. ***Mah P, Reeves TE, McDavid WD. .*** *323-35, s.l. : Dentomaxillofac Radiol, 2010, Vol. 39.*

91. Relationshio between Hounsfield Unit in CT scan and Gray Scale in CBCT. ***Tahmineh Razi, Mahdi Niknami, Fakhri Alavi Ghazani.*** *2:107-110, s.l. : J Dent Res Dent Clin Dent Prospect, 2014, Vol. 8.*

92. Technical aspects of dental CBCT: state of the art. ***R Pauwels, K Araki, J H Siewerdsen and s S Thongvigitmanee.*** *20140224, s.l. : Dentomaxillofacial Radiology, 2015, Vol. 44.*

93. Artefacts in CBCT: a review. ***Schulze R, Heil U, Gross D, Bruellmann DD; Dranischnikow E, Schwanecke U.*** *265-73, s.l. : dentomaxillofac RAdiol, 2011, Vol. 40.*

94. 3D scanning system for in vivo imaging of human body. ***Ares M, Royo S, Vidal J.*** *899-902, s.l. : Springer, 2014, Vol. 2014.*

95. Aesthetic reconstruction of microtia: a review of current techniques and nes 3Dprinting aproaches. ***Ross MT, Cruz R, Hutchinson C, Arnott WL, Woodruff MA, Powell SK.*** *2:117-130, s.l. : Virtual Phys Prototyp, 2018, Vol. 13.*

96. 3D scanning applications in medical field: a literature-based review. ***Abid Haleem, Mohd Javaid.*** *s.l. : Clinical Epidemiology and Global Health, 2018.*

97. Close-range photogrammetry applications in bridge measurement:literature review. ***Jiang R, Jauregui DV, White KR.*** *823-834, s.l. : Measurement, 2008, Vol. 41.*

98. Obtaining malignant melanoma indicators through statistical analysis of 3D skin surface disruptions. ***Ding Y, Smith M, Sun J, Warr R.*** *262-270, s.l. : Skin Res Technol, 2009, Vol. 15.*

99. Feasibility of contactless 3D optical measurement for the analysis of bone and soft tissue lesions: new technologies and perspectives in forensic sciences. ***Sansoni G, Cattaneo C, Trebeschi M, Gibelli D, Porta D, Picozzi M.*** *540-545, s.l. : J Forensic Sci, 2009, Vol. 54.*

100. Photogrammetry and its potential application in medical science on the basis of selected literature. ***Halina Ey Chielewska, Malgorzata Chrusciel Nogalska, Bogumila Fraczak.*** *4:737-741, s.l. : Adv Clin Exp Med, 2015, Vol. 24.*

101. Medical 3D printing for the radiologist. ***Dimitris mitsouras et al.*** *1965-1988, s.l. : radiographics, 2015, Vol. 35.*

102. Medical Image Segmentation Methods, Algorithms and Applications. ***Norouzi A, Rahim M. Altameem A, Saba T, Rad E. Rehman A, Uddin M.*** *3, s.l. : IETE tecnincal review, 2014, Vol. 31.*

103. A survey of current methods in medical image segmentation. ***Pham DL, Xu C, Prince LJ.*** *315-37, s.l. : Ann. Rev. Biomed. EMg, 1998, Vol. 2.*

104. Image segmentation in digital mammography: Comparison of local thresholding and region growing algorithms. ***Kallergi M, Woodsa K, Ckarkea L, Quiana W.*** *5, s.l. : Comp. Med Imag Graph, 1992, Vol. 16.*

105. Segmentation and Image Aalysis of abnormal Lungs at CT: Current Approaches, challes,and Future trends. ***Mansoor A, Bagci U, Foster B, Xu Ziyue, Papadakis GZ, Folio LR, Udupa JK, Mollura DJ.*** *1056-1076, s.l. : RadioGraphics, 2015, Vol. 35.*

106. Evaluation of 3D printing and its Potential Impact on Biotechnology and the chemical Sciences. ***Gross BC, Erkal JL, Lockwood SY, Chen C, and Spence DM.*** *3240-3253, s.l. : And. Chem, 2014, Vol. 86.*

107. ***Aura.*** *i.materialise. [Online] may 29, 2018. [Cited: 02 15, 2019.] https://i.materialise.com/blog/en/preparing-files-for-3d-printing/.*

108. Three-dimensional Printing in Maxillofacial Surgery: Hype versus Reality. ***aldaadaa A, Owji N, Knowles J.*** *1-5, s.l. : Journal of Tissue Engineering, 2018, Vol. 9.*

109. Applications od additive manufacturing in dentistry: A review. ***Bhargav A, sanjairaj V, Rosa V, Feng WL.*** *s.l. : Wiley Periodicals, 2017.*

110. A narrative of a monstous birth in Plymouthtogether with the natomical observations, taken there upon by william Durston Docot in Physik and communicated to Dr.Timclerk. ***W, Durston.*** *2096, s.l. : Philios Trans Lond, 1670, Vol. 5.*

111. Experience with thoracoscopic repair of long gap esophageal atresia in neonates. ***Rothenberf SS , Flake AW.*** *932-935, s.l. : J Laparoedosc Ad Surg Tech A, 2015, Vol. 25.*

112. Esophageal Atresia new guidelinesin management. ***Gonzalez-hernandez J, Lugo-vicente H.*** *1, s.l. : Boetion de la asociacion meddicade puerto rico, 2010, Vol. 102.*

113. Thoracoscopic repair of esophageal atresia and tracheoesophageal fistula in neonates, firstdecades experience. ***SS, Rothenberg.*** *359-364, s.l. : Disease of the Esophagus, 2013, Vol. 26.*

114. ***World Health Organization.*** *[Online] 2019. [Cited: febrero 14, 2019.] https://www.who.int/news-room/fact-sheets/detail/cancer.*

115. *Cancer Trends in Mexico: Essential Data for the creation and Follow Up of Public Policies.* ***Mohar-Bentacourt A. Reynoso-Noveron N.Armas-Texta D., Gutierrez-Delgado C., Torres-Dominguez JA.*** *6, s.l. : Journal of Global Oncology, 2017, Vol. 3.*

116. *Breast cancer in Mexicn women: an epidemiological study with cervical cancer control****.*** ***Guzman-Tovar V, Hernandez-Giron C, Lazcano-Ponce E, Romieu I, Avila-H M****,. 2, s.l. : Rev. Saude Publica , 2000, Vol. 34.*

117. Geografia del cancer de mama en Mexico. MR, Castrezana-Campos. *s.l. : Invest.Geog, 2017, Vol. 93.*

118. *Costs of breast cancer care in Mexico: analysis of two insurance converage scenarios.* ***Gonzalez-Robledo CM, Wong R, Arreola-Ornelas H. Knaul F.*** *587, s.l. : ecancer, 2015, Vol. 9.*

119. Mexico, Secretaria de Salud. Programa Nacional de Salud 2001-2006. *[Online] www.salud.gob.mx/unidades/cdi/nom/compi/pns20012006.pdf.*

120. *National and regional breast cancer incidence and mortality trends in Mexico 2001:2011: analysis of a population-based database****. Soto-Perez-de-Celis E, Chavarri-Guerra Y.*** *24-33, s.l. : Cancer Epidemiol, 2016, Vol. 41.*

121. Chavarri-Guerra Y., Villareal-Garza, Liedke PER, Knaul F. *e335-43, s.l. : Lancer Oncol , 2012, Vol. 13.*

122. *Clinical and Epidemiological Profile of Breast Cancer in Mexico: Results of the Seguro Popula****r. Reynoso-Noveron N. Villareal-Garza C. Arce-Salinas C et al.*** *6, s.l. : J****ournal of Global Oncology, 2017, Vol. 3.***

123. Informatics, National Institte of Statistics Geography and. Government and Society : socieconomic indicators. *[Online] www.inegi.org.mx/sistemas/temasV2/Default.aspx.*

124. Poor esthetic results after conservative treatment of breast cancer. technics of partial breast reconstrucion. *petit JY, Rigaut L, Zekri A, Le M. 2:103-8, s.l. : Ann Chir Plast Esthet., 1989, Vol. 34.*

125. *Oncoplastic techniques allow extensive resections for breast-conserving therapy of breast carcinomas****. Clough KB, Lewis JS, Couturaud B.*** *26-34, s.l. : Ann Surg, 2003, Vol. 237.*

126. *Oncoplastic Breast Surgery: What, When and for Whom****. Douglas Macmillan, MCCulley SJ.*** *112-117, s.l. : Curr Breast Cancer Rep, 2016, Vol. 8.*

127. *"use what God has given me": difference and disparity in breast reconstruction****. Rubin LR, Chavez J, Alderman A, Pusic LA.*** *10, s.l. : psychol Health, 2013, Vol. 28.*

128. *five methods of breast volume measurements: a comparative study of measurements of specimen volume in 30 mastectomy cases****. Kayar R, Civelek S, Cobanogly M,Gungor O, Catal H, Emiroglu M. 43-52****, s.l. : Breast Cancer , 2011, Vol. 5.*

129. *3D volumetric analysis and Haptic Modeling for preoperative planning breast reconstruction****. P Chae, Smith-Hunter DJ, Rizzltelll A. Spychal TR, Rozen W.*** *1, s.l. : anaplastology, 2015, Vol. 4****.***

130. *A simple means for accurate breast volume determination****. Grossman AK, Roudner LA.*** *851-852, s.l. : Plast Reconstr Surg, 1980, Vol. 66.*

131. *A formula for surgical modificacitons of the breast****. Brown RW, Cheng YC, Kurtay M.*** *1342-1345, s.l. : Plast Reconstr Surg, 2000, Vol. 106.*

132. *Breast volume measuement in young Chinese womenand clinical applications* ***. Qiao Q, Zhou G, Ling Y.*** *362-368, s.l. : Aesthet Plast Surg, 1997, Vol. 21.*

133. *Breast volume determination in breast determination in breast hypertrophy: an accurate method using two antrhopormorphic measurements****. Sigurdson LJ, Kirkland SA.*** *313-320, s.l. : Plast reconstr Surg, 2006, Vol. 118.*

134. Marsh, James. *The Theory of Everything. working tittle films, 2014.*

135. *Pre.Post-operative visualization of neonantal esophageal atresia/tracheoesophageal fistulavia magnetic resonance imaging.* ***Hgano NS, Bates Aj, Tkach JA, Fleck RJ, Lim FY, Woods JC, Kingma PS.*** *s.l. : J Pediatr Surg Case Rep, 2018, Vol. 29.*

136. Alexievich, Svetlana. *The Unwomanly Face of War. s.l. : Penguin UK, 2017.*

137. Slicer. Slicer. *[Online] 2019. [Cited: 02 18, 2019.] https://www.slicer.org/.*

138. *Anatomical dimensions of trachea, main bronchi, subcarinal and bronchial angles in fetuses measured exvivo****. Harjeet, Sahni D, Batra YK, Rajeev S.*** *11, s.l. : Paediatr Anaesth, 2008, Vol. 10****.***

139. *Determinants of gap length in esophageal atresia with tracheoesophageal fistula and the impact of gap length on outcome****. Rassiwala M, Choudhurry SR, Yadav PS, Jhanwar P,Agarwal RP, Chadha R, and Debnath PR.*** *3, s.l. : J indian Assc Pediatr Surg, 2016, Vol. 21.*

140. *Three-dimensional Printing in maxillofacial Surgery: Hype versus Reality****. Aldaadaa A, Owji N and knowles.*** *s.l. : J tissue Eng, 2018, Vol. 9.*

141. *Novel bioactive materials with different mechanical properties.* ***kokubo T, Kim H, Kawashita M.*** *13, s.l. : biomaterials, 2003, Vol. 24.*

142. *Biofabrication of PLGA-TCP-based porous bioactive bone substitute with sustained release of icaritin****. Xie XH, Wang XL, Zhang G, et al. (8)****, s.l. : J Tissue Eng Regen Med, 2015, Vol. 9.*

143. *Engineering human TMJ discs with protein-releasng 3D-printed scaffolds.* ***Legemate K, Tarafder S, Jun Y , et al. 7,*** *s.l. : J Dent Res, 2016, Vol. 95.*

144. *Evaluation of a porous, biodegradable biopolymer scaffold for mandibular reconstruction.* ***Trantolo DJ, Sonis ST, thompson BM, etal****. 2, s.l. : Int J oral maxillofac Implants, 2003, Vol. 18.*

145. *Biocompatibility and osteogenesis of biomimetic nanohydroxyapatite/polyamide composite scaffolds for bone tissue engineering****. Wang H, Li Y Zuo Y .*** *22, s.l. : Biomaterials, 2007, Vol. 28.*

146. *Patient-Specific Surgical Implants Made of 3D printed PEEK:Material, Technology, and Scope of Surgical Application****. Honingmann P, Sharma N, Okolo B, Popp U, Msallem B, Thieringer FM.*** *s.l. : Biomed res Int, 2018, Vol. 4520636.*

147. Aniwaa. Aniwaa. *[Online] 2019. [Cited: 04 02, 2019.] https://www.aniwaa.com/product/3d-printers/apium-p220/.*

148. *3D-printed simulationdevice for orbital sugery.* ***Lichtenstein JT, Zeller AN, Lemound J, Lichtenstein TE, Ranna M, Gellrich NC, Wagner ME. 1,*** *s.l. : J Surgical Education, 2016, Vol. 74.*

149. 3Faktur. 3Factur. *[Online] 2018. [Cited: 04 1, 2019.] https://3faktur.com/en/3d-printing-materials-technologies/selective-laser-sintering-sls-technology-overview/selective-laser-sintering-sls-material-pa12pa2200-nylon/#1486464083768-fd5616c7-78f2.*

150. mundi, Index. Index Mundi. *[Online] [Cited: 04 2, 2019.] https://www.indexmundi.com/es/datos/indicadores/SH.XPD.TOTL.ZS.*

151. Organization, World Health. World Health Organization. *[Online] 2019. [Cited: 04 02, 2019.] https://www.who.int/countries/deu/en/.*

152. *Prenatal craniofacial abnormalities: from ultrasonography to 3D-printed model****. Nicot R, Druelle C, Hurteloup E, Levaillant J.-M.*** *s.l. : Ultrasound in Obstetrics and Gynecology, 2019.*

153. *2D XFEM-based modeling of retraction and succesive resections for preoperative image updat****e. Vigneron, LM et al.*** *s.l. : Comput Aided. Surg , 2009, Vol. 14.*

154. *Fabrication of cerebral aneurysm simulator with a desktop 3D printe****r. Liu Y., Gao Q., D S., Chen Z., Fu JF., Chen B., Lui Jie and He Y. 44301,*** *s.l. : Sci Rep, 2017, Vol. 7.*

155. *Validation of an inaniate low cost model for training minimal invasive surgery (MIS) of esophageal atresia with trahceoesophageal fistula (AE/TEF) repair****. Maricic Ma, Bailez MM, Rodriguez SP.*** *9, s.l. : J Pediatr Surg, 2016, Vol. 51.*

156. *Semi-automated delineation of breast cancer tumors and subsequent materialization using three-dimensional printing (rapid prototyping).* ***Wendtland SR, Harz M, Meitinger MM, Brehm B, Wacker T, Hahn KH, Wagner F, Wittenberg T, Beckmann MW, UderM, Fasching PA, Emons J.*** *s.l. : Journal of surgical oncology, 2016.*

157. *Decision regret following breast reconstruction: The role of self-efficacy and satisfaction with information in the preoperative period****. Zhong T, Hu J, Bagher S, O´neill AC, Beber Bm Hofer SOP. 5,*** *s.l. : plast reconstr surg, 2013, Vol. 132.*

158. *First look: a mixedmethods study explorng womens initial experiences of their appearance after mastectomy and or breast reconstruction****. ParaskevaN, Herring B, Tolloww Pand Harcourt D.*** *s.l. : journal of plastic reconstructive and asthetic surgery, 2019.*

159. *Decisional regret and choice of breast reconstruction following mastectomy for breast cancer: a systematic review****. flitcroft K, Brennan M, spillane A.*** *s.l. : psychooncology, 2017.*

160. *satisfaction with outcome and attitudes towards scarring among women undergoing breast reconstructive surgery****. Abu- Nab Z, Grunfeld EA. 22,*** *s.l. : Patient Educ Couns, 2007, Vol. 66.*

161. *fabrication of low cost soft tissue prostheses with the desktop 3D printer****. He, Y., Xue, G and Fu, J.*** *6973, s.l. : Sci. Rep, 2014, Vol. 4.*

162. *Comparison between breast volume measurement using 3D surface imaging and classical techniques****. kovacs L, Eder M, Hollweck R, Zimmermann A, Settles M, Scneeier A, Endlich M, Mueller A, Zimmerer KS, Papadopulos NA, Biemer E.,.*** *s.l. : The Breast, 2007, Vol. 16.*

163. Tolkien, JRR. *The fellowship of the ring. s.l. : Harper Collins, 1999.*

164. P, Estupinya. *El Ladron de cerebros. Compartiendo el conocimiento cientifico de las mentes mas brillantes. 201****0.***

165. Consejo Nacional de Ciencia y Tecnología (CONACYT). *Programa Especial de Ciencia, Tecnología e Innovación 2014-2018. CONACyT. Mexico, D.F. : México, Gobierno de la República, 2014. Plan Nacional de Desarrollo 2012-2018.*

Appendices

8.1. STATISTICS. Non-parametric test for 3D Haptic Biomodels for Presurgical Planning in Maxillofacial Surgery

- **Normality Test (Kolmogorov-Smirnov)**

Data source: Data 2 in Notebook1

CAD V1:	K-S Dist. = 0.224	P = 0.018	Failed
FDM V1:	K-S Dist. = 0.226	P > 0.200	Passed
CAD V2:	K-S Dist. = 0.195	P = 0.070	Passed
FDM v2:	K-S Dist. = 0.234	P > 0.200	Passed
CAD V3L:	K-S Dist. = 0.237	P = 0.009	Failed
FDMV3L:	K-S Dist. = 0.261	P > 0.200	Passed
CAD V3R:	K-S Dist. = 0.117	P > 0.200	Passed
FDM V3R:	K-S Dist. = 0.234	P > 0.200	Passed
CAD v4L:	K-S Dist. = 0.218	P = 0.023	Failed
FDM v4L:	K-S Dist. = 0.228	P > 0.200	Passed
CAD V4R:	K-S Dist. = 0.150	P > 0.200	Passed
FDM V4R:	K-S Dist. = 0.183	P > 0.200	Passed
CAD V5L:	K-S Dist. = 0.118	P > 0.200	Passed
FDM V5L:	K-S Dist. = 0.207	P > 0.200	Passed
CAD v5R:	K-S Dist. = 0.188	P = 0.091	Passed
FDM V5R:	K-S Dist. = 0.235	P > 0.200	Passed
CAD CL:	K-S Dist. = 0.227	P = 0.015	Failed
FDM CL:	K-S Dist. = 0.210	P > 0.200	Passed
CAD Cr:	K-S Dist. = 0.248	P = 0.005	Failed
FDM CR:	K-S Dist. = 0.154	P > 0.200	Passed

- **t-test**

Data source: Data 2 in Notebook1

Normality Test (Kolmogorov-Smirnov) Failed (P < 0.050)

Test execution ended by user request, Rank Sum Test begun

Mann-Whitney Rank Sum Test

Data source: Data 2 in Notebook1

Group	N	Missing	Median	25%	75%
CAD V1	18	0	112.905	110.979	117.883
FDM V1	6	0	113.410	108.175	119.650

Mann-Whitney U Statistic= 52.000

T = 77.000 n(small)= 6 n(big)= 18 (P = 0.920)

; there is not a statistically significant difference (P = 0.920)

- **t-test**

Data source: Data 2 in Notebook1

Normality Test (Kolmogorov-Smirnov) Passed (P = 0.121)

Equal Variance Test: Passed (P = 0.472)

Group Name	N	Missing	Mean	Std Dev	SEM
CAD V2	18	0	93.792	2.956	0.697
FDM v2	6	0	92.397	3.339	1.363

Difference 1.395

t = 0.971 with 22 degrees of freedom. (P = 0.342)

95 percent confidence interval for difference of means: -1.584 to 4.374

There is not a statistically significant difference between the input groups (P = 0.342).

Power of performed test with alpha = 0.050: 0.050

- **t-test**

Data source: Data 2 in Notebook1

Normality Test (Kolmogorov-Smirnov) Passed (P = 0.138)

Equal Variance Test: Passed (P = 0.794)

Group Name	N	Missing	Mean	Std Dev	SEM
CAD V3L	18	0	29.433	2.620	0.618
FDMV3L	6	0	31.660	2.417	0.987

Difference -2.227

t = -1.834 with 22 degrees of freedom. (P = 0.080)

95 percent confidence interval for difference of means: -4.744 to 0.291
There is not a statistically significant difference between the input groups (P = 0.080).

Power of performed test with alpha = 0.050: 0.298

- **t-test**

Data source: Data 2 in Notebook1

Normality Test (Kolmogorov-Smirnov) Passed (P = 0.787)

Equal Variance Test: Passed (P = 0.256)

Group Name	N	Missing	Mean	Std Dev	SEM
CAD V3R	18	0	28.856	2.804	0.661
FDM V3R	6	0	30.237	1.657	0.677

Difference -1.381

t = -1.132 with 22 degrees of freedom. (P = 0.270)

95 percent confidence interval for difference of means: -3.911 to 1.149

There is not a statistically significant difference between the input groups (P = 0.270).

Power of performed test with alpha = 0.050: 0.076

- **t-test**

Data source: Data 2 in Notebook1

Normality Test (Kolmogorov-Smirnov) Passed (P = 0.209)

Equal Variance Test: Passed (P = 0.635)

Group Name	N	Missing	Mean	Std Dev	SEM
CAD v4L	18	0	28.993	7.704	1.816
FDM v4L	6	0	32.317	5.346	2.182

Difference -3.324

t = -0.974 with 22 degrees of freedom. (P = 0.340)

95 percent confidence interval for difference of means: -10.398 to 3.750

There is not a statistically significant difference between the input groups (P = 0.340).

Power of performed test with alpha = 0.050: 0.050

- **t-test**

Data source: Data 2 in Notebook1

Normality Test (Kolmogorov-Smirnov) Passed (P = 0.535)

Equal Variance Test: Passed (P = 0.954)

Group Name	N	Missing	Mean	Std Dev	SEM
CAD V4R	18	0	30.887	4.190	0.988
FDM V4R	6	0	29.755	4.799	1.959

Difference 1.132

t = 0.554 with 22 degrees of freedom. (P = 0.585)

95 percent confidence interval for difference of means: -3.107 to 5.371

There is not a statistically significant difference between the input groups (P = 0.585).

Power of performed test with alpha = 0.050: 0.050

- **t-test**

Data source: Data 2 in Notebook1

Normality Test (Kolmogorov-Smirnov) Passed (P = 0.740)

Equal Variance Test: Passed (P = 0.917)

Group Name	N	Missing	Mean	Std Dev	SEM
CAD V5L	18	0	15.002	1.694	0.399
FDM V5L	6	0	15.040	1.652	0.674

Difference -0.0383

t = -0.0483 with 22 degrees of freedom. (P = 0.962)

95 percent confidence interval for difference of means: -1.685 to 1.609

There is not a statistically significant difference between the input groups (P = 0.962).

Power of performed test with alpha = 0.050: 0.050

- **t-test**

Data source: Data 2 in Notebook1

Normality Test (Kolmogorov-Smirnov) Passed (P = 0.052)

Equal Variance Test: Passed (P = 0.670)

Group Name	N	Missing	Mean	Std Dev	SEM
CAD v5R	18	0	14.996	1.570	0.370
FDM V5R	6	0	14.480	1.970	0.804

Difference 0.516

t = 0.655 with 22 degrees of freedom. (P = 0.519)

95 percent confidence interval for difference of means: -1.117 to 2.148

There is not a statistically significant difference between the input groups (P = 0.519).

Power of performed test with alpha = 0.050: 0.050

- **t-test**

Data source: Data 2 in Notebook1

Normality Test (Kolmogorov-Smirnov) Failed (P < 0.050)

Test execution ended by user request, Rank Sum Test begun

Mann-Whitney Rank Sum Test

Data source: Data 2 in Notebook1

Group	N	Missing	Median	25%	75%
CAD CL	18	0	17.980	17.418	18.210
FDM CL	6	0	17.965	14.788	19.208

Mann-Whitney U Statistic= 50.000

T = 71.000 n(small)= 6 n(big)= 18 (P = 0.815)
there is not a statistically significant difference (P = 0.815)

- **t-test**

Data source: Data 2 in Notebook1

Normality Test (Kolmogorov-Smirnov) Failed (P < 0.050)

Test execution ended by user request, Rank Sum Test begun

Mann-Whitney Rank Sum Test

Data source: Data 2 in Notebook1

Group	N	Missing	Median	25%	75%
CAD Cr	18	0	17.200	11.898	17.630
FDM CR	6	0	16.935	14.303	20.153

Mann-Whitney U Statistic= 37.500

T = 91.500 n(small)= 6 n(big)= 18 (P = 0.285)

; there is not a statistically significant difference (P = 0.285)

Table 26 Statistic for 3D Haptic Biomodels for Presurgical Planning in Maxillofacial Surgery factor correction and validation

	CAD V1	FDM V1	CAD V2	FDM V2	CAD V3L	FDM V3L	CAD V3R	FDM V3R	CAD V4L	FDM V4L	CAD V4R	FDM V4R	CAD V5L	FDM V5L	CAD V5R	FDM V5R	CAD CL	FDM CL	CAD CR	FDM CR
Mean	112.7419	112.89	93.792	92.3967	29.4334	31.66	28.8556	30.2367	28.9929	32.3167	30.8872	29.755	15.0077	15.04	14.9956	14.48	17.8144	17.2983	15.465	17.0317
Median	112.9045	113.41	94.735	91.805	30.19	30.84	29.055	30.15	28.9	31.69	30.245	29.87	15.05	14.68	14.67	14.05	17.98	17.965	17.2	16.935
Std.dev	6.563	7.312	2.9556	3.3395	2.6203	2.4172	2.8038	1.6574	7.7043	5.346	4.1801	4.7989	1.6943	1.6521	1.5702	1.9688	1.4325	2.2959	3.447	3.1275
std.err	1.5469	2.9851	0.6966	1.3633	0.6176	0.9868	0.6609	0.6766	1.8159	2.1825	0.9876	1.9592	0.3984	0.6745	0.3701	0.8042	0.3376	0.9373	0.8125	1.2768
95% conf	3.2637	7.6736	1.4698	3.5046	1.303	2.5367	1.3943	1.7394	3.8313	5.6103	2.0837	5.0362	0.8426	1.7338	0.7809	2.0672	0.7124	2.4094	1.7142	3.2822
93% conf	4.4836	12.0365	2.0192	5.4972	1.7901	3.979	1.9155	2.7283	5.2634	8.8002	2.8626	7.8996	1.1575	2.7196	1.0727	3.2426	0.9786	3.7793	2.3549	5.1483
size	18	6	18	6	18	6	18	6	18	6	18	6	18	6	18	6	18	6	18	6
Total	2029.355	677.34	1688.256	554.38	529.8017	189.96	519.4007	181.42	521.8717	193.9	555.97	178.53	270.03	90.24	269.92	86.88	320.66	103.79	278.37	102.19
min	98.36	100	87.3	88.87	24.41	29.57	24.09	28.17	14.13	26.51	25.6	21.87	11.86	13	12.9	12.15	14.51	14	10	12.66
max	120.12	120.13	97.79	96.97	32.42	35.59	33.8	32.65	39.25	38.94	39.54	35.9	18.6	17.61	19.84	18.02	20.4	19.8	20.4	20.91
min poss	98.36	100	87.3	88.87	24.41	29.57	24.09	28.17	14.13	26.51	25.6	21.87	11.86	13	12.9	12.15	14.51	14	10	12.66
missing	0	0	0	0	0	0	0	0	0	0	0	0	0	0	0	0	0	0	0	0
other	0	0	0	0	0	0	0	0	0	0	0	0	0	0	0	0	0	0	0	0

8.2 Ethical considerations and privacy aspects

8.2.1 SUBJECT SELECTION FOR 3D VOLUMETRIC ANALYSIS FOR BREAST RECONSTRUCTIVE SURGERY

- Population:

Directed to a population of women from 18 to 70 years, without ethnic or social class distinction.

• Inclusion

Inclusion Criteria are referred for women 18 to 70 years of age.

Women who have implants have no risk in the present study. However, it would be cataloged in a different group.

Women who are going to be subjected to mastectomies may be included in the study with the prior authorization and consent of their oncologist

Women who have undergone total or partial mastectomy surgery.

Women who have undergone reconstructive surgery after a tumor resection have no risk in the present study. However, it would be cataloged in a different group because there is evidence that immediate reconstructive surgeries have a better result in an aesthetic matter than the reconstructive surgeries that have been postponed. Therefore, it is considered that symmetric reconstructions can be modified.

• Exclusion:

Women with cognitive deficiencies.

Women who present emotional instability.

Underage women

• Elimination Criteria

Women who feel uncomfortable in the procedure and decide to finish the study.

Women who are considered to have given wrong or false information about their age and medical history.

Women who at the time of the photo session are in a state of intoxication and under the influence of psychotropic substances or recreation.

- Data protection and privacy

  The required data are name, age, and anthropomorphic measurements.

  Each woman will be assigned a numeric key per study. To avoid a direct relationship with the name and study.

  Each photo session per participant will be stored in removable storage units. For no reason will they be shared in storage clouds such as Google Drive or Dropbox.

  Due to the sensitivity of the study, the photos taken for the photogrammetry analysis will not focus on the face, only the upper part of the trunk.

  At the end of the photo session for the photogrammetry analysis, the participant will be shown to verify that at no time will her identity be exposed.

  The study participant will be free to give a pseudonym or just provide a surname.

  The participant will have the option to grant a medium for their contact such as email or mobile phone.

  For any reason, the information will be made public for purposes not related to this study.

  The participant can choose if she wants to show sections of her study for publications in scientific journals, congresses, thesis presentation, and a written thesis, as well as any written means related to scientific research. In case the participant accepts, she would choose exhibition formats of sections of her studio, for example, color photos, grayscale, interrupted sections with black bars, point clouds, alignment, volumetric models.

  The participant cannot be informed exactly the technical protocol to follow to generate the volumetric models, in order to protect the study.

- Informed consent:

  Each participant will be given informed consent before carrying out any process. In which the title of the investigation, the objective of the investigation, the study procedure will be explained. The selection criteria of the participants. The time required, the risks and benefits, privacy aspects, data protection and the right to withdraw from the study.

- Individual protection. Pre-Peri-post study.

The study is non-invasive, does not require any substance administration. Therefore, it does not require care.

During the study of the photo shoot, only female staff will be found. The participant may request the presence of a person they trust. Under no circumstances will undue physical contact be made. In case of needing physical contact, the participant will be asked to consent. No physical contact is allowed unless it has purposes that justify the study. The participant may at any time request that the study is paused or withdrawn.

The participant does not require post-process care.

• Potential risks.

No potential risk.

Discomfort, stress, anxiety.

• Mitigation risks.

None.

- Distribution of risk and benefit for the study population.

The goal is to benefit all social classes without ethnic distinctions

There is no exclusive risk.

The inequality of benefit of the study may be due to other factors such as customs, individual experiences, beliefs, expectations, lack of knowledge of reconstruction procedures.

To ensure an appropriate distribution of benefits, the procedure is inexpensive and easy to handle.

It is necessary to create a collaborative culture between oncological surgery and reconstructive surgery.

- Conflict of interests

The possible conflict of interest can be due to a lack of communication with the participants and patients of breast cancer, due to the existing vulnerability of a diagnosis that consists of a radical procedure affecting the individuality as a person.

There is no type of funding proposed by a health or educational institution, so there can be no bias in the results.

There must be objectivity of the scope and limitations of the study and constant feedback from medical specialists,

- Request for data deletion once the study is completed

Because the validity of the study can be compromised by the exclusion without chance and consent, the information can not remove data obtained in the study once the study is completed. This is clear in the proposed informed consent, however, because of the sensitivity of the study in terms of data protection and privacy, the photographic images can be removed, but the 3D models generated are not. This includes the cloud of alignment points and the dense point cloud.

8.3 STATISTICS for volumetric analysis for breast reconstructive surgery

Table 27 Descriptive statistics for 4.3 Breast Reconstructive Surgery

	CAD LEFT	CAD RIGHT	AG LEFT	AG RIGHT	M LEFT	M RIGHT
MEAN	277.102	339.46	277	235.8	286.6	319.8
MEDIAN	291	382.4	293	310	300	330
STD DEV	95.9427	120.0547	149.6429	163.3805	101.896	107.4626
STD ERROR	42.9069	53.6901	86.3964	73.066	45.5693	48.0587
95% CONF	119.1258	149.0641	370.9557	202.859	126.5177	133.4293
99% CONF	197.4959	247.1298	845.0332	336.3151	209.7506	221.2092
SIZE	5	5	5	5	5	5
TOTAL	1385.51	1697.3	831	1179	1433	1599
MIN	151.91	143.9	120	0	140	142
MAX	414	460	418	385	423	430
MIN POS	151.91	143.9	120	134	140	142
MISSING	0	0	0	0	0	0
OTHER	0	0	2	0	0	0

Statistics non-parametrics test for 4.3 Breast Reconstructive Surgery

- **Normality Test (Kolmogorov-Smirnov)**

Data source: TODO in estadistica beast

CAD L:	K-S Dist. = 0.226	P > 0.200	Passed
CAD R:	K-S Dist. = 0.240	P > 0.200	Passed
AG L:	K-S Dist. = 0.209	P > 0.200	Passed
AG R:	K-S Dist. = 0.275	P > 0.200	Passed
M Left:	K-S Dist. = 0.209	P > 0.200	Passed
M Right:	K-S Dist. = 0.338	P = 0.064	Passed

- **t-test**

Data source: Left Breast in estadistica beast

Normality Test (Kolmogorov-Smirnov) Passed (P = 0.484)

Equal Variance Test: Passed (P = 0.237)

Group Name	**N**	**Missing**	**Mean**	**Std Dev**	**SEM**
CAD Left	5	0	277.202	95.961	42.915
AG Left	5	2	277.000	149.643	86.396

Difference 0.202

t = 0.00237 with 6 degrees of freedom. (P = 0.998)

95 percent confidence interval for difference of means: -208.219 to 208.623

There is not a statistically significant difference between the input groups (P = 0.998).

Power of performed test with alpha = 0.050: 0.050

- **t-test**

Data source: Left Breast in estadistica beast

Normality Test (Kolmogorov-Smirnov) Passed (P = 0.255)

Equal Variance Test: Passed (P = 0.961)

Group Name	**N**	**Missing**	**Mean**	**Std Dev**	**SEM**
CAD Left	5	0	277.202	95.961	42.915
M Left	5	0	286.600	101.896	45.569

Difference -9.398

t = -0.150 with 8 degrees of freedom. (P = 0.884)

95 percent confidence interval for difference of means: -153.745 to 134.949

There is not a statistically significant difference between the input groups (P = 0.884).

Power of performed test with alpha = 0.050: 0.050

- **t-test**

Data source: Left Breast in estadistica beast

Normality Test (Kolmogorov-Smirnov) Passed (P = 0.594)

Equal Variance Test: Passed (P = 0.294)

Group Name	N	Missing	Mean	Std Dev	SEM
M Left	5	0	286.600	101.896	45.569
AG Left	5	2	277.000	149.643	86.396

Difference 9.600

t = 0.110 with 6 degrees of freedom. (P = 0.916)

95 percent confidence interval for difference of means: -204.734 to 223.934

There is not a statistically significant difference between the input groups (P = 0.916).

Power of performed test with alpha = 0.050: 0.050

- **t-test**

Data source: Right Breast in estadistica beast

Normality Test (Kolmogorov-Smirnov) Passed (P = 0.239)

Equal Variance Test: Passed (P = 0.721)

Group Name	N	Missing	Mean	Std Dev	SEM
CAD right	5	0	339.660	120.306	53.803
AG right	5	1	294.750	111.461	55.731

Difference 44.910

t = 0.574 with 7 degrees of freedom. (P = 0.584)

95 percent confidence interval for difference of means: -140.042 to 229.862

There is not a statistically significant difference between the input groups (P = 0.584).

Power of performed test with alpha = 0.050: 0.050

- **t-test**

Data source: Right Breast in estadistica beast

Normality Test (Kolmogorov-Smirnov) Passed (P = 0.118)

Equal Variance Test: Passed (P = 0.876)

Group Name	N	Missing	Mean	Std Dev	SEM
CAD right	5	0	339.660	120.306	53.803
M Right	5	0	319.800	107.463	48.059

Difference 19.860

t = 0.275 with 8 degrees of freedom. (P = 0.790)

95 percent confidence interval for difference of means: -146.498 to 186.218

There is not a statistically significant difference between the input groups (P = 0.790).

Power of performed test with alpha = 0.050: 0.050

- **t-test**

Data source: Right Breast in estadistica beast

Normality Test (Kolmogorov-Smirnov) Failed (P < 0.050)

Test execution ended by user request, Rank Sum Test begun

Mann-Whitney Rank Sum Test

Data source: Right Breast in estadistica beast

Group	N	Missing	Median	25%	75%
AG right	5	1	330.000	178.000	376.250
M Right	5	0	330.000	236.000	398.500

Mann-Whitney U Statistic= 8.000

T = 18.000 n(small)= 4 n(big)= 5 P(est.)= 0.712 P(exact)= 0.730

there is not a statistically significant difference (P = 0.730)

Pearson Product Moment Correlation

Data source: Right Breast in estadistica beast

Cell Contents:
Correlation Coefficient
P Value
Number of Samples

	AG right	M Right
CAD right	0.995 0.00524 4	0.983 0.00265 5
AG right		0.987 0.0129 4
M Right		

Pearson Product Moment Correlation

Data source: Left Breast in estadistica beast

Cell Contents:
Correlation Coefficient
P Value
Number of Samples

	AG Left	M Left
CAD Left	0.999 0.0253 3	0.992 0.000876 5
AG Left		1.000 0.0147 3
M Left		